UC Irvine
UC Irvine Electronic Theses and Dissertations

Title

Development of theoretical and computational tools to study photochemistry involving multiple electronic excited states

Permalink

https://escholarship.org/uc/item/31j764pv

Author

Roy, Saswata

Publication Date

2020

Copyright Information

Peer reviewed|Thesis/dissertation

UNIVERSITY OF CALIFORNIA,
IRVINE

Development of theoretical and computational tools to study photochemistry involving
multiple electronic excited states

DISSERTATION

submitted in partial satisfaction of the requirements
for the degree of

DOCTOR OF PHILOSOPHY

in Chemistry

by

Saswata Roy

Dissertation Committee:
Professor Filipp Furche, Chair
Professor Kieron Burke
Professor Vladimir A. Mandelshtam

2020

DEDICATION

To people paying taxes

TABLE OF CONTENTS

LIST OF FIGURES

LIST OF TABLES

ACKNOWLEDGMENTS

Completing a Ph.D. may seem like an individual accomplishment, but it is far from the truth, at least in the case of this thesis. I have been fortunate to work with a group of extremely talented and helpful people in my graduate career and I would like to thank them for being a part of my journey.

I had the privilege of working with Prof. Filipp Furche as my advisor. His scientific brilliance can only be overshadowed by his dedication towards helping younger scientists grow. Under his guidance, I have learnt to more critical, self-reliant and compassionate towards others. I can not thank him enough for supporting me and helping me develop as a theoretical chemist.

I am grateful to the other members of my thesis committee, Prof. Vladimir A. Mandelshtam and Prof. Kieron Burke. I have greatly benefitted from the courses on statistical mechanics and mathematical methods taught by Prof. Mandelshtam. The courses on density functional theory offered by Prof. Burke are phenomenal and has helped me immensely in my graduate carreer. In addition, I would like to thank both Prof. Burke and Prof. Mandelshtam for being supportive of my during my examination for the advancement to candidacy.

UCI is a wonderful place to learn theoretical chemistry, and I am thankful to Profs. Shaul Mukamel and Ioan Andricioaei for having introduced me to some of the other branches of theoretical chemistry. I am fortunate to be in the same department as Prof. Craig Martens who has been extremely helpful with discussions on semi-classical dynamics, which forms a large part of my research at UCI.

I benefitted a lot from the collaborative nature of the department. It was a wonderful opportunity to work with my collaborators here at UCI; Dr. Daniel N. Huh, Prof. William J. Evans and Prof. Shane Ardo. I would additionally like to thank Prof. Ardo for being extremely supportive of me throughout my graduate carreer and also for offering the wonderful summer course on photoelectrochemisty that helped me connect several broader ideas. I would also like to thank Dr. Gianmarc Grazioli for collaborating with me on the acetaldehyde project.

My colleagues and senior group members have been directly involved in shaping me as a scientist. Prof. Shane M. Parker, Prof. Vamsee K. Voora, Dr. Mikko Muuronen and Dr. Eva von Domaros have been wonderful post-docs and mentors during my time in the Furche group, and I can not thank them enough. Dr. Brandon Krull, Dr. Jordan C. Vincent, Dr. Guo P. Chen, B. Sree Ganesh, Matthew M. Agee, Luke Nambi Mohanam, Jason M. Yu, Brian D. Nguyen, Gabriel Phun, Samuel Bekoe and Jeffrey Tsai are the amazing graduate students that I had the privilege to be colleagues with. I am indebted to the continuous support from Dr. Nathan Crawford and Ms. Jenny Du, without which none of this work would have been possible. I am also indebted to my high school students, Jasper Hu, Gary Zeri, Bailey Kau and Sophie Hwang, who were excellent mentees and helped me grow as a mentor.

In my graduate school I befriended a few other scientists and I have been fortunate to have such wonderful friends. I would like to thank Dr. William N. White, Drew Cunningham, Dr. James McSally, John Houlihan, Dr. Sandra Brown, Dr. Joel Mallory, Dr. Anupam Chatterjee, Dr. Alana F. Ogata, Dr. Saleh Riahi Samani, and William Ogden from the chemistry department who indulged in a whole lot of discussions on chemistry with me, often over a pint of beer at the Antihill Pub. I would like to thank Dr. Austin J. Ryan, Shane Flynn, Francisca Sagredo, Victoria Lim, Dr. Kara Kapnas, Dhiman Ray and Moises Romero for being wonderful friends and part of my experience as a graduate student at UCI.

Living on my own in a foreign country was a new experience for me, it only got enriched with the amazing friends I made while I stayed in Irvine. People like Sanjana Goswami, Rohit Bhide, Lily Li, Dr. Srikiran Chandrasekaran, Dr. Anirudh Wodeyar, Dr. Pele Schramm, Dr. Mayukh Mondal, Tabitha Miller, Demet Kirmizibyrak, Ankita Biswas, Achint Sanghi, Paul Tschida, Yash Gargasia and Apurva Bhasin helped me step out of my department and I have benefitted immensely from that. I am indebted to BATS, the junior choir group at UCI, where I sang for 3.5 year and it helped me keep my sanity.

A handful of my friends from my undergraduate institutions have been in close contact with me throughout my graduate career. I could not have completed this work without the support of Madhura Dattagupta, Deep Chatterjee, Dr. Soumalya Sinha, Dr. Sumanta Bandyopadyay, Bibek Ranjan Samanta and Ankan Bag. Thank you guys for being there for me and reminding me that there lies more to my identity than being a chemistry graduate student.

My family has been a cornerstone of my life and my identity. I would like to thank my father, Mr. Sudipta Kumar Roy and my mother, Dr. Sonali Roy for giving me all the love and support required and often providing the necessary counselling. My sister, Sulagna Roy, has been a constant source of inspiration in my life, and I am thankful for that.

VITA

Saswata Roy

EDUCATION

Doctor of Philosophy in Chemistry   **2020**
University of California, Irvine   *Irvine, California*

BS-MS of Science in Chemistry   **2014**
Indian Institute of Science Education and Research, Kolkata   *Mohanpur, West Bengal*

RESEARCH EXPERIENCE

Graduate Research Assistant   **2015–2020**
University of California, Irvine   *Irvine, California*

TEACHING EXPERIENCE

Teaching assistant at University of California, Irvine

General chemistry lecture discussions teaching assistant	Fall **2014**
General chemistry lecture discussions teaching assistant	Winter **2015**
General chemistry laboratory teaching assistant	Spring **2015**
Classical mechanics and electromagnetism lecture (Graduate level) teaching assistant	Fall **2015**
General chemistry laboratory teaching assistant	Spring **2016**
General chemistry lecture discussions teaching assistant	Summer **2018**
Density functional theory lecture (Graduate level) teaching assistant	Fall **2018**

REFEREED JOURNAL PUBLICATIONS

Shane M. Parker, Saswata Roy, Filipp Furche
Multistate Hybrid Time-dependent Density Functional Theory with Surface Hopping Accurately Captures Ultrafast Thymine Photodeactivation, *Phys. Chem. Chem. Phys.* **21**, 18999–19010, 2019. doi: 10.1039/c9cp03127h

Daniel N. Huh, Saswata Roy, Joseph W. Ziller, Filipp Furche, William J. Evans
Isolation of a Square Planar Th(III) Complex: Synthesis and Structure of $[\text{Th}(\text{OC}_6\text{H}_2{}^t\text{Bu}_2\text{-}2,6\text{-Me-4})_4]^{1-}$, *J. Am. Chem. Soc.* **141**, 12458–12463, 2019. doi: 10.1021/jacs.9b04399

Saswata Roy, Shane Ardo, Filipp Furche
5-Methoxyquinoline Photobasicity is Mediated by Water Oxidation, *J. Phys. Chem. A* **123**, 6645–6651, 2019. doi: 10.1021/acs.jpca.9b05341

Gianmarc Grazioli, Saswata Roy and Carter T. Butts
Predicting Reaction Products and Automating Reactive Trajectory Characterization in Molecular Simulations with Support Vector Machines,*J. Chem. Inf. Model.* **59**, 2753–2764, 2019. doi: 10.1021/acs.jcim.9b00134

Shane M. Parker, Saswata Roy and Filipp Furche
Unphysical Divergences in Response Theory, *J. Phys. Chem.* **145**, 134105, 2016 doi: 10.1063/1.4963749

Subhajit Bandyopadyay and Saswata Roy Determination and Comparison of Carbonyl Stretching Frequency of a Ketone in Its Ground State and the First Electronic Excited State, *J. Chem. Ed.* **91**, 1995–1998, 2014. doi: 10.1021/ed500442a

CONFERENCE TALK AND POSTER PRESENTATION

<u>talks</u>   March **2018**

Quinoline Photobasicity is Mediated by Hole Injection
American Physical Society March Meeting   Los Angeles, USA

Nonadiabatic molecular dynamics simulations of photo-   June **2016**
catalysts and photoacids
Great Lakes Regional Meeting of the American Chemi-   Fargo, USA
cal Society

<u>posters</u>   July **2017**
Quinoline Photobasicity is Mediated by Hole Injection
American Conference on Theoretical Chemistry   Boston, USA

poster: Non-Adiabatic molecular dynamics simulations   February **2016**
251st American Chemical Society National Meeting and   San Diego, USA
Exposition

SOFTWARE

Turbomole   https://www.turbomole.org/
Leading code for solving electronic structure problems

ABSTRACT OF THE DISSERTATION

Development of theoretical and computational tools to study photochemistry involving
multiple electronic excited states

By

Saswata Roy

Doctor of Philosophy in Chemistry

University of California, Irvine, 2020

Professor Filipp Furche, Chair

The development, implementation and benchmarking of the computational tools to study photochemical processes is reported in this dissertation. Fewest switches surface hopping (FSSH) in conjunction with density functional theory (DFT) and time-dependent DFT (TDDFT) forms the basis of the methodology. DFT and TDDFT was also used to explain the unusual electronic structure of the first synthesized square planar actinide complex. A π–donating ligand field theory was proposed to explain the d_{z^2} character of the highest occupied molecular orbital of this complex. The theory was supported by the agreement between the simulated and the experimentally observed UV/Vis spectrum.

The excited state deactivation of 5-methoxyquinoline, a known photobase, was studied using the developed methodology. Active participation of the water molecules in quenching the excitation of the chromophore was observed from the simulations. The observed mechanism challenges the validity of Förster cycle to understand photoacidity and photobasicity. The simulations were also able to explain the lack of kinetic isotope effect observed from the experimental transient absorption spectroscopy.

With access to stable analytical derivative couplings between excited states, it was possible to study the performance of TDDFT/FSSH methodology for thymine. The simulated excited

state lifetimes agreed with experimental observations. Addition of decoherence correction to the FSSH algorithm resulted in no decay to the ground state. Analysis of the lowest excited potential energy surface of thymine as generated from TDDFT showed a kinetic barrier to a conical intersection, explaining the lack of decay to the ground state. Two different flavors of decoherence correction was implemented, and will be available in the next release of Turbomole.

Chapter 1

Introduction to the thesis

1.1 Energy and water economy

Water crisis and extreme weather events are listed among the top ten global risks, in terms of impact and likelihood by UNESCO.[1,2] In addition, as a consequence of rising CO_2 concentrations, the acidification of the oceans[3] put the oceans' food cycle in jeopardy, which in turn adversely affects the livelihood of millions of people depending on the health of the ocean.[4] With a global rise in population at a rate of 1.1%,[5] more and more human lives are at risk from both water crises and climate change. Yet, despite all scientific warnings, our fossil fuel consumption is at its maximum, directly contributing to some of the distress.

While scientific solutions to the crises regarding energy,[6–8] water,[9] and carbon capture[10] exist, the efficiencies of current methodologies do not compensate for the economic and political inertia in using fossil fuel and denying the consequences. Fossil fuels are simultaneously energy and power dense, making them very reliable sources of energy and hard to replace. The long-standing hope of using the abundant solar power as a substitute provides plenty of scientific and engineering challenges. The field of solar photocatalysis, which aims at trans-

forming solar energy into chemical energy, has been an active field of research for several decades.[11,12] While there have been several success stories in photocatalysis,[13] many of the processes are poorly understood, making systematic improvements hard. Since almost 45% of solar radiation energy have wavelengths greater than 1.2 eV, the first step of capturing the photon energy is through electronic excitation.[14] Most photocatalysts work on the principle of transferring the energy from the excited electrons to the nuclear degrees of freedom. Traditional description of chemistry involving the Born-Oppenheimer approximation[15] excludes the possibility of exchange of electronic excitation energy with the nuclei,[16] making the understanding of such processes difficult. Since the Born-Oppenheimer approximation is often called the 'adiabatic' approximation, where the nuclei are treated as stationary point charges while solving the electronic Schrödinger equation, the processes where this approximation is inappropriate are termed 'nonadiabatic'.

Nonadiabatic molecular dynamics (NAMD) is a theoretical tool used to describe nuclear motion in scenarios where the electronic excitation energies are comparable to the nuclear kinetic energies, allowing the possibility to transfer of energy between the nuclear and the electronic degrees of freedom.[16] For the execution of NAMD, knowledge of the electronic potential energy surfaces as well as the coupling between the electronically excited states due to the nuclear kinetic energy operator are required. While the exact solution is computationally intractable, well established approximate solutions for the electronic Hamiltonian and the semi-classical nuclear propagation exist. Like all approximations, the methods have their limitations and pathologies. The extent to which these approximate methods can be used to study nonadiabatic phenomenon is studied in this thesis.

In the beginning of my graduate school, the state-of-the-art tools and methodology to study photochemistry from first principles were the following. The gradients of the electronic energy required for the nuclear propagation was available within linear response TDDFT.[17] It was possible to compute the nonadiabatic couplings between the ground and any excited state

from linear response TDDFT,[18,19] and their performance to study photochemistry of systems essentially involving two electronic states was documented.[19,20] While transition properties between two excited states was possible to be extracted from quadratic response TDDFT,[21] the severity of the unphysical divergences in the state-to-state properties was unknown. Fewest switches surface hopping (FSSH)[22] was used to study nonadiabatic dynamics, and several improvements to the methods had been suggested,[23-33] and was demonstrated to be improvements over the original algorithm for low-dimensional model problems. No direct comparison of the methods was made for ab-initio simulations.

This thesis is structured as follows. The accuracy of density functional theory (DFT) to model the electronic states was studied in chapter 2. Using DFT, it was possible to assign the electronic structure of the first square-planar actinide complex synthesized. Agreement between experimental and the calculated molecular structure as well as the UV-Vis spectrum calculated using time-dependent DFT (TDDFT), provided confidence in the assignment of the unusual singly-occupied d_{z^2} highest occupied molecular orbital (HOMO) for the thorium(III) square-planar complex.

Emboldened by the success of DFT as a means to model the electronic states, the nonadiabatic dynamics of 5-methoxyquinoline was studied using DFT and is presented in chapter 3. To model the nonadiabatic dynamics, the FSSH[22] method was used for the nuclear motion. The study revealed an alternate mechanism for the photobasicity of 5-methoxyquinoline, contrary to the commonly accepted Förster theory[34] for photoacidity and photobasicity.

While linear response theory is adequate for extracting the approximate electronic excitation energies, gradients and the couplings between the ground and the excited states, quadratic response theory is required to extract the couplings between the excited states. However, spurious poles present in the quadratic response function cause unphysical divergences of the transition properties.[35] These unphysical divergences are, however, removed when a pseudowavefunction approximation to the quadratic response vectors is introduced. Enabled

with robust methods for calculating the electronic properties, it was possible to study the photochemistry of thymine, which shows a transfer of nuclear populations between multiple electronic states. Presented in chapter 4, we discuss the accuracy of TDDFT/FSSH methodology in predicting the excited state lifetimes of thymine. This chapter also discusses the limitations of our methods, especially the inconsistency in the swarm and the electronic populations in thymine. FSSH is known to have overcoherent electronic amplitudes, and the discrepancy provides motivation to study the effects of decoherence correction to FSSH.

Two decoherence corrections to FSSH were introduced and its effect on the nonadiabatic dynamics of thymine and isocytosine was studied and is presented in chapter 5. The limitations of the method described in chapter 4 are revisited and the sources of errors in the methodology are critically evaluated and tested against other available methods for NAMD presented in the literature.

Gaining control over the processes involved in transferring electronic excitation energy into chemical bonds remains elusive. One of the many ways we might be able to understand the processes is through simulations, which require careful and rigorous implementation of approximate methods, requiring regular testing and reevaluation. The tools and software necessary to study these processes through simulations are important to build and maintain. The data and the scientific discussion presented in this thesis is a consequence of building such software. In conclusion, it will be discussed how the tools developed to produce, collect and analyze the data presented in this thesis, will help answer questions of global interests in future, which is beyond the scope of this study.

Chapter 2

Use of DFT to understand the electronic structure of the first synthesized square-planar thorium(III) complex

This chapter contains verbatim excerpts from Huh, D. N.; Roy, S.; Ziller, J. W.; Furche, F.; Evans, W. J. Isolation of a Square-Planar Th(III) Complex: Synthesis and Structure of [Th(OC$_6$H$_2$^{t}Bu$_2$-2,6-Me-4)$_4$]$^{1-}$. *J. Am. Chem. Soc.*, 2019, **141**, 12458–12463. Copyright (2019) American Chemical Society.

2.1   Introduction

Although Th(IV) alkoxide complexes were synthesized in the 1950s by Bradley and co-workers,[36–39] it was not until the 1980s that Th(IV) aryloxide complexes were reported by Lappert.[40,41] In 1992, Clark and Sattelberger isolated the first homoleptic Th(IV) aryloxide complex, Th(OC$_6$H$_3$^{t}Bu$_2$-2,6)$_4$, which had the expected tetrahedral geometry.[42]

In contrast, neither alkoxides nor aryloxides of Th(III) have been reported. Crystallographically characterizable Th(III) complexes are rare in general, and most contain cyclopentadienyl ancillary ligands. There are only 10 structurally characterized examples: $[K(DME)_2]$ Th $[\eta_8\text{-}C_8H_6(SiMe_2{}^tBu)_2]_2$,[43] $[C_5H_3(SiMe_2{}^tBu)_2]_3Th$,[44] $[C_5H_3(SiMe_3)_2]_3Th$,[44] $(C_5Me_5)_2Th[^iPrNC(Me)N^iPr]$,[45] $(C_5Me_4H)_3Th$,[46] $[K(18\text{-crown-}6)(Et_2O)]\{[C_5H_3(SiMe_3)_2]_2 ThH_2\}_2$,[47] $[K(18\text{-crown-}6)(THF)]$ $[(C_5Me_5)_2ThH_2]_2$,[47] $(C_5Me_5)_3Th$,[48] $(C_5H_3{}^tBu_2)_3Th$,[49] and $(C_5H_3{}^tBu_2)_2Th(\mu\text{-H})_3AlC(SiMe_3)_3$.[50] Gambarotta attempted to reduce $Th[OC_6H_3(Ph)_2\text{-}2,6]_4$ with potassium but isolated only the Th(IV) hydroxide compound $[K(18\text{-crown-}6)(THF)_2][Th(OC_6H_3(Ph)_2\text{-}2,6)_4(OH)(THF)]$.[51] We report here the first examples of Th(III) aryloxides and their unusual structure.

Treatment of a colorless THF solution of $Th^{IV}(OAr')_4$ $(OAr' = OC_6H_2{}^tBu_2\text{-}2,6\text{-Me-}4)$ (**1**) with KC_8 at room temperature forms a dark-purple solution similar to those of $(C_5Me_4H)_3Th$,[46] $(C_5Me_5)_3Th$,[47] and $(C_5Me_5)_2[^iPrNC(Me)N^iPr]Th$.[45] The product crystallizes from a THF/Et_2O solution to form dark-purple crystals that were structurally characterized as $[K(THF)_5(Et_2O)][Th^{III}(OAr')_4]$ (**2**) (eq 2.1) and Figure 2.1). Treatment of **1** with Li metal did not immediately form a dark solution, but after storage at -35 $^\circ$ C overnight, a purple solution was present. Crystallization from THF/Et_2O yielded $[Li(THF)_4][Th^{III}(OAr')_4]$ (**3**) (eq 1 and Figure 2.2) as large dark-purple blocks that had to be cut for X-ray diffraction. Reactions with cesium also formed a dark-purple solution, but attempts

to crystallize the reduction product yielded intractable colorless solids.
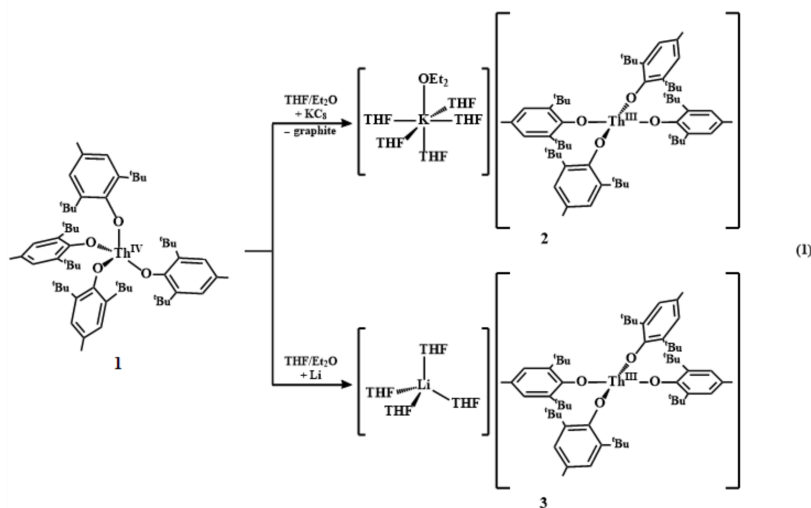
$$Scheme \qquad (2.1)$$
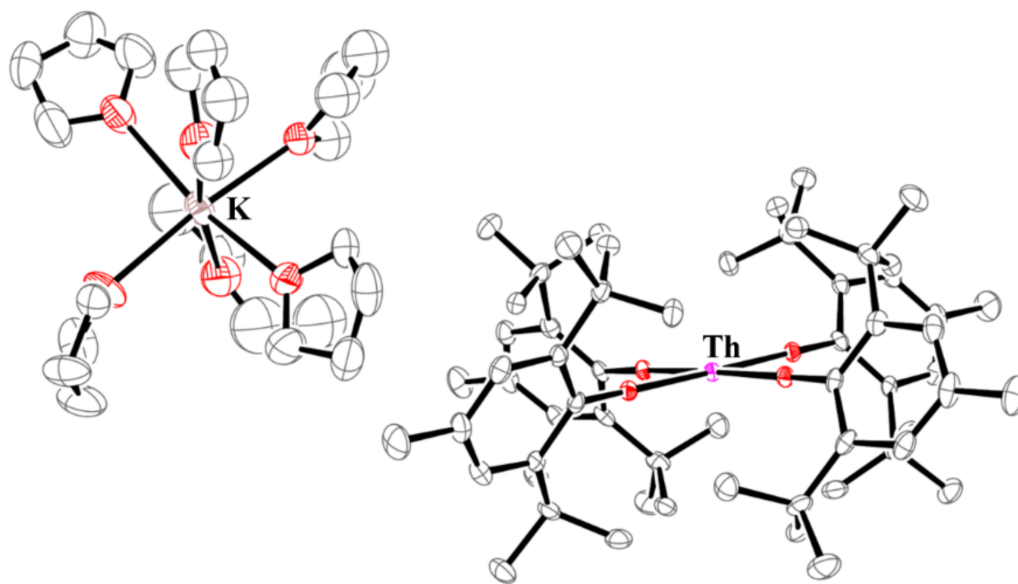
Figure 2.1: ORTEP representation of $[K(THF)_5(Et_2O)][Th(OAr')_4]$ (**2**) with a side-on view and thermal ellipsoids drawn at the 50% probability level. Hydrogen atoms have been omitted for clarity.

The $[Th^{III}(OAr')_4]^{1-}$ anions are the first examples of square-planar geometry in f element chemistry. The closest example to our knowledge is the $U^{IV}[N(C_6F_5)_2]_4$ complex of Schelter.[52] That U(IV) com-
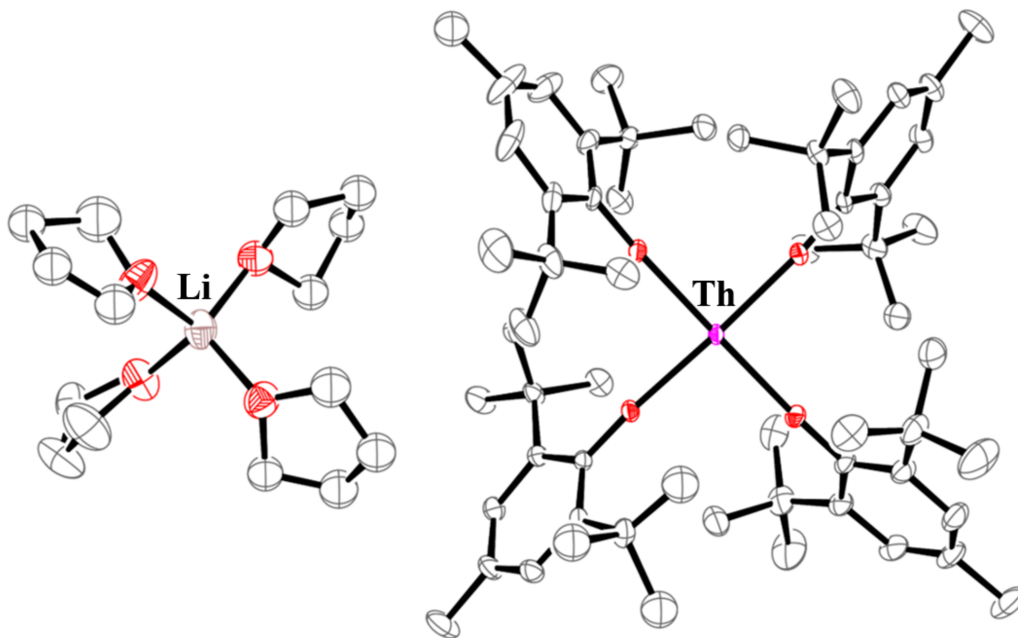
Figure 2.2: ORTEP representation of [Li(THF)$_4$(Et$_2$O)][Th(OAr')$_4$] (**2**) with a side-on view and thermal ellipsoids drawn at the 50% probability level. Hydrogen atoms have been omitted for clarity.

plex has a square-planar array of nitrogen donor atoms enforced by additional fluorine–uranium interactions that make it formally eight-coordinate. The U(III) complex {K[U^{III}(OC$_6$H$_2$^{t}Bu$_2$-2,6)$_4$]}$_n$, synthesized by Arnold, has a tetrahedral array of oxygen donor atoms.[53]

Table 2.1 summarizes the metrical parameters of **2** and **3**. The [K(THF)$_5$(Et$_2$O)]$^{1+}$ and [Li(THF)$_4$]$^{1+}$ countercations are well-separated from the square-planar anion. The Th(III) ion and four oxygen donor atoms are coplanar to within <0.05 Å. The O–Th–O angles range from 88.9(1) to 90.5(2) ° for the cis ligands and from 175.45(1) to 179.6(2)° for the trans ligands. Interestingly, the Th–O–C(ipso) angles in **2** and **3** range from 173.9(2) to 178.6(4)°. In contrast, the tetrakis(aryloxide) complexes of Th(IV), [Th^{IV}(OC$_6$H$_3$^{t}Bu$_2$-2,6)$_4$] (**4**)[42] and [Th^{IV}(OC$_6$H$_3$Ph$_2$-2,6)$_4$] (**5**),[51] have bent Th–O–C angles of 153.5(10) ° and 152.8(7) to 170.7(7) °, respectively (Table 2.1). The 2.235(3)–2.260(3) ÅTh(III)–O distances are longer than the 2.177(7)–2.211(9) ÅTh(IV)–O distances in **4** and **5**. It is well-established that M–O distances do not necessarily correlate with M–O–C(ipso) angles,(19–21) but this comparison is complicated by the difference in oxidation state.

8

	2	**3**	**4**	**5**
Th–O	2.235(3)	2.238(2)	2.189(6)	2.177(7)
	2.239(3)	2.244(2)		2.187(10)
	2.257(3)	2.244(2)		2.189(8)
	2.260(3)	2.247(2)		2.211(9)
O–C(ipso)	1.349(6)	1.355(4)	1.341(19)	1.34(1)
	1.355(6)	1.355(4)		1.35(1)
	1.356(6)	1.358(4)		1.354(8)
	1.371(6)	1.358(4)		1.36(1)
Th–O–C(ipso)	174.2(3)	173.9(2)	153.5(10)	152.8(7)
	176.1(3)	174.7(2)		152.8(7)
	178.5(3)	174.7(2)		155.6(7)
	178.6(4)	176.5(2)		170.7(7)
Th–O4(plane)[1]	0.004	0.031		
C_6 torsion angle[2]	63.21–65.10	58.46–61.81		

Table 2.1: Selected Bond Distances (Å) and Angles (deg) of $[K(THF)_5(Et_2O)][Th^{III}(OAr')_4]$ (**2**), $[Li(THF)_4][Th^{III}(OAr')_4]$ (**3**), $[Th^{IV}(OC_6H_3{}^tBu_2\text{-}2,6)_4]$ (**4**),[42] and $[Th^{IV}(OC_6H_3Ph_2\text{-}2,6)_4]$ (**5**)[51]

2.2 Density functional calculations

The molecular structure of the anion of **2** was optimized starting from the X-ray structure using the TPSS meta-generalized gradient approximation (meta-GGA) functional[54] along with Grimme's D3 dispersion correction.[55] Small-core scalar-relativistic effective core Stuttgart-Cologne potentials (ECPs)[56] were used for Th along with the corresponding valence basis sets.[57] Polarized split valence basis sets def2-SVP[58] were used for oxygen, and group optimized single-ζ bases[58] were used for all other atoms. Fine (size m4[59]) quadrature grids along with the resolution-of-the-identity approximation[60] were used throughout. The conductor like screening model (COSMO)[61] was used to model THF solution ($\epsilon = 7.520$).[62] Ground state energies were converged to 10^{-7} Hartrees. For structural optimization, the DFT gradients were calculated including the derivatives of the quadrature weights for the density grid and converged to a maximum gradient norm of $<10^{-4}$ au. Unconstrained optimization of the anionic Th(III) species resulted in a C_2 symmetric structure. Two structures were optimized for the neutral Th(IV) species. Starting from a S_4 symmetric structure the neutral Th(IV) species optimized to a tetrahedral structure. Optimizing the Th(IV) species starting from the C$_2$ structure resulted in a square planar structure. Attempts to converge structures with

tetrahedral Th(III) coordination were unsuccessful. Mulliken population analysis is used to analyze the frontier molecular orbitals. As expected, the 6d orbitals show a single radial node (since the ECP accounts for the 3d and the 4d orbitals). Numerical second derivative calculations were carried out to confirm that the optimized C_2 and S_4 structures are minima. Electronic excitation spectrum for the anionic C_4 structure was computed using time-dependent density functional theory (TD-DFT) with the Perdew-Burke-Ernzerhof hybrid PBE0[63] and the hybrid TPSSh functional[54], TD-DFT calculations were carried within C_4 symmetry and 8 excitations of A and 7 excitations of E irreducible representation (IRREP) were evaluated using both the group optimized single-ζ bases and the def2-SV(P)[58] bases for all the ligand atoms. The UV-Vis line spectrum was broadened by superimposing Gaussian functions of RMS line width of 0.1 eV. The TPSSh spectrum was blue shifted by 0.15 eV and the PBE0 spectrum with the def2-SV(P) bases were blue shifted by 0.075 eV. The excitation corresponding to the peak near 483 nm is a charge transfer excitation and hence is sensitive to the extent of exact-exchange in the hybrid functional as well as the incompleteness error arising from the basis sets.

Structures of $[PtCl_4]^{2-}$ and $[PdCl_4]^{2-}$ complexes were optimized using TPSS functional and triple-ζ def2-TZVP basis sets along with small-core ECPs.[56] COSMO was used to model water as solvent ($\epsilon = 80.1$).[64] The optimized structures assumed D_{4h} symmetry. The relative d-orbital energies are reported in Tables 2.3 and 2.4. All calculations were performed using Turbomole V7-3.[65]

2.3   Results

The neutral complex **1** as well as the anions in **2** and **3** were studied using density functional theory (DFT). For the neutral compound, two qualitatively different minimum-energy structures were identified: an S_4-symmetric structure with a tetrahedral Th coordination environment and a C_1-symmetric structure with square-planar coordination of Th. The square-planar geometry for Th(OAr')$_4$ is less stable than the tetrahedral structure by 11 kcal/mol (Table 2.2). This is the expectation based on steric factors, and it matches the structures of **4** and **5**. For $[Th(OAr')_4]^{1-}$, the

	Square planar	Tetrahedral (S_4)
[Th(OAr')$_4$]$^{1-}$	0	33
Th(OAr')$_4$	44	29

Table 2.2: Computed relative energies (kcal/mol) of the S_4-symmetric minimum of **1**, C_1-symmetric minimum of the neutral species from **2** and the C_4-and S_4-symmetric minima of anion of **2** and **3** .

calculations show that the square-planar structure is lower in energy than the tetrahedral structure by 33 kcal/mol. Addition of an electron to tetrahedral Th(OAr')$_4$ is endothermic and yields a positive highest occupied molecular orbital (HOMO) energy, indicating that tetrahedral Th(OAr')$_4$ cannot be reduced. The calculated square-planar C_4-symmetric structure of the anion agrees with the X-ray diffraction data within error margins typical of the current methodology, approximately 0.01 Åin covalent bond distance and a few degrees in bond angles. The O–Th–O bond angles are calculated to be 90° and 180° for the cis and trans ligands, respectively, and the Th–O$_4$(plane) distance is calculated to be zero within the accuracy of the present approach. The 2.245 Åcalculated Th–O bond length and the 1.376 ÅO–C distance are similar to those in Table 2.1. The nearly linear Th–O–C(ipso) angles are predicted to be 178°. The calculated 57° C$_6$ torsion angle matches the angular arrangement of the ligands found in the structures.

Mulliken population analysis of the HOMO from the DFT calculations on [Th(OAr')$_4$]$^{1-}$ suggests that it is predominantly $6d_z^2$ in character (Figure 2.3) with some 7s-type Rydberg admixture, which is allowed in C$_4$ symmetry.[66] Although d_{z^2} is usually not the energetically lowest d orbital in square-planar geometry, there are examples, such as [PtCl$_4$]$^{2-}$,[67,68] where metal orbitals with d_{z^2} character are energetically the most stable, particularly for ligands with π-donating lone pairs. To update the calculations from 1958[67] and 1983,[68] [PdCl$_4$]$^{2-}$ and [PtCl$_4$]$^{2-}$ were examined by modern methods to confirm the conclusion of a low-lying d_{z^2} orbital (see Tables 2.3 and 2.4).

In [Th(OAr')$_4$]$^{1-}$, the doubly occupied π lone pairs repulsively interact with the d_{xy} orbital as well as the degenerate d_{xz} and d_{yz} orbitals. Schrock *et al.*[69] synthesized a square-planar d^2 W(IV) complex, W(OC$_6$H$_3$^{i}Pr$_2$-2,6)$_4$, that Hoffman *et al.*[70] described as having the doubly occupied π lone pairs repulsively interacting with the d_{xy}, d_{xz}, and d_{yz} orbitals. Hayton *et al.*[71] described similar
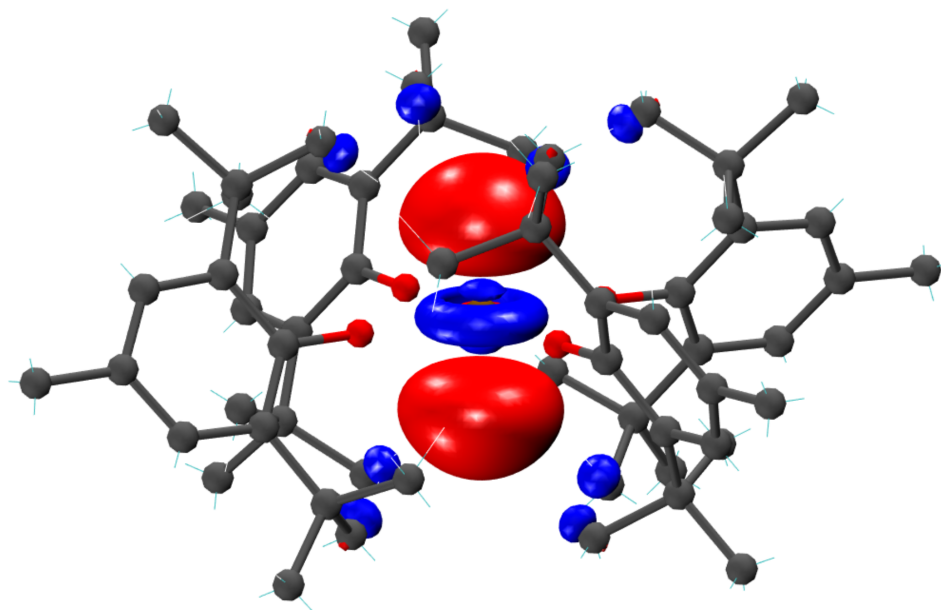
Figure 2.3: HOMO of $[Th(OAr')_4]^{1-}$ plotted with an isovalue of $\pm$ 0.05 au. See Table 2.5 for population analysis.
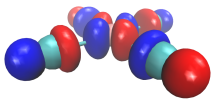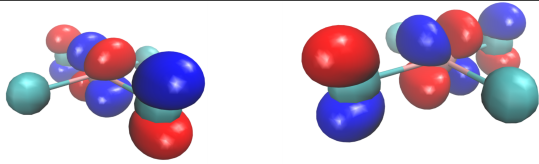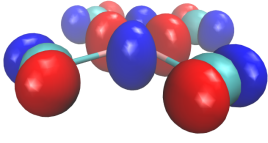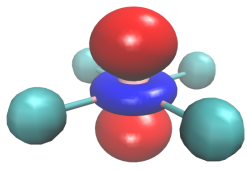
Orbital	Orbital energy (eV)	Molecular orbital plot (isovalue=0.05 au)
6b1g	-2.1	
3eg	-4.64	
3b2g	-4.89	
7a1g	-5.11	

Table 2.3: d-orbital splitting in square planar structure for $[PtCl_4]^{2-}$ using TPSS density functional and triple-ζ bases.
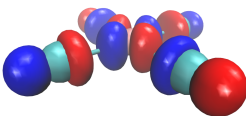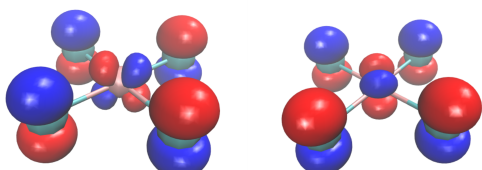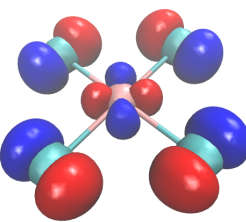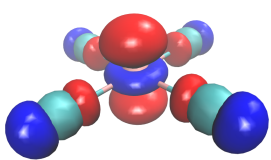
Orbital	Orbital energy (eV)	Molecular orbital plot (isovalue=0.05 au)
6b2g	-2.09	
3eg	-4.99	
3b1g	-5.24	
7a1g	-5.29	

Table 2.4: d-orbital splitting in square planar structure for $[PdCl_4]^{2-}$ using TPSS density functional and triple-ζ bases.

behavior in a pseudo-square-planar d^4 Fe(IV) ketimide, [Fe(N=C^{t}Bu$_2$)$_4$], where the π-lone pairs of the ketimide repulsively interact with the degenerate d_{xz} and d_{yz} orbitals. Figure 2.4 shows the orbitals responsible for this effect in [Th(OAr')$_4$]$^{1-}$. A qualitative molecular orbital diagram of the [Th(OAr')$_4$]$^{1-}$ anion displaying important frontier molecular orbital energies is shown in Figure 2.5. To our knowledge,[72] this is the first $6d^1$ square-planar complex.
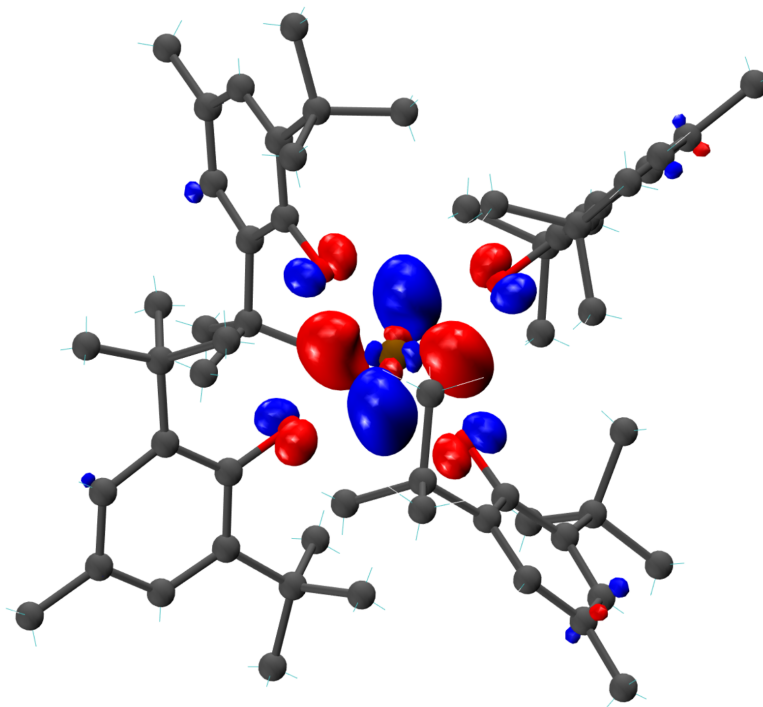
Figure 2.4: Example of antibonding orbitals of [Th(OAr')$_4$]$^{1-}$ (isovalue = $\pm$ 0.05 au) involving the π orbitals on oxygen and the d_{xy} orbital on thorium.

The UV-Vis spectrum of **2** (Figure 2.6) shows two absorption bands at 483 and 581 nm with high extinction coefficients (ϵ = 4000 and 5000 M^{-1} cm^{-1}, respectively) and a more intense peak at 320 nm (ϵ = 9000 M^{-1} cm^{-1}). The simulated spectrum calculated using time-dependent DFT (Figure 2.6) suggests that the two broad peaks in the visible spectrum arise from several transitions originating from the $6d_{z^2}$ orbital. The 581 nm peak corresponds to symmetry-allowed metal-centered transitions into orbitals with significant 5f character, whereas the 483 nm band has additional metal-
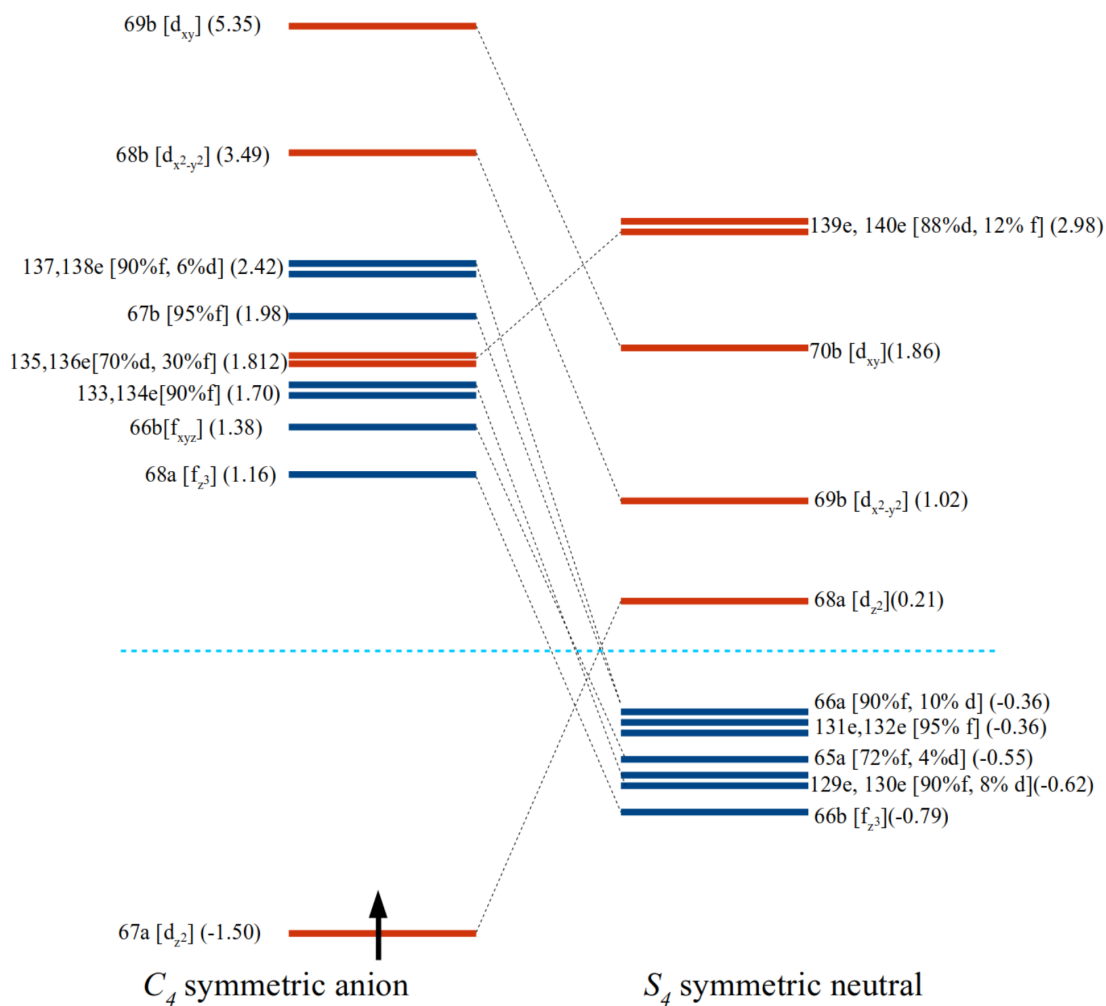
Figure 2.5: Simplified frontier molecular orbital diagram of $[\text{Th}(\text{OAr'})_4]^{1-}$ showing α spin orbitals with strong Th character. Red and blue levels represent computed energies of predominantly d and f orbitals, respectively; numerical values in eV are given in parentheses. The dashed blue line denotes zero orbital energy. Atomic orbital designations are reported in brackets whenever possible.

to-ligand charge transfer character. The intense absorption near 320 nm is attributed to a transition from the $6d_{z^2}$ orbital to a diffuse p-type Rydberg orbital (Figure 2.7).
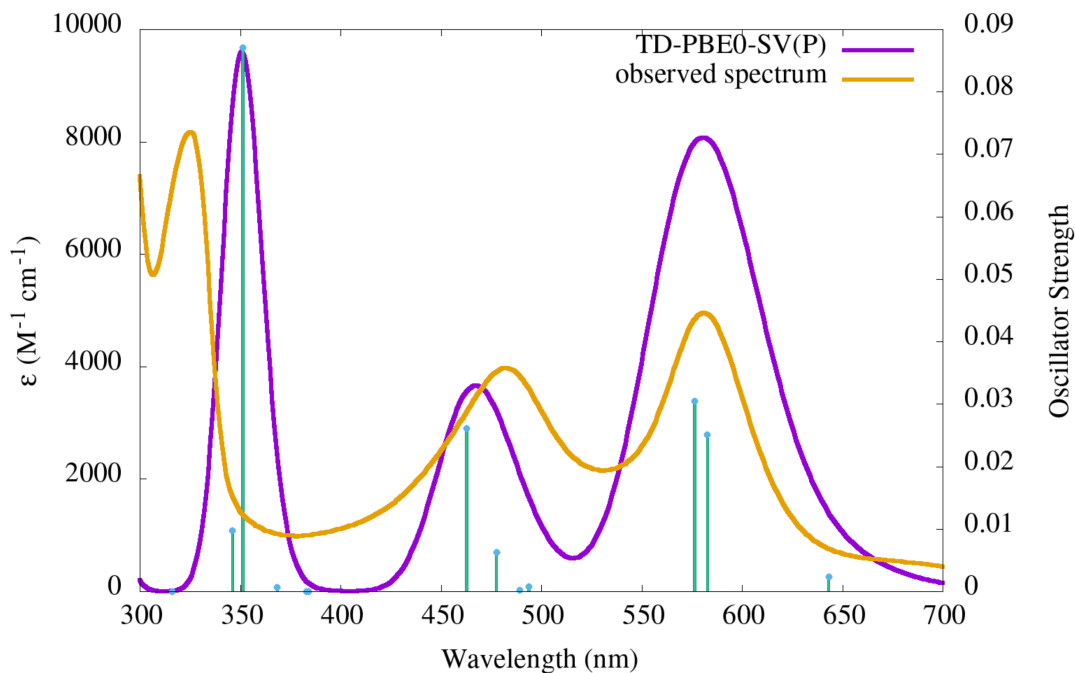
Figure 2.6: Observed UV-Vis spectrum of $[K(THF)_5(Et_2O)][Th(OAr')_4]$ (**2**) in THF (700 μM) (yellow) and simulated UV−vis spectrum of $[Th(OAr')_4]^{1-}$ (purple) with the excitations shown as vertical lines. Calculated extinction coefficients are scaled down by a factor of 1.5.

The square-planar coordination geometry in $[Th(OAr')_4]^{1-}$ was surprising given that tetrahedral geometry is sterically favored and the electron configuration of the new complex is not one of the d^7–d^9 electron configurations that electronically favor square-planar geometries au.[73–75] It is possible that the arrangement of the eight tert-butyl groups is optimized with the OAr' ligands in a square-planar array, although most eight-coordinate structures are similar in energy.[76,77] The eight tert-butyl tertiary carbon atoms define a square antiprism, which is one of the several common geometries for ML_8 compounds and M_8L_x clusters.

Dispersion forces between the tert-butyl groups may also lead to the square-planar geometry. The importance of dispersion forces in inorganic chemistry has recently been thoroughly summarized.[78] It has also been previously shown that the tert-butyl-substituted trityl compound $[C(C_6H_3\text{-}3,5\text{-}^tBu_2)_3]_2$ has significant dispersion forces, which give it a simple dimeric structure and a melting point of 214°![79–81] The C(Me)...C(Me) distances between the tert-butyl groups in $[Th(OAr')_4]^{1-}$
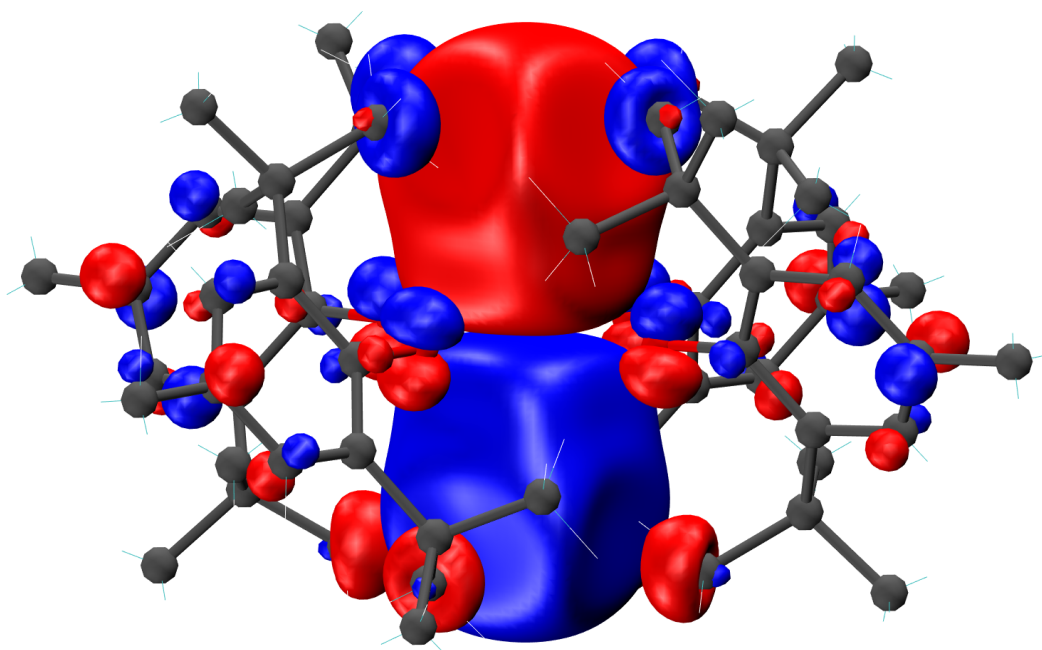
Figure 2.7: Rydberg orbital 71 a (2.73 eV) plotted with isovalue = ± 0.02 au. The band located at 321 nm in the UV-visible spectrum results predominately from a transition out of the d_{z^2} HOMO into 71 a.

are as low as 3.30(1) to 3.55(1) , which are well below the 3.95(2)–4.15(2) range of distances in [C(C$_6$H$_3$-3,5-^{t}Bu$_2$)$_3$]$_2$.[79–82] Consistent with this, the closest H(CMe3)…H(CMe3) distances in **2** and **3** are in the 2.21–2.35 range, which is less than twice the sum of the 1.2 van-der-Waals radius of hydrogen. However, calculated structures optimized without dispersion corrections showed little difference from calculated structures optimized with dispersion corrections.

The main difference in the electronic structure of the square-planar and tetrahedral coordination geometries is the accessibility of a low-lying Th orbital with 6d/7s character in the square-planar geometry. This suggests that the main driving force for the reorganization of the structure upon reduction from Th(IV) to Th(III) is a gain in ligand field stabilization energy for a 6d^1 configuration in the square-planar coordination geometry relative to the tetrahedral one. The calculations also revealed different orientations of the tert-butyl groups for the tetrahedral and square-planar cases. In the tetrahedral geometry, one C–Me bond of the tert-butyl groups is aligned nearly parallel to the O–Th bonds, whereas it is nearly antiparallel in the square-planar geometry. The latter orientation with more methyl groups near the metal facilitates stronger dispersive interactions and is better accommodated in the anion since the Th–O distances are longer for Th(III) than for Th(IV).

In summary, a square-planar geometry is accessible to thorium in the +3 oxidation state with suitable ligands. The aryloxide ligands, which are π-donors, favor the formation of a square-planar d^1 complex with a low-energy d$_{z^2}$ orbital. This geometry, which is unusual for an f element and for d^1 complexes, is likely also favored by the positioning of the eight tert-butyl substituents on the four aryloxide ligands.

2.4 Appendix

Orbital	Orbital energy (eV)	Spin occupied	s contribution	p contribution	d contribution	f contribution
67 a	-1.95	alpha	0.33	0.00	0.50	0.00
68 a	1.75	alpha	0.00	0.35	0.07	0.55
71 a	3.24	alpha	0.00	0.29	0.00	0.47
72 a	3.75	alpha	0.85	0.00	0.00	0.00
66 b	2.22	alpha	0.00	0.00	0.03	0.99
67 b	2.81	alpha	0.00	0.02	0.04	0.89
68 b	4.06	alpha	0.00	0.00	0.68	0.01
69 b	4.11	alpha	0.00	0.00	0.40	0.00
133,134 e	2.49	alpha	0.00	0.02	0.06	0.89
135,136 e	2.65	alpha	0.00	0.00	0.45	0.17
137,138 e	3.19	alpha	0.00	0.00	0.01	0.71
67 a	0.82	beta	0.38	0.00	0.41	0.00
70 a	2.45	beta	0.00	0.22	0.00	0.64
71 a	3.50	beta	0.00	0.40	0.00	0.33
72 a	3.82	beta	0.84	0.01	0.01	0.00
66 b	2.28	beta	0.00	0.00	0.00	0.99
67 b	2.85	beta	0.00	0.00	0.03	0.90
68 b	4.10	beta	0.00	0.00	0.69	0.01
69 b	5.93	beta	0.00	0.00	0.38	0.00
133,134 e	2.48	beta	0.00	0.02	0.10	0.88
135,136 e	2.65	beta	0.00	0.03	0.64	0.18
137,138 e	3.25	beta	0.00	0.04	0.04	0.69

Table 2.5: Mulliken population analysis of selected molecular orbitals of anionic $[\text{Th(OAr')}_4]^{1-}$ centered on Th.

Chapter 3

5-Methoxyquinoline photobasicity is mediated by water oxidation

This chapter contains verbatim excerpts from Roy, S.; Ardo, S; Furche, F. 5-Methoxyquinoline Photobasicity is Mediated by Water Oxidation. *J. Phys. Chem. A*, 2019, **123**, 6645–6651. Copyright (2019) American Chemical Society.

3.1 Introduction

Brønsted acids whose acidity increases significantly upon photoexcitation are commonly called photoacids[83]; analogously, photobases can be defined as Brønsted bases whose basicity increases upon photoexcitation.[84,85] Applications of photoacids and -bases include photolithography,[86] photopolymerization,[87] probes in structural biology,[88] and functional materials for light-to-ionic energy conversion.[89]. The concept of photoacidity or -basicity is based on the Förster cycle[34], a closed thermodynamic cycle which postulates two different acid-base equilibria, one for the ground and one for the excited electronic state, see Figure 3.1. If the excited-state lifetime is long compared to acid-base equilibration, the change in acidity upon photoexcitation, ΔpK_a, can be obtained, in the

simplest case, from the change in E_{00} emission energies from the excited-state photoacid and its conjugate base, ΔE_{em},[90,91] according to

$$\Delta pK_a = \frac{\Delta E_{em}}{RT \ln 10},$$ (3.1)

where R is the ideal gas constant and T denotes temperature. Molecules whose excited state lifetime is long enough to permit acid-base equilibration include naphthols and 8-hydroxy-1,3,6-pyrenesulfonates (HPTS) and its derivatives, with typical excited state lifetimes on the order of 1 ns.[92] The time evolution of proton transfer in such systems has been studied in detail by ultrafast spectroscopy.[83,93]
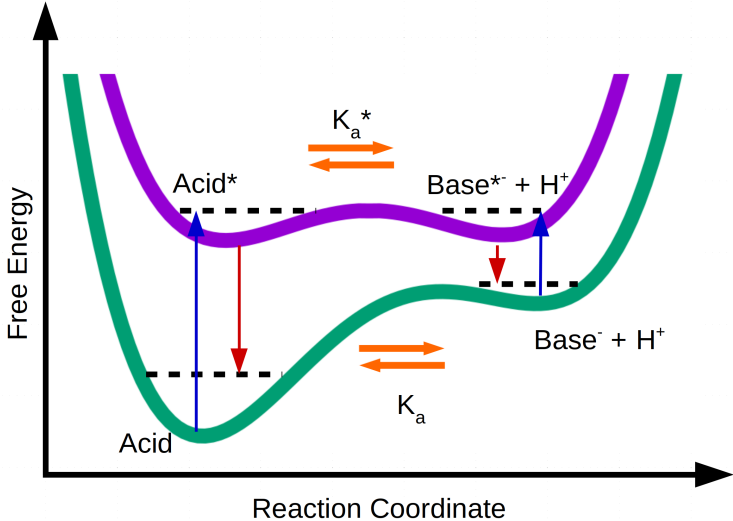
Figure 3.1: Förster cycle assuming excited-state acid-base equilibrium. K_a and K_a^* denote the acid dissociation constants of the ground (green) and excited (purple) electronic state, respectively.

A typical timescale for excited-state proton transfer is 10s of picoseconds (ps) down to few femtoseconds (fs) for "super" photoacids;[93] full equilibration may take considerably longer. However, typical excited state lifetimes for states undergoing ultrafast internal conversion are on the order of fs. As a result, the acidic or basic species inducing proton transfer may differ from the initially Franck–Condon excited species. While the Förster cycle remains valid from a strictly thermodynamic viewpoint, Eq. (3.1) may not be applicable in such a scenario, because observed photoemission may stem from species different from the excited acid or base, or not be observed at all. The term

"photoacid generator"[94] has been coined for chromophores whose photodegradation produces acidic species; however, the mechanism leading to generation of acidic or basic species, as well as their chemical composition, are often unknown.

Recent advances in nonadiabatic molecular dynamics (NAMD) simulations and excited-state electronic structure methods[20,95,96] enable *ab initio* studies of ultrafast excited-state dynamics and decay processes, providing detailed pictures of the mechanisms underlying photoacidity. For example, pioneering work by Domcke and Sobolewski[97,98] established the critical role of solute to solvent charge-transfer excited states leading to proton transfer via conical intersection with the absorbing state. However, comparatively little is known about the mechanism underlying photobasicity, despite growing experimental interest.[99–101]

Here, we report NAMD simulations using state-of-the-art hybrid time-dependent density functional theory (TDDFT) and fewest switches surface hopping (SH), further supported by second-order algebraic diagrammatic construction [ADC(2)] calculations[102,103] to elucidate the mechanism underlying 5-methoxyquinoline (5-MeOQ) photobasicity. 5-MeOQ was chosen because detailed kinetic data from recent time-resolved fluorescence measurements are available.[101] These data indicated an anomalously short excited state lifetime and no detectable kinetic isotope effect (KIE) in aqueous solution hard to reconcile with the notion of an excited state acid-base equilibrium.

3.2   Methods

3.2.1   Computational details

Nonadiabatic *ab initio* molecular dynamics simulations were carried out on potential energy surfaces generated on-the-fly from density functional theory (DFT) and (TDDFT) using the PBE0 exchange-correlation functional[63] along with Grimme's D3 dispersion correction.[104] All calculations used polarized double -ζ valence def2-SVP[105] basis sets. Analytic gradients for state S_0 and state S_1[17] were computed at each time step along with the analytic derivative coupling between the states.[18]

Resolution-of-the-identity (RI) approximation for the two-electron Coulomb integrals[60] and fine (size m4) grid for the functional integral[59] were used throughout. Nonadiabatic effects were taken into account using the SH method[22] where the classical nuclear propagation was performed using a leap frog Verlet algorithm with a time step of 20 a.u. (~ 0.48 fs).[106]

3.2.2   Sampling

Structures of 5-MeOQ and a cluster of four water molecules were individually optimized in the ground states in gas phase with a threshold of 5×10^{-4} Hartrees/Bohr for the gradient. The water cluster was placed near the nitrogen of 5-MeOQ and the total structure was reoptimized with the same criterion and a conductor-like screening model (COSMO) for solvation.[107] To model an ensemble, 100 trajectories were initiated on the S_1 surface with random velocities contributing to a thermal energy consistent with 1500 K temperature. The initial nuclear coordinates of the trajectories were sampled from a ground state equilibrium dynamics at 300 K on the S_0 surface. To avoid numerical instabilities near a conical intersection, a hop was forced from S_1 to S_0 when the excitation energy became less than 0.5 eV. The total simulation time for all the trajectories was 6.5 ps.

To capture relatively rare proton transfer events on the ps timescale, NAMD simulations were performed at elevated temperatures of 1600 K, 1500 K, and 1400 K. Excited state decay constants were extracted from the simulations, and extrapolated to 300 K using an exponential (Arrhenius) temperature dependence. Based on this analysis, timescales from dynamics simulations obtained at 1500 K were scaled by a factor 290 to obtain estimates for dynamics at the desired temperature of 300 K.

3.2.3   Absorption and emission spectra

The excitation energy obtained using PBE0/SVP for 5-MeOQ was compared with experiments.[99] To demonstrate the applicability of TDDFT, the first excitation energy of several substituted quino-

24

lines were calculated and were found to be in good agreement with experiments (see Supporting Information Figure S1). For the validation of an approaching conical intersection, structures from 10 time steps before and after the point of forced hop of one of the trajectories were considered for analysis using algebraic diagrammatic construction method to second order [ADC(2)][103] calculations. All calculations were performed using a local development version based on Turbomole 7.2.[108]

To simulate the time-dependent emission spectrum, the Einstein coefficient for spontaneous emission A was calculated for each trajectory at every time step according to[109]

$$A = \frac{2c}{a_0} \left(\frac{\Delta E}{m_e c^2} \right)^2 f \tag{3.2}$$

where ΔE denotes the excitation energy, f the oscillator strength, c the speed of light, m_e the electron mass, and a_0 the Bohr radius. The coefficients were fit to a Lorentzian function with a line width of 0.01 eV. The time resolved spectrum was obtained by taking the ensemble average of the Lorentzian functions from the trajectories on the S_1 state at each time step.

3.3   Results

3.3.1   Franck-Condon structure

Close to the Franck-Condon point, the S_1 state corresponds to a bright $\pi \rightarrow \pi^*$ transition in the quinoline moiety. The computed S_1 vertical excitation energy of 300 nm agrees closely with the position of the band maximum in the experimental absorption spectrum, 309 nm.[99] The S_1 state relaxes to a nearby local minimum with a vertical emission energy of 419 nm in the experiment and 359 nm in the PBE0/SVP model. Analysis of the density difference between the S_1 state and the S_0 state reveals that, upon excitation, the quinoline nitrogen gains some electron density perpendicular to the plane of the molecule and loses electron density along the plane of the molecule, resulting in a negligible total charge difference, see Figure S2 in the Supporting Information. Intramolecular

25

charge-transfer excited states of amido character, i.e., with a significant increase of negative charge density on the nitrogen atom, are much higher in energy since they require nitrogen rehybridization and loss of conjugation. Thus, the experimentally observed increase in basicity upon photoexcitation cannot simply be rationalized by intramolecular charge transfer, a first hint that the Förster picture may not apply here.

3.3.2 Nonadiabatic molecular dynamics simulations

In the 100 NAMD trajectories, direct protonation of the π^* excited 5-MeOQ is not observed. Instead, hole transfer from the quinoline moiety to the solvated water molecule closest to the quinoline nitrogen occurs after an initial quasi-equilibration period in 95 out of 100 trajectories, see Figure 3.2. This hole transfer is preceded by a configuration where the accepting water molecule is hydrogen bonded to two neighboring water molecules.

According to the NAMD simulations, the charge separation proceeds through a conical intersection between the S_1 state and a solvent to solute charge-transfer (CT) state roughly corresponding to a 5-MeOQH$^-$ anion and a positively charged water cluster, see Figure 3.3. The migration of the hole is followed by rapid (< 0.5 ps) proton transfer to the quinoline nitrogen driven by the Coulomb attraction between the electron charge on the 5-MeOQ$^-$ moiety and the proton. The resulting singlet diradical state decays almost instantaneously through a second conical intersection to produce 5-MeOQH$^+$ and OH$^-$ in the ground state. Continued propagation of the system in the ground state shows the expected rapid acid-base back reaction producing vibrationally excited neutral 5-MeOQ and water in the ground electronic state.

According to the TDDFT-SH simulations, the rate-determining step is hole injection into an adjacent water molecule, suggesting that the (supersystem) dipole moment should change as the reaction proceeds. Indeed Figure 3.4, shows a dramatic change in direction and magnitude of the dipole moment. A suitable reaction coordinate for this step is not the distance between a proton and the 5-MeOQ nitrogen, but a coordinate describing reorganization of the surrounding water molecules
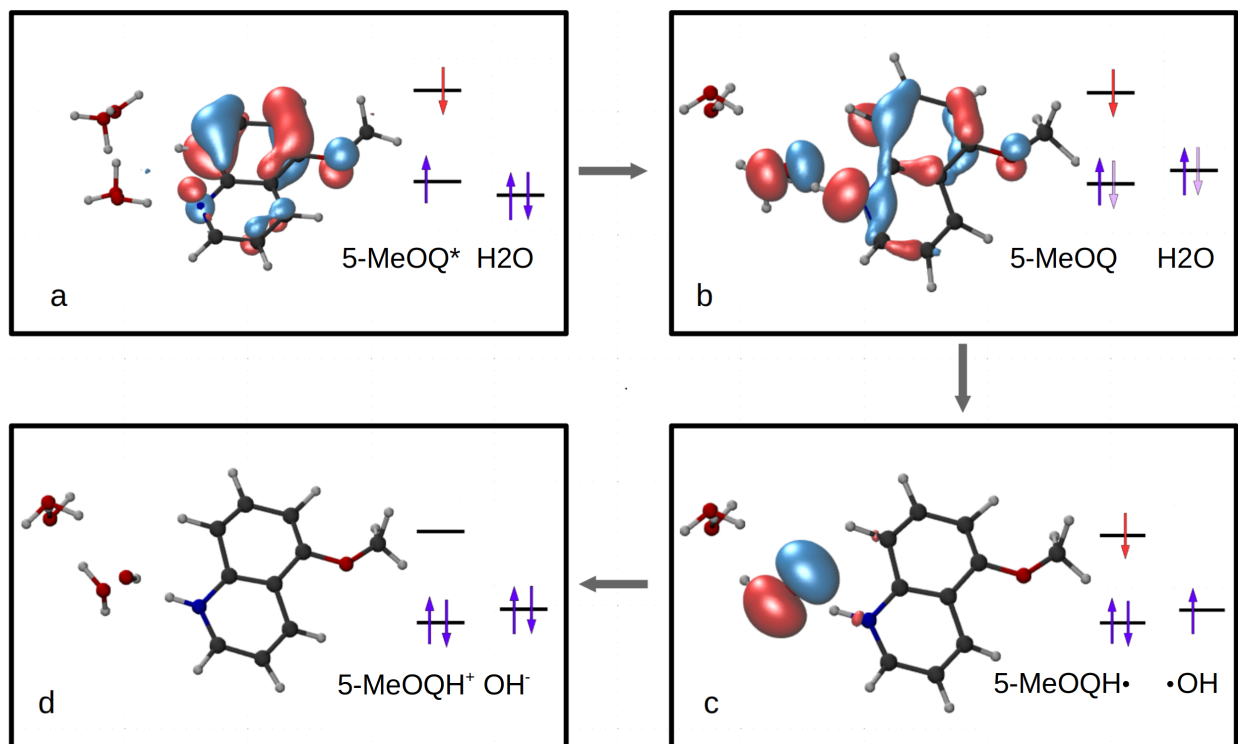
Figure 3.2: Snapshots from a reactive NAMD trajectory illustrating the redox-catalyzed proton transfer mechanism in 5-MeOQ· 4H$_2$O in a simplified molecular orbital picture (contour values: ±0.05 au). (a) Near the Franck-Condon point, the system corresponds to $\pi \rightarrow \pi^*$-excited 5-MeOQ and neutral water molecules. (b) Reorganization of the water molecules enables a partial hole transfer to the water cluster. The resulting charge-transfer state corresponds to a 5-MeOQ$^-$ radical anion and solvated H$_2$O$^+$. (c) As the charge transfer proceeds, the a proton is transferred to 5-MeOQ. (d) The system rapidly decays to the ground state of 5-MeOQH$^+$ and solvated OH$^-$ through a conical intersection.
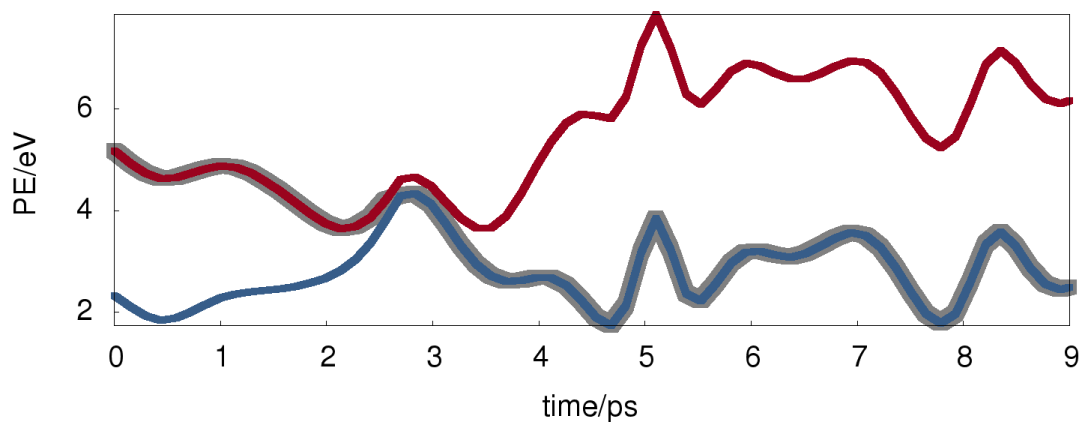
Figure 3.3: Example reactive trajectory displaying relative electronic energy as a function of time for the ground (blue) and S$_1$ (red) states. The active state is highlighted in grey.

during ionization.
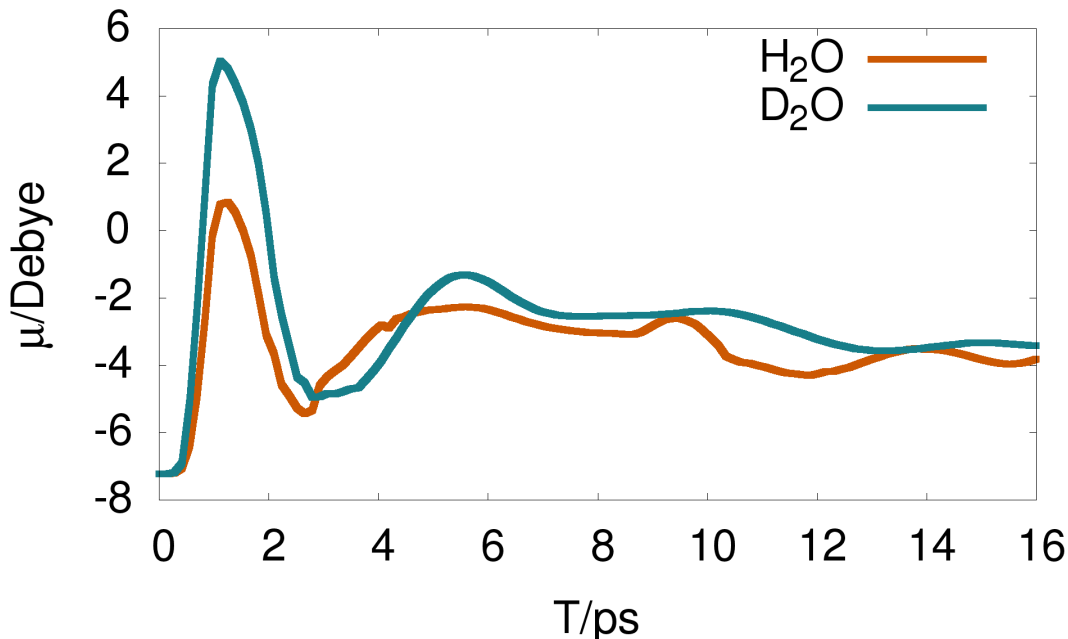
Figure 3.4: Simulated dipole moment of 5-MeOQ along the bridging axis of the quinoline moiety as a function of time averaged over all trajectories. The orange line represents the simulations with H_2O and cyan line for that of D_2O.

3.3.3 ADC(2) calculations

A well-known shortcoming of TDDFT is its tendency to overstabilize charge transfer excited states, especially in conjunction with nonhybrid functionals and long-range charge transfer.[110][111–113] To validate the hole-transfer mechanism suggested by the hybrid TDDFT-SH simulations, single-point ADC(2) calculations were carried out along a trajectory close to the conical intersection with the solvent-to-solute charge transfer state. ADC(2) generally yields accurate charge-transfer excitation energies in cases where TDDFT fails,[114] albeit at increased computational cost relative to TDDFT calculations.

Close to the conical intersection the TDDFT and ADC(2) excitation energies are in qualitative agreement, see Figure 3.5, predicting excitation energies of 0.7 and 0.8 eV close to the charge-transfer geometry. Furthermore, the natural transition orbitals from ADC(2) excitation and TDDFT are

consistent, showing localization of the photohole on the oxygen lone pair as the reaction proceeds. This suggests that the solvent to solute charge transfer observed in the hybrid TDDFT-SH simulations is not an artifact and has physical significance.
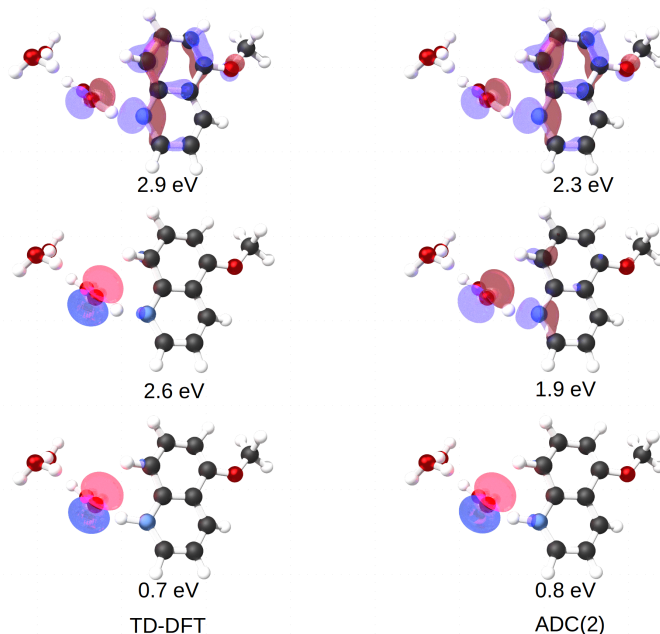
Figure 3.5: ADC(2) NTO hole orbitals (left) compared to PBE0 NTO hole orbitals (right). The structures correspond to 1.1, 0.8 and 0.6 ps before reaching the conical intersection with the ground state. Contour values of ± 0.05 au were used.

3.4 Discussion

3.4.1 Thermodynamic plausibility

The proposed mechanism postulates the formation of a solvated ion pair consisting of an H_2O^+ cation and a 5-MeOQ anion. This is thermodynamically feasible if the electron affinity of excited 5-MeOQ plus the stabilization due to ion pair interaction (exciton binding energy) is larger than the ionization potential of liquid water, see Figure 3.6. PBE0/def2-SVP yields a vertical first electron affinity of 5.8 eV for excited 5-MeOQ at the S_1 state minimum. The ionization potential of liquid water has been estimated to be approximately 6.5 ± 0.5 eV.[115] This argument yields a lower bound

of 0.7 ± 0.5 eV for the excitation energy of the charge-transfer state, which is a plausible range consistent with the TDDFT and ADC(2) results in Figure 3.5.
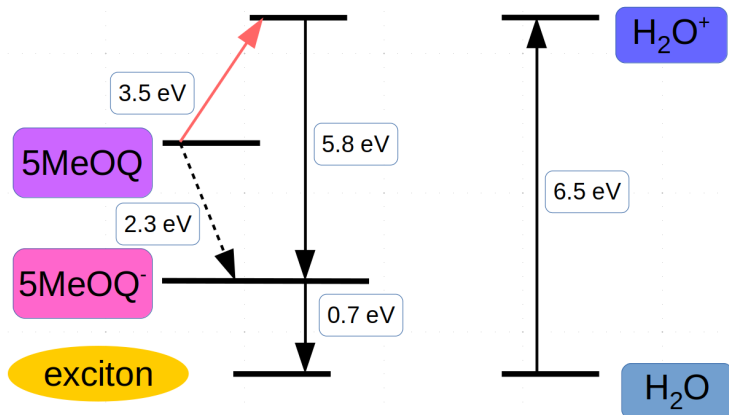
Figure 3.6:   Thermodynamic cycle illustrating plausibility of the hole-transfer mechanism.

3.4.2   Time-Resolved fluorescence and isotope substitution

Time-resolved emission spectra of 5-MeOQ in water and D_2O recently reported by Hunt and Dawlaty[101] yielded an excited-state lifetime of (22 ± 5) ps and a KIE of 0.9 ± 0.3.[101] These results agree well with the simulated time-resolved emission spectra displayed in Figure 3.7, corresponding to an excited-state lifetime of 5 ps and a KIE of 0.8, see Table 3.1 and The proposed mechanism provides a simple explanation for the conspicuous lack of significant KIE of 5-MeOQ decay: The rate determining step is electron rather than proton or deuteron transfer.

Table 3.1: S_1 state lifetimes (ps) obtained from simulated TDDFT-SH and experimental[101] (Exp.) time-resolved fluorescence spectra.

Solvent	TDDFT-SH	Exp.
H_2O	5.1	24 ± 5
D_2O	4.2	22 ± 5

In liquid methanol, much longer excited state lifetimes and a significant KIE were reported, suggesting a different mechanism in non-aqueous solvents.[101] Photochemical oxidation of liquid methanol may require stronger oxidants than 5-MeOQ such as excited 1,3,5-trimethoxybenzene radical cation.[116]
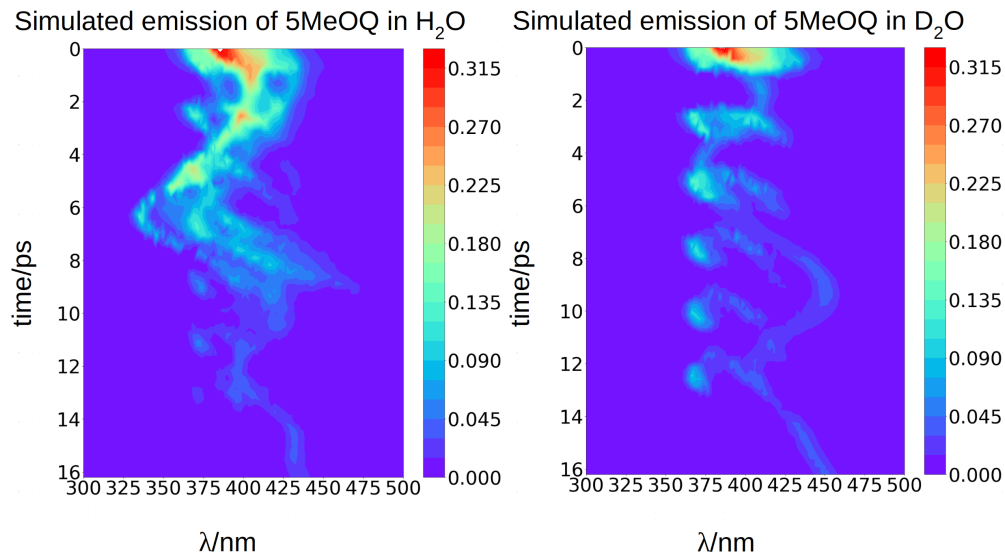
Figure 3.7: Simulated emission spectrum of 5-MeOQ in a) H_2O, b) D_2O.

3.5 Conclusion

The present results do not support previous suggestions[100] that direct protonation of photoexcited 5-MeOQ followed by acid-base equilibration with surrounding water molecules is the main mechanism underlying 5-MeOQ photobasicity in aqueous solution. In particular, (i) the S_1 state of 5-MeOQ has mainly π^* character, showing no appreciable increase in negative charge density at the quinoline nitrogen upon excitation. (ii) The excited-state lifetime, determined experimentally and theoretically to be on the order of 10 ps, is too short acid-base equilibration, and shows no appreciable KIE. Thus, excited state deactivation occurs before the excited conjugate acid species can be formed.

The NAMD simulations lead to an alternative proposal for the mechanism underlying 5-MeOQ photobasicity: Excited 5-MeOQ is apparently a strong enough oxidant to allow hole transfer to an adjacent water molecule in the first solvation shell, inducing rapid protonation of the resulting excited 5-MeOQ$^-$ species and simultaneous electron transfer, resulting in 5-MeOQH$^+$ in the ground state. This does not preclude the possibility that excited 5-MeOQ could be protonated directly from an energetic viewpoint; however, direct protonation cannot compete kinetically with the much faster redox-catalyzed proton transfer mechanism seen in the NAMD simulations. The

available experimental data, including excitations and time-resolved emission spectra, support the hole-transfer mechanism.

Recently, Schlenker and coworkers[117] reported detection of hydroxyl radicals as by-product of proton coupled electron transfer in photoexcited 2,5,8-tris(4-methoxyphenyl)-1,3,4,6,7,9,9b-heptaazaphenalene (TAHz) in the presence of water. This observation can be explained by hole transfer from TAHz to water, followed by a proton transfer to form hydroxyl. The direct observation of hydroxyl radicals in a related system further supports the hypothesis that hole transfer can mediate acid-base reactions. Whereas the resulting charge-transfer state of TAHz-water is long-lived and can be trapped, it is rapidly quenched via proton transfer and deactivation into the ground state in 5-MeOQ-water.

The mechanism reported here provides a plausible explanation for the photobasicity of compounds with exited-state electron affinities similar to or slightly below that of 5-MeOQ and short excited-state lifetime. Such species are strong, electron-rich oxidants, which can rapidly react with redox-active solvents.

Chapter 4

Multistate hybrid time-dependent density functional theory with surface hopping accurately captures ultrafast thymine photodeactivation

4.1 Introduction

Nonadiabatic molecular dynamics[118] (NAMD) using a combination of time-dependent density functional theory[119–124] (TDDFT) and surface hopping[22] (SH) has emerged as a versatile tool for study-

ing and analyzing complex photochemical transformations.[125,20,126] TDDFT-SH has proven capable of predicting the kinetics of pericyclic ring-opening and -closing reactions,[127–135] the reactivity of photoexcited metal oxides[95] such as perovskites[136] and titania,[137–139] and the branching ratios, kinetic energy distributions, and mass distributions of photodissociation reactions.[140,141]

However, the majority of photochemical TDDFT-SH applications to date have included only the ground state and the first excited state. Simulations including several excited states and all nonadiabatic couplings between them have been reported, but rely on approximations with questionable validity such as the neglect of orbital relaxation[142,132,143,144,134,145,146] or single Slater determinant models for the excited state. A rigorous theoretical approach to general couplings between excited states in the TDDFT framework has only recently been devised,[147,21,148] but little is known about its performance in photochemical applications.

Here we report an efficient analytical implementation of state-to-state nonadiabatic couplings and multistate TDDFT-SH dynamics, which builds on these theoretical results and the implementation of the TDDFT quadratic response properties reported by our group previously.[149] All required gradients and couplings can be computed simultaneously; as a result, the computational cost for a multistate NAMD time-step is proportional to that of a ground-state Born–Oppenheimer dynamics step, with a proportionality constant growing sublinearly with the number of electronic states.

We assess the performance of multistate TDDFT by investigating excited state decay of UV-photoexcited thymine. The experimental lifetime of UV-photexcited thymine, 5–7 ps, is significantly longer than that of other photoexcited nucleobases,[150] and its decay has been extensively studied experimentally[150–157] and computationally.[158–161,156,162–166] Nevertheless, the deactivation mechanism of UV-photoexcited thymine remains controversial.[150,158,166] In particular, prior NAMD-SH simulations using multiconfiguration self-consistent field (MCSCF) and the second-order algebraic diagrammatic connection [ADC(2)] methods lead to excited-state lifetimes hard to reconcile with each other and with ultrafast pump-probe experiments.[156,163,165,150]

We summarize the working equations and details of our implementation in Secs. 4.2 and 4.3, followed by the results for thymine excited-state deactivation in Sec. 4.4 and conclusions in Sec. 4.5.

4.2 Nuclear dynamics: Fewest switches surface hopping

Mixed quantum-classical methods treat nuclei classically and expand an auxiliary electronic wavefunction in a few-state (often adiabatic) electronic basis parametrically dependent on the nuclear coordinates.[22] In our implementation, the auxiliary electronic density matrix

$$\hat{\sigma}^{\mathrm{aux}} = \sum_{nm} \sigma_{nm}^{\mathrm{aux}}(t)|\phi_n; \mathbf{R}(t)\rangle\langle\phi_m; \mathbf{R}(t)|, \tag{4.1}$$

is the basic dynamic variable, where $\mathbf{R}(t)$ denotes the nuclear coordinates, $\sigma_{nm}^{\mathrm{aux}}(t)$ are expansion coefficients at time t, and ϕ_n are electronic basis states.[22,167,168] The auxiliary electronic density matrix evolves as

$$\dot{\boldsymbol{\sigma}}^{\mathrm{aux}}(t) = -\mathrm{i}[\bar{\mathbf{H}}, \boldsymbol{\sigma}^{\mathrm{aux}}(t)], \tag{4.2}$$

where $\bar{\mathbf{H}} = \mathbf{H} - \mathrm{i}\mathbf{W}$ is the effective Hamiltonian, $H_{nm} = \langle\phi_n; \mathbf{R}(t)|\hat{H}|\phi_m; \mathbf{R}(t)\rangle$ is a matrix element of the electronic Hamiltonian,

$$W_{nm} = \langle\phi_n; \mathbf{R}(t)|\frac{\partial}{\partial t}\phi_m; \mathbf{R}(t)\rangle = \boldsymbol{\tau}_{nm} \cdot \dot{\mathbf{R}} \tag{4.3}$$

is a nonadiabatic coupling matrix element and

$$\tau_{nm}^{(\xi)} = \langle\phi_n; \mathbf{R}(t)|\frac{\partial}{\partial\xi}\phi_m; \mathbf{R}(t)\rangle \tag{4.4}$$

is the first-order derivative coupling between electronic states n and m.[22]

Within surface hopping, the electronic properties for a given trajectory at any give time are determined by a single Born–Oppenheimer electronic state, here referred to as the active state or active surface.[167] This picture implicitly defines an active electronic density matrix,

$$\sigma_{nm}^{\mathrm{active}} = \delta_{nk}\delta_{mk} \tag{4.5}$$

where k labels the active electronic state. Transitions between electronic states are mimicked through stochastic hops of the active state.

FSSH is a specific realization of the surface hopping framework in which the probability of hopping from active state k to electronic state n in the time interval t to t',

$$g_{k \to n}(t, t') = \int_t^{t'} \mathrm{d}T \times \left(\sigma_{nk}^{\mathrm{aux}}(T) \bar{H}_{kn}(T) - \bar{H}_{nk}(T) \sigma_{kn}^{\mathrm{aux}}(T) \right) / \sigma_{kk}^{\mathrm{aux}}(T) \qquad (4.6)$$

is chosen to reproduce the swarm average population of state k—that is, so $N_k(t)/N_{\mathrm{traj}} \approx \sigma_{kk}(t)$ where $N_k(t)$ is the number of trajectories on active surface k and N_{traj} is the total number of trajectories.[22] In practice, surface hops are decided by computing hopping probabilities according to Eq. (A.13) and generating a uniform random number $\eta \in [0, 1]$. When $\eta < g_{k \to n}$, a surface hop to state n is initiated and the momentum along the derivative coupling vector is rescaled to conserve energy.[22] In case of insufficient kinetic energy, i.e. a frustrated hop, the hop is rejected and no momentum readjustment is performed.

4.3   Electronic dynamics: TDDFT

The NAMD frameworks described above require as input the adiabatic energies of electronic states (E_n), nuclear forces (∇E_n), and derivative couplings ($\tau_{nm}^{(\xi)} \equiv \langle \phi_n | \nabla_\xi \phi_m \rangle$). All of these quantities are computed using (TD)DFT: ground state properties are determined from ground state DFT, excitation energies and derivative couplings between the ground state and an excited electronic state (ground-to-excited-state) are determined from linear response, and excited-state forces and derivative couplings between two excited electronic states (state-to-state) are determined from the quadratic response function.

4.3.1 Linear response

In the TDDFT linear response framework,[119–121,169,170] excitation energies are obtained by solving the eigenvalue problem

$$(\mathbf{\Lambda} - \Omega_n \mathbf{\Delta}) \ket{X^n, Y^n} = 0, \tag{4.7}$$

where

$$\mathbf{\Lambda} = \begin{pmatrix} \mathbf{A} & \mathbf{B} \\ \mathbf{B}^* & \mathbf{A}^* \end{pmatrix} \tag{4.8}$$

is the linear response operator;

$$(A + B)_{ia,jb} = \epsilon_{ab}\delta_{ij} - \epsilon_{ij}\delta_{ab} + 2f^{\mathrm{xc}}_{ia,jb} + 2(ia|jb) - c_x[(ib|ja) + (ij|ab)] \tag{4.9a}$$

$$(A - B)_{ia,jb} = \epsilon_{ab}\delta_{ij} - \epsilon_{ij}\delta_{ab} + c_x[(ib|ja) - (ij|ab)], \tag{4.9b}$$

denote the electronic and magnetic orbital rotation Hessians, respectively;

$$\mathbf{\Delta} = \begin{pmatrix} \mathbf{1} & \mathbf{0} \\ \mathbf{0} & \mathbf{-1} \end{pmatrix} \tag{4.10}$$

is the pseudometric, and Ω_n and $\ket{X^n, Y^n}$ are the eigenvalue (excitation energy) and associated eigenvector of excited state n, respectively.[121,169] Here, indices $i, j, \dots$ denote occupied, $a, b, \dots$ virtual, and $p, q, \dots$ general Kohn-Sham molecular orbitals. Moreover, ϵ_{pq} is an element of the Kohn–Sham matrix which is assumed to be block-diagonal (i.e., the occupied-virtual blocks vanish), $f^{\mathrm{xc}}_{pq,rs}$ is an element of the exchange-correlation kernel, $(pq|rs)$ is an element of the Coulomb operator in Mulliken notation, and c_x is a scalar that interpolates between pure semilocal density functionals ($c_x = 0$) and Hartree–Fock theory ($c_x = 1$, $f^{xc} = 0$). The vast majority of applications use the adiabatic approximation,[171] which replaces the frequency-dependent exchange-correlation kernel with its static limit. The excitation vector for state n encodes the Kohn–Sham ground-to-excited

state transition density matrix

$$\gamma^{0n}(x, x') = \sum_{ia} \left(X_{ia}^n \varphi_i(x) \varphi_a(x') + Y_{ia}^n \varphi_a(x) \varphi_i(x') \right) \tag{4.11}$$

in terms of the Kohn–Sham orbitals φ_p.[170] Eigenvectors of Eq. (4.7) satisfy the orthonormalization condition

$$\langle X^n, Y^n | \boldsymbol{\Delta} | X^m, Y^m \rangle = \delta_{nm}. \tag{4.12}$$

4.3.2   Ground-to-excited-state derivative couplings

First-order derivative couplings between the ground and an excited electronic state within the adiabatic approximation to TDDFT are obtained from a pole analysis of the frequency-dependent linear response of the time-dependent Kohn–Sham wavefunction,[18,147] and are computed together with excited-state gradients as

$$\tau_{0n}^{(\xi)} = \langle \mathbf{D}^{0n,\mathrm{AO}} \mathbf{h}^{(\xi)} \rangle + \langle \mathbf{D}^{0n,\mathrm{AO}} \mathbf{v}^{\mathrm{xc},(\xi)} \rangle - \langle \mathbf{W}^{0n,\mathrm{AO}} \mathbf{S}^{(\xi)} \rangle + \langle \boldsymbol{\Gamma}^{0n,\mathrm{AO}} \mathbf{V}^{(\xi)} \rangle; \tag{4.13}$$

here, the superscript (ξ) indicates partial differentiation, ξ represents the nuclear coordinate of interest, the superscript $\mathbf{M}^{\mathrm{AO}} \equiv \mathbf{CMC}^\dagger$ indicates the quantity is expressed in the AO basis for molecular orbital coefficient matrix $\mathbf{C}$, $\mathbf{h}$ is the one-electron core Hamiltonian, $\mathbf{v}^{\mathrm{xc}}$ is the exchange-correlation potential, $\mathbf{S}$ is the overlap matrix, $\mathbf{D}^{0n}$ is a generalized one-electron transition density, $\mathbf{W}^{0n}$ is a generalized energy-weighted transition density, $\boldsymbol{\Gamma}^{0n}$ is the pair transition density, and $\mathbf{V}$ is the two-electron Coulomb operator defined with $V_{\mu\nu\lambda\kappa} = (\mu\nu|\lambda\kappa)$; Greek indices denote AOs. At variance with Ref. 18, we include in Eq. (4.13) only translationally invariant terms, which is approximately equivalent to employing electron-translation factors.[172,173]

4.3.3 State-to-state derivative couplings

In analogy to the ground-to-excited state derivative couplings, state-to-state derivative couplings are defined through a pole analysis of the quadratic response function. The generator for the derivative coupling between excited states n and m is[147]

$$G_{nm}(\mathbf{C}, \boldsymbol{\epsilon} | \boldsymbol{\gamma^{nm}}, \mathbf{R}) = \langle X^n, Y^n | \Lambda(\mathbf{R}) | X^m, Y^m \rangle / \Omega_{nm} + \langle \boldsymbol{\gamma}^{nm,T} \mathbf{C}^{(0)\dagger} \mathbf{O}(\mathbf{R}) \mathbf{C} \rangle, \qquad (4.14)$$

where $O_{\mu\nu}(\mathbf{R}) \equiv \langle \chi_\mu | \chi_\nu(\mathbf{R}) \rangle$ is a one-sided atomic orbital overlap integral, $|\chi_\mu\rangle$ is an atom-centered Gaussian basis function, the superscript $^{(0)}$ indicates that the quantity is fixed at the zeroth-order solution, $\Omega_{nm} \equiv \Omega_n - \Omega_m$, $\boldsymbol{\gamma}^{nm}$ is the one-particle transition density matrix (1TDM) of the KS system, and dependence on the nuclear coordinates, $\mathbf{R}$, is now denoted explicitly.

Quadratic response theory dictates that the 1TDM in Eq. (4.14) is obtained from

$$\boldsymbol{\gamma}^{nm,\mathrm{QR}} = \begin{pmatrix} -\left(\mathbf{X}^n(\mathbf{X}^m)^T + \mathbf{Y}^n(\mathbf{Y}^m)^T\right) & \mathbf{X}^{nm} \\ (\mathbf{Y}^{nm})^T & (\mathbf{X}^n)^T \mathbf{X}^m + (\mathbf{Y}^n)^T \mathbf{Y}^m \end{pmatrix} \qquad (4.15)$$

where the off-diagonal blocks require the solution of a dynamic-polarizability-like equation,

$$|X^{nm}, Y^{nm}\rangle = -\left(\boldsymbol{\Lambda} - \Omega_{nm}\boldsymbol{\Delta}\right)^{-1} |P^{nm}, Q^{nm}\rangle \qquad (4.16)$$

Explicit expressions for the right-hand-side (RHS) are provided in Ref. 149 and supplied in the appendix for completeness. However, within the adiabatic approximation to the exchange-correlation kernel, the linear response operator in Eq. (4.16) becomes singular when Ω_{nm} approaches any other excitation energy and thus the transition density diverges unphysically.[147,21,148,35,149] Thus, we exclusively use derivative couplings from the pseudowavefunction approximation which is equivalent to ignoring the off-diagonal blocks of the 1TDM in Eq. (4.14),

$$\boldsymbol{\gamma}^{nm,\mathrm{PW}} = \mathbf{T}^{nm} = \begin{pmatrix} \boldsymbol{\gamma}_{\mathrm{oo}}^{nm,\mathrm{QR}} & \mathbf{0} \\ \mathbf{0} & \boldsymbol{\gamma}_{\mathrm{vv}}^{nm,\mathrm{QR}} \end{pmatrix}, \qquad (4.17)$$

where $\boldsymbol{\gamma}_{\mathrm{oo}}^{nm,\mathrm{QR}}$ and $\boldsymbol{\gamma}_{\mathrm{vv}}^{nm,\mathrm{QR}}$ are the occupied-occupied and virtual-virtual blocks of $\boldsymbol{\gamma}^{nm,\mathrm{QR}}$, and $\mathbf{T}^{nm}$ is referred to as the unrelaxed 1TDM.

Regardless of the choice of 1TDM in Eq. (4.14), an expression for the state-to-state derivative couplings including all Pulay terms is obtained by stationarizing the Lagrangian

$$L_{nm}[\mathbf{C}, \boldsymbol{\epsilon}, \mathbf{D}^{nm}, \bar{\mathbf{W}}^{nm}] = G_{nm}(\mathbf{C}, \boldsymbol{\epsilon}|\boldsymbol{\gamma}^{nm}, \mathbf{R}) + \langle \mathbf{D}^{nm,T}(\mathbf{C}^{\dagger}\mathbf{F}\mathbf{C} - \boldsymbol{\epsilon})\rangle - \langle \bar{\mathbf{W}}^{nm,T}(\mathbf{C}^{\dagger}\mathbf{S}\mathbf{C} - \mathbf{I})\rangle \quad (4.18)$$

where $\boldsymbol{\epsilon}$ is a Lagrange multiplier assumed to be block-diagonal, $\mathbf{F}$ is the (density-matrix dependent) Fock matrix in atomic orbital (AO) representation, $\mathbf{D}^{nm}$ and $\bar{\mathbf{W}}^{nm}$ are Lagrange multipliers that require the molecular orbitals to satisfy the KS equation and enforce orthonormality, respectively, and $\langle \cdot \rangle$ indicates a trace. $\mathbf{D}^{nm}$ and $\bar{\mathbf{W}}^{nm}$ are determined by enforcing stationarity with respect to the remaining parameters,

$$\left(\frac{\partial L_{nm}}{\partial \boldsymbol{\epsilon}}\right) = 0, \quad (4.19)$$

and

$$\left(\frac{\partial L_{nm}}{\partial \mathbf{C}}\right) = \left(\frac{\partial L_{nm}}{\partial \mathbf{C}^{\dagger}}\right) = 0. \quad (4.20)$$

Real orbitals are assumed only *after* taking derivatives such that fully general expressions are obtained. An outline of the derivation is provided in the appendix. At the stationary point, the total derivative of G_{nm} is obtained straightforwardly through a partial derivative of the Lagrangian,

$$\begin{aligned}
\frac{\mathrm{d}G_{nm}}{\mathrm{d}\xi} &= \frac{\partial L_{nm}}{\partial \xi} \equiv L_{nm}^{(\xi)} \\
&= \langle \mathbf{D}^{nm,\mathrm{AO},T}\mathbf{h}^{(\xi)}\rangle + \langle \mathbf{D}^{nm,\mathrm{AO},T}\mathbf{v}^{\mathrm{xc}(\xi)}\rangle \\
&\quad - \langle \bar{\mathbf{W}}^{nm,\mathrm{AO},T}\mathbf{S}^{(\xi)}\rangle + \langle \boldsymbol{\gamma}^{nm,\mathrm{AO},T}\mathbf{O}^{(\xi)}\rangle \\
&\quad + \langle \boldsymbol{\Gamma}^{nm,\mathrm{AO},T}\mathbf{V}^{(\xi)}\rangle + \langle \boldsymbol{\Gamma}^{nm,\mathrm{AO},T}\mathbf{f}^{\mathrm{xc}(\xi)}\rangle \quad (4.21) \\
&= \langle \mathbf{D}^{nm,\mathrm{AO},T}\mathbf{h}^{(\xi)}\rangle + \langle \mathbf{D}^{nm,\mathrm{AO},T}\mathbf{v}^{\mathrm{xc}(\xi)}\rangle - \langle \mathbf{W}^{nm,\mathrm{AO},T}\mathbf{S}^{(\xi)}\rangle \\
&\quad + \langle \boldsymbol{\Gamma}^{nm,\mathrm{AO},T}\mathbf{V}^{(\xi)}\rangle + \langle \boldsymbol{\Gamma}^{nm,\mathrm{AO},T}\mathbf{f}^{\mathrm{xc}(\xi)}\rangle \quad (4.22)
\end{aligned}$$

where Γ^{nm} is the pair transition density and all other quantities are defined as in Eq. (4.13). Eq. (4.22) follows from Eq. (4.21) by introducing $S_{\mu\nu}^{(-\xi)} = \langle \chi_\mu^{(\xi)}|\chi_\nu\rangle - \langle \chi_\mu|\chi_\nu^{(\xi)}\rangle$, then recognizing that $\mathbf{O}^{(\xi)} = \frac{1}{2}\left(\mathbf{S}^{(\xi)} + \mathbf{S}^{(-\xi)}\right)$ such that the Hermitian part of $\boldsymbol{\gamma}^{nm}$ can be combined with $\bar{\mathbf{W}}^{nm}$,

$$\mathbf{W}^{nm} = \bar{\mathbf{W}}^{nm} - \frac{1}{4}\left(\boldsymbol{\gamma}^{nm} + \boldsymbol{\gamma}^{nm,\dagger}\right). \tag{4.23}$$

The contractions involving $\mathbf{S}^{(-\xi)}$ with the anti-Hermitian part of $\boldsymbol{\gamma}^{nm}$ can be neglected on physical grounds.[172]

4.3.4   State-to-state derivative coupling implementation

Eq. (4.22) was implemented into the program `egrad`,[17] building on the existing implementation of excited-state gradients and ground-to-excited-state derivative couplings. The rate-determining steps are the computation of a user-specified set of excitations, Eq. (4.7), the construction of the relaxed densities, Eq. (4.16), and the final contraction of the effective densities with operator partial derivatives, Eq. (4.22). First, a user-specified set of excited states are computed, then couplings are computed between all excitations in a user-specified subset of the original excitations. For each pair of excited states, one coupled-perturbed Kohn–Sham (CPKS) calculation is required (for derivative couplings within full quadratic response theory, this becomes a dynamic polarizability calculation). The right-hand-sides for all pairs of excited states in Eq. (4.16) are computed simultaneously, together with the right-hand-sides for excited-state gradients,[17] using identical methodology as excited-state absorption calculations.[149] Thus the state-to-state derivative coupling implementation achieves the same high resource-efficiency as shown for other quadratic response properties,[149] up to the final contraction with operator derivatives. The required CPKS calculations were performed iteratively and simultaneously as described in Refs. 174 and 149 with an integral driven[175,59,176–178] nonorthonormal Krylov space block Davidson algorithm.[179] Finally, for each operator type (e.g., $\mathbf{h}$), contractions between its partial derivatives ($\mathbf{h}^{(\xi)}$) and all effective densities—including effective densities needed to compute ground- and excited-state gradients—were performed together such that the partial derivatives only need to be computed once.

Our implementation permits the computation of derivative couplings between excited-states computed with spin-restricted Kohn–Sham (RKS) or spin-unrestricted KS (UKS) orbitals, with or without the resolution-of-the-identity approximation for the Coulomb integrals,[60] with and without applying the Tamm–Dancoff approximation,[180] and for non-hybrid and hybrid semilocal density functionals, or time-dependent Hartree–Fock. Transition densities and RHSs between excited states were verified by reconstructing the dynamic hyperpolarizability from the exact TDDFT sum-over-states expressions. The final derivative couplings were verified against finite difference results.[147]

4.4 Excited-State Deactivation of Thymine

4.4.1 Prior results

Experimentally, three decay channels of UV-photoexcited thymine have been distinguished on the basis of gas phase femtosecond pump-probe transient ionization spectroscopy,[150,151,153–156] femtosecond time-resolved photoelectron spectroscopy (TRPES),[152] and Ultrafast X-ray Auger,[157] see Table 4.1: i) a *prompt* signal with a time constant near 100–200 fs ii) a *fast* signal with time constant of 5.1–7.0 ps and iii) a *slow* decay conventionally attributed to intersystem crossing that is longer than 100 ps. Although mechanistic details could be inferred for aqueous thymine photodynamics using UV resonance Raman spectroscopy,[181,182] the decay mechanism of UV-photoexcited thymine in the gas phase is experimentally difficult to probe.

The photodynamics of nucleic acids and nucleobases have been studied extensively computationally[166] using a range of different approaches, including characterization of the minimum energy pathways through conical intersections[159,160,183,155,184] and direct dynamics simulations.[161,156,162–165] Here, we focus on on-the-fly dynamical simulations of photoexcited thymine and refer the interested reader to a several extensive reviews for additional details.[158,166] Previously reported on-the-fly simulations of thymine photodynamics can be broadly categorized according to the electronic structure methods used to power the dynamics, see Table 4.2. To date, the most advanced on-the-

Table 4.1: Summary of experimental time constants for ultrafast deactivation of UV-photoexcited thymine[150,151,153–155,152] obtained with experimental techniques pump-probe transient ionization (PPTI), pump-probe resonant ionization (PPRI), pump-probe ionization spectroscopy (PPIS), and time-resolved photoelectron spectroscopy (TRPES)

Measurement	Component			
	ultrashort	prompt	fast	slow
PPTI[150]			6.4 ps	> 100 ns
TRPES[152]	< 50 fs	490 fs	6.4 ps	
PPRI[151]		105 fs	5.12 ps	
PPIS[153,154]		130 fs	6.5 ps	
PPIS[155]		100 fs	7.0 ps	>1 ns
X-ray Auger[157]		200 fs		

fly NAMD simulations have used semiempirical models,[185] MCSCF[156,162–164], and ADC(2) theory, with partially conflicting conclusions.

In particular, there appears to be no general consensus on the deactivation mechanism for photoexcited thymine with an excitation wavelength of 266 nm, near absorption onset. **Semiempirical models** such as multireference configuration interaction with the OM2 Hamiltonian[185] (OM2/MRCI)—which are parametrized to reproduce energies near ground state geometries and can thus become unreliable far from the Franck–Condon region such as near conical intersections—predict an overall excited-state lifetime of 437 fs, about one order of magnitude faster than that observed experimentally.[161] Furthermore, the predicted S_2 lifetime of 17 fs and S_1 lifetime of 420 fs lead to the interpretation that the ultrashort signal corresponds to internal conversion $S_2 \longrightarrow S_1$, the prompt signal corresponds to internal conversion to the ground state ($S_1 \longrightarrow S_0$) and the fast component corresponds to thermalization on the ground state.[161]

MCSCF, especially the state-averaged complete active space self-consistent field (SA-CASSCF) variant, is commonly used for NAMD simulations because, as a multireference method, it correctly recovers the topology of potential energy surface crossings.[186] However, CASSCF lacks dynamical correlation and can therefore overestimate the absorption onset and the S_2-S_1 energy gap by up to 1.5 eV in thymine relative to more accurate methods.[164] Thymine's photochemistry has been simulated using CASSCF by several different groups[156,162–164] with a qualitatively consistent picture emerging in which photoexcited thymine relaxes from the Franck–Condon (FC) geometry

to a minimum on the S_2 potential energy surface with a time constant of 100–200 fs thus giving rise to the prompt signal. The S_2 state then decays to the S_1 state with an estimated time constant of 2.6–5 ps and S_1 also exhibits a lifetime of several ps although precise estimates have not been provided. From this, the fast signal is assigned to the compound $S_{2,\text{min}} \longrightarrow S_1 \longrightarrow S_0$ deactivation. The relatively long S_2 lifetime has been attributed to a small but significant energetic barrier of ≈ 0.25 eV (5.7 kcal/mol) between the S_2 minimum and the S_2/S_1 conical intersection.[183] However, this trapping on the S_2 state surface was called into question based on ultrafast X-ray Auger experiments that observe a distinct electronic relaxation within 200 fs.[157] Furthermore, the barrier all but disappears with the inclusion of dynamic correlation. For example, the barrier falls to 0.05 meV (1 kcal/mol) using multistate complete active-space second-order perturbation theory (MS-CASPT2).[183]

To test the effect of dynamic correlation on the ensuing dynamics, Stojanović *et al.*[165] used the **ADC(2)** method. ADC(2) is complementary to CASSCF in that dynamic correlation is explicitly included to second-order, but being a single-reference method, ADC(2) is sensitive to strong static correlation due to near-degeneracy of the ground state. In particular, although *state-to-state* conical intersections are correctly reproduced, *ground-to-excited-state* intersections have the wrong dimensionality.[187] However, this may not be a cause for concern; preliminary investigations have shown that mixed quantum-classical trajectories are relatively insensitive to the dimensionality of the surface crossing, producing qualitatively similar results for different excited-state surface topologies.[188] As opposed to the several picosecond S_2 lifetime found with CASSCF dynamics, ADC(2) based dynamics indicate that following relaxation to the S_2 minimum in 100 fs, the majority of trajectories (84%) decay to S_1 within 250 fs. Out of these trajectories, 83% (70% of total trajectories) decay to the ground state within 400 fs. This lead to the conclusion that the prompt signal corresponds to decay to S_2 with the fast signal corresponding to $S_1 \longrightarrow S_0$ deactivation, but the computed rate for the latter reaction is approximately one order of magnitude too fast.

Table 4.2: Summary of computed time constants for ultrafast deactivation of UV-photoexcited thymine with available confidence intervals shown in parentheses in comparison to experimental results (see Table 4.1 for details)

Method	Component			
	prompt	assignment	fast	assignment
Semiempirical[161]	420 fs	$S_1 \longrightarrow S_0$		$S_0 \longrightarrow S_{0,eq}$
CASSCF[156,162–164]	100–200 fs	$S_{2,FC} \longrightarrow S_{2,min}$	2.6–5 ps	$S_{2,min} \longrightarrow S_1$
ADC(2)[165]	250 fs	$S_2 \longrightarrow S_1$	420 fs	$S_1 \longrightarrow S_0$
PBE0/SVP (this work)	153 fs (147–162 fs)	$S_2 \longrightarrow S_1$	13.9 ps (10.4–21 ps)	$S_1 \longrightarrow S_0$
PBE0/SVPD (this work)	110 fs (82–128 fs)	$S_2 \longrightarrow S_1$	20.5 ps (11.6–49 ps)	$S_1 \longrightarrow S_0$
Exp.	100–200 fs		5–7 ps	

4.4.2 Computational details

Initial conditions were drawn randomly from a 9.5 ps ground state ab initio molecular dynamics (AIMD) simulation at 500 K after a 0.5 ps equilibration period. The molecular dynamics were propagated with the leapfrog Verlet algorithm with an 80 a.u. ($\approx$1.935 fs) time step. The TPSS density functional[189] with D3 dispersion corrections[190] and Becke–Johnson (BJ) damping parameters[191] and the def2-SVP basis set[192] was used to compute the ground state energy at each time step. For these AIMD simulations, the resolution-of-the-identity (RI) was used to approximate the two-electron Coulomb integrals,[60] m3 grids with quadrature weight derivatives were used for functional integrations, and self-consistent field (SCF) convergence thresholds were set to 10^{-7} E_h (`scfconv 7`).

NAMD simulations were initiated on the bright S_2 surface with initial electronic density matrix $\sigma_{nm} = \delta_{n,2}\delta_{m,2}$ and used the PBE0 density functional[63] with D3-BJ dispersion corrections[190,191] and either split valence (def2-SVP)[192] or property-optimized (def2-SVPD)[193] basis sets. Excited states were computed within the Tamm–Dancoff approximation (TDA).[180] Molecular dynamics were propagated with the leapfrog Verlet algorithm and a time step of 40 a.u. (0.9676 fs). For the NAMD simulations, size 4 grids with quadrature weight derivatives were used for functional integrations, SCF convergence thresholds were set to 10^{-9} E_h (`scfconv 9`), and excited states were converged to a residual norm of less than 10^{-7} (`rpaconv 7`). As for ADC(2), conical intersections between the ground state and an excited state have incorrect dimensionality with TDDFT.[186] To

45
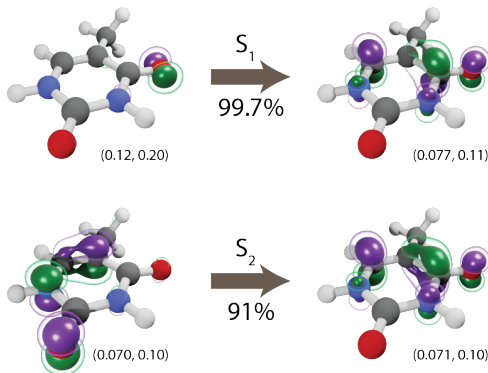
Figure 4.1: Dominant natural transition orbitals (NTOs) for the S_1 ($n-\pi^*$) and S_2 ($\pi-\pi^*$) electronic states. The corresponding singular value is shown under the arrow. For each NTO, isovalues are shown below the corresponding orbital and chosen to contain approximately 25% (inner) and 50% (outer) of the total orbital density. All excitations at the Franck–Condon geometry.

avoid potential associated instabilities, trajectories are forced to hop to the ground state if the first excitation energy, Ω_1, falls below 0.5 eV. In total, we simulated 200 independent trajectories for a combined 650 ps of simulation time.

All uncertainties indicated here correspond to 95% confidence intervals (CI) estimated from bootstrap sampling with 10000 samples.[194] Bootstrap sampling is a powerful resampling technique to estimate uncertainties in properties computed from a set of measurements of a stochastic process, i.e., without assuming an analytical distribution. Bootstrap sampling is therefore well-suited to estimating errors from NAMD trajectories where no information about the underlying statistical process is available.[195] To obtain the bootstrap confidence interval of, for example, the mean value of given set of N_{measure} measurements of a stochastic process, $N_{\mathrm{bootstrap}}$ replica samples are generated, the mean is computed for each replica sample, and confidence intervals are chosen to compactly contain the specified proportion of all replica means. Replica samples are generated by randomly selecting N_{measure} measurements with replacement (meaning duplicates are likely) out of the original N_{measure} measurements.

Table 4.3: Computed vertical excitation energies for the first two singlet excited states of thymine compared to experimental results from gas-phase electron energy loss (EEL) spectroscopy (band maxima)

Method	S_1 (eV)	S_2 (eV)
PBE0/SVP (this work)	4.85	5.44
PBE0/SVPD (this work)	4.83	5.24
ADC(2)[165]	4.56	5.06
MS-CASPT2[163]	5.09	5.09
MS-CASPT2[156]	5.23	5.44
CASSCF[163]	5.31	7.12
EEL spectroscopy		4.95[196], 4.9[197], 4.96[198]

4.4.3 Thymine excited states

The lowest-lying excited state (S_1) of thymine is a dark $n-\pi^*$ transition dominated by a single occupied-to-virtual transition, see Fig. 4.1, in which the dominant natural transition orbitals (NTOs) (singular value 0.997 with PBE0/def2-SVP) correspond to a HOMO-1 (highest occupied molecular orbital) to LUMO (lowest unoccupied molecular orbital) transition. The second excited-state (S_2), on the other hand, is a bright $\pi-\pi^*$ transition mostly characterized by a single HOMO-to-LUMO orbital transition (singular value 0.91). Using PBE0, we found little to no dependence of the S_1 vertical excitation energy on the basis set—4.85 eV with def2-SVP compared to 4.83 eV with def2-SVPD—and a small but notable dependence of the S_2 vertical excitation energy on the basis set—5.44 eV with def2-SVP compared to 5.24 eV with def2-SVPD. No further significant change was observed when moving to even larger basis sets: with def2-TZVPPD, the vertical excitation energies are 4.82 eV and 5.21 eV, respectively. For all of the basis sets considered here, the excitation energies computed using PBE0 at the ground state geometry agree well with excitation energies measured experimentally and computed by other methods, see Table 4.3.

4.4.4 Dynamics

All simulated trajectories exhibit similar qualitative behavior exemplified by the sample trajectory shown in Fig. 4.2: after being initiated on the S_2 state, thymine rapidly undergoes internal conver-
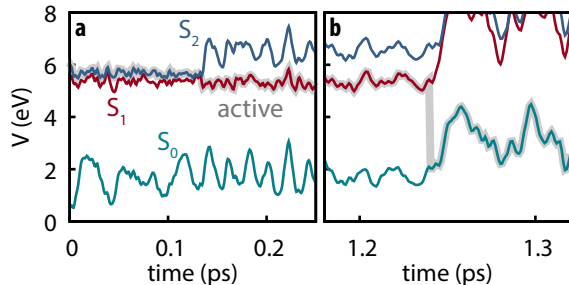
Figure 4.2: Example trajectory showing (a) the subpicosecond internal conversion from S_2 to S_1 followed by (b) slow decay to S_0.

sion to the S_1 state (in all cases occurring in less than 250 fs) followed by a slower decay to S_0 on the order of several ps.

Since the detailed nonadiabatic dynamics are expected to be highly sensitive to the energy difference between different excited states—which is itself sensitive to the basis set—we first assessed the difference between observed dynamics using both def2-SVP and def2-SVPD basis sets. 100 trajectories were simulated for each basis set using FSSH and trajectories were propagated for 5 ps using def2-SVP and 1.5 ps using def2-SVPD. Figure 4.3 compares the evolution of the excited state populations along these trajectories. Excited state populations in Fig. 4.3 were computed as $p_k(t) = N_k(t)/N_{\mathrm{traj}}$ where $N_k(t)$ is the number of trajectories with state k as active state at time t.

The S_2 decay with def2-SVPD was found to be significantly faster than with def2-SVP: with def2-SVP, the half-life of the S_2 state is 106 fs (CI: 102–112 fs) whereas the half-life with def2-SVPD was 76 fs (CI: 57–89 fs). The observed increased rate can be attributed to the reduced energy gap at the Franck–Condon geometry between S_1 and S_2, $\Delta E_{21} = E_{S_2} - E_{S_1}$, which is 0.59 eV at def2-SVP and 0.41 eV at def2-SVPD, i.e., the energy gap and the half-life both reduce by $\approx 70\%$. On the other hand, since ΔE_{10} is only slighty affected by the basis set, no significant change in the S_1 lifetime is expected or observed. After 1.5 ps, the proportion of trajectories on the ground state have strongly overlapping confidence interval ranges (6–18% with def2-SVP vs 3–12% with def2-SVPD). We therefore conclude that after the ultrafast decay to S_1, def2-SVP and def2-SVPD recover essentially identical dynamics and we thus continue our analysis with only the def2-SVP results.
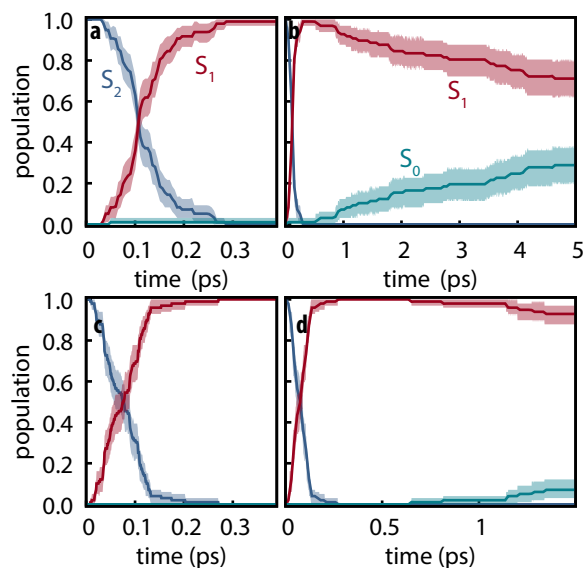
Figure 4.3: Excited-state populations measured over trajectory swarms using (a,b) def2-SVP and (c,d) def2-SVPD basis sets. Shaded regions show the 95% bootstrap confidence interval. Panels (a) and (c) show the short time behavior while panels (b) and (d) show the picosecond behavior. Note the different time scales in (b) and (d).
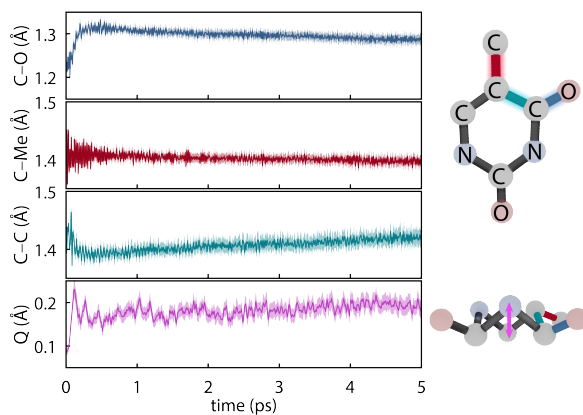
Figure 4.4: Major geometrical changes measured over trajectory swarms accompanying ultrafast dynamics simulated with def2-SVP and FSSH. Shaded regions show the 95% bootstrap confidence interval. a) $C-O$ bond distance b) $C-Me$ bond distance c) aromatic $C-C$ bond distance and d) the puckering amplitude, Q.[199]

The initial dynamics were quantified in terms of four structural parameters, the C−O bond distance of the carbonyl on which the S_1 hole is located, the C−Me (where Me is methyl), the C−C bond distance for the carbon atoms in the ring connecting the active carbonyl and the CMe, and the ring puckering amplitude, Q, computed using the Cremer–Pople coordinates.[199] Figure 4.4 summarizes the dynamics simulated using FSSH and depicts the coordinates involved. Immediately upon photoexcitation, the C−O bond lengthens and the C−C bond shortens, both of which are consistent with observed shifts in the oxygen Auger spectrum[157] and with the interpretation that the particle (virtual) NTO of the S_2 excitation exhibits a bonding-like π overlap on the C−C bond in the ring and an antibonding-like structure on the carbonyl. In addition, the puckering amplitude more than doubles from the equilibrium value of about 0.08 Å to 0.23 Å within 120 fs. However, we find no significant difference in the degree of planarity between the ground state and S_1, and thus attribute the increased degree of puckering to the increased vibrational energy resulting from the nonradiative decay.

The simulated rates for the two electronic decays ($S_2 \longrightarrow S_1$ and $S_1 \longrightarrow S_0$) are characterized as single exponential decays from which two lifetimes are defined according to

$$p_2(t > 0) \approx e^{-t/\tau_2}, \text{ and} \tag{4.24a}$$

$$p_0(t > 0) \approx 1 - e^{-t/\tau_0}, \tag{4.24b}$$

where τ_2 corresponds to the $S_2 \longrightarrow S_1$ decay channel and τ_0 corresponds to the rise of the ground state or conversely the total excited state lifetime. τ_2 is estimated through the S_2 half-life, $t_{S_2,1/2}$, according to

$$\tau_2 = t_{S_2,1/2}/\ln 2, \tag{4.25}$$

while τ_0 is similarly estimated from the final value in the simulation using

$$\tau_0 = -t_f/\ln(1 - p_{0,f}), \tag{4.26}$$
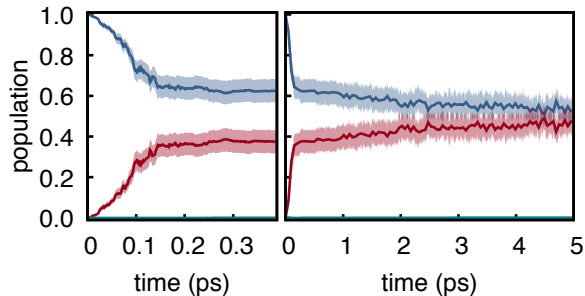
Figure 4.5: Electronic populations computed from the auxiliary electronic density matrix for trajectories computed using PBE0-D3/def2-SVP and FSSH. Shaded regions show the 95% bootstrap confidence interval. (a) short time and (b) long time behavior.

where t_f and $p_{0,f} = p_0(t_f)$ are the time and population used to estimate the rate.

Using the set of def2-SVP simulations, we find the S_2 lifetime to be $\tau_2 = 153$ fs (CI: 147–162 fs) which agrees well with the 100–200 fs lifetimes measured for the prompt signal. Consequently, we assign the prompt signal to the $S_2 \longrightarrow S_1$ decay. The total excited state lifetime was found to be 13.9 ps (CI: 10.4–21 ps), which agrees well (within a factor of 2) with the 5–7 ps lifetimes measured for the fast component such that we assign the fast signal to correspond to the $S_1 \longrightarrow S_0$ decay.

4.4.5   Electronic populations and surface hopping

Electronic populations within FSSH and many of its variants are ambiguously defined[200] because the FSSH algorithm refers to two distinct effective electronic wavefunctions: i) the auxiliary wavefunction, which is propagated using Eq. (5.2) and ii) the active wavefunction which is determined from the evolution of the auxiliary wavefunction and from which the potential energy and nuclear forces are computed. The preceding analysis follows the original prescription[22] in which only the active wavefunction (i.e. the active surface) is used to determine electronic populations although other prescriptions have been proposed.[201] However, it is important to examine the auxiliary electronic populations because they indirectly dictate the behavior of the active wavefunction and because they are central to the original motivation for hopping probabilities.

Electronic populations using the auxiliary wavefunction indicate negligible nonradiative decay from

51

S_1; instead, the populations slowly evolve towards a near equal mixture of S_1 and S_2 (see Fig. 4.5). This leads to a starkly different interpretation of the reactivity—that S_1 and S_2 are equally populated on the picosecond timescale—that is not supported by any experimental evidence. This is concerning given that the FSSH hopping probability was derived to satisfy the constraint that the swarm-based populations, i.e., populations computed through

$$p_k(t) = \langle N_k \rangle(t)/N_{\text{traj}}, \tag{4.27}$$

where $\langle N_k \rangle(t)$ is the number of trajectories with active surface k at time t and N_{traj} is the total number of trajectories, statistically match the auxiliary populations.[22] It thus appears that physically valid results for thymine are obtained even though a central assumption underlying surface hopping is violated. These results imply that efforts to adjust the surface hopping criterion to better enforce the correspondence between swarm-based populations and the auxiliary electronic density matrix could adversely affect accuracy for the present system.[202]

Our observation is consistent with the fact that the total energy of a trajectory and all properties, including electronic populations, are best defined in terms of an energy derivative:[203]

$$\sigma_{nm}^{\text{effective}}(t) = \frac{\partial \langle E \rangle(t)}{\partial H_{mn}(t)}, \tag{4.28}$$

where $E(t)$ is the trajectory energy which is defined as the nuclear kinetic energy plus the electronic energy of the active state.

4.5   Conclusions

Building on resource-efficient methodology previously developed for ground states, excited states, and quadratic response properties, the implementation of state-to-state derivative couplings reported here enables multistate nonadiabatic molecular dynamics simulations using hybrid-TDDFT for molecules with up to $\sim$100 atoms and $\sim$10 ps simulation times on single workstation nodes. For

the first three singlet states of thymine, each step of an on-the-fly NAMD simulation including all couplings requires only a factor of 4.3 more CPU time than the corresponding ground-state AIMD simulation. As opposed to finite-difference approaches, the entire nonadiabatic coupling vector is obtained, enabling correct rescaling of velocities. The single Slater-determinant model for excited states corresponds to a zeroth-order noniterative approximation using unit excitation vectors and neglecting the Hartree, exchange, and correlation contributions to the excitation energy. Whether the resulting modest gain in efficiency is worthwhile in view of the loss of accuracy caused by neglect of configuration interaction appears questionable. Our implementation will be publicly released through Turbomole V7.5.[65,204] All NAMD trajectory data are available through a Creative Commons license.[205]

Straightforward application of the present hybrid TDDFT-SH methodology to UV-photoexcited thymine semiquantitatively recovers experimental excited-state lifetimes. In particular, the TDDFT-SH lifetimes of 147–162 fs for S_2 and 10.4–20.1 ps for S_1 agree well with the experimentally observed ones of 100–200 fs and 5–7 ps. The rapid S_2 decay is barrierless and proceeds through a conical intersection between S_2 and S_1 close to the Franck–Condon region, whereas the S_1 decay is much slower. Thus, our results strongly support the S_1 trapping hypothesis.[156]

For thymine deactivation, TDDFT using standard hybrid functionals yields significantly better agreement with experiment than MCSCF and ADC(2). While this result could be coincidental, it is consistent with the good performance of hybrid TDDFT for vertical excitation energies of thymine, as well as a mounting body of evidence suggesting that hybrid TDDFT has favorable cost-to-performance characteristics for a wide range of systems,[206,135,207,208,131,209,210,140,211,139,212,213,128]. Due to its resource efficiency, TDDFT-SH is particularly suitable for large-scale and exploratory applications. The striking discrepancy between electronic and trajectory-averaged populations for the slow decay of the S_1 state of thymine may warrant further investigation. The current approach circumvents but does not fundamentally eliminate the divergences of inexact response theory in state-to-state properties.[21,35]

Chapter 5

Fewest switches surface hopping and decoherence corrections, a study of thymine and isocytosine

5.1 Introduction

Nucleobases absorb in the ultraviolet region of the spectrum and are extremely efficient in dissipating the excitation energy through nonradiative internal conversions.[151,150,158] The naturally occurring pyrimidines in most organismic DNA; thymine, cytosine and uracil, undergo ultrafast internal conversion, and decay to the ground state in a few picoseconds (ps), with thymine being the longest lived pyrimidine. Experiments and quantum chemical calculations agree that the lowest lying bright state of thymine is the second excited state, S_2, and a $\pi \to \pi*$ character, with a lower dark $n \to \pi*$ S_1 state.[150–157] Time resolved spectroscopic experiments on thymine suggest there are two decay lifetimes. However, the assignment of the decay lifetimes to actual reaction mechanism pathways is unclear, with conflicting interpretation of the experimental and computational results.[150,158,166]

The dynamics for the internal conversion of the nucleobases necessarily involves exchange energy from the electronic excitation to the nuclear degrees of freedom, making the Born-Oppenheimer approximation inappropriate for the chemical description, and such processes are called 'nonadiabatic'.[16] NAMD[214,22] has emerged as a tool to study photochemical processes. Fewest switches surface hopping (FSSH)[22] is a popular choice for studying photochemistry, and has been used to study a variety of systems, from quantum dots[215,216] and perovskites[136] to small organic molecules.[140,217] Owing to the simplicity of the implementation and relatively direct interpretation of the dynamics, FSSH has been used to understand the internal conversion of the natural as well as synthetic nucleobases, including thymine. The results from using FSSH with complete CASSCF methods for modeling the electronic states do not agree with those from using the second order algebraic diagrammatic construction (ADC(2)) for electronic excitation. While the dynamics using CASSCF methods suggest an S_1 trap of thymine, results from ADC(2) calculation predict an ultrafast <350 fs decay to the ground state mediated via a semi-planar ring distortion conical intersection, neither of which fully justify the experimental decay lifetimes.

While CASSCF cannot describe dynamic correlation, which is often cited as the source of error in the corresponding dynamics, using ADC(2) requires numerical derivatives to approximate the nonadiabatic couplings between the electronic states,[218] the driving factor for transfer of populations between electronic states due to coupling with the nuclear momenta. Time-dependent density functional theory serves as an alternative method for calculating excited state energies, gradients and nonadiabatic coupling vectors.[120,170,17] While nonadiabatic coupling vectors between ground and excited states are available through linear response TDDFT,[18] recent development in quadratic response TDDFT allows the computation of nonadiabatic coupling vectors between two excited states.[219,220,149] Recently, Parker and coworkers studied the multistate dynamics of thymine using hybrid TDDFT and FSSH, and found good agreement between the simulated and experimental lifetimes.[221] The study, however, showed inconsistency in the electronic and nuclear populations of thymine, a known artifact of the FSSH method.[222,223] In addition, this study did not include any decoherence corrections to FSSH to account for the well studied shortcoming of overly coherent electronic density matrices in FSSH.[23-33] Upon divergence of the nuclear populations, the reduced

electronic density matrix should have little coherence. However, it has been observed that FSSH provides unreliable results in systems where the nuclei pass through multiple regions of strong electronic coupling.[28] Lastly, despite the agreement of experimental and simulated lifetimes, the study did not reveal any distinct chemical pathway for the $S_1 \rightarrow S_0$ decay. In the present work, we reinvestigate the thymine dynamics within TDDFT and address the inconsistency in the FSSH populations.

Along with the study of regular nucleobases, the study of nonadiabatic dynamics of isocytosine has gained traction in the recent years.[224–226] Isocytosine forms base pairs with isoguanine and is of considerable interest in the field of synthetic genetic coding. Interestingly, all the NAMD simulations for isocytosine was performed using an energy based decoherence corrected FSSH algorithm. Unlike thymine, the semiclassical dynamics of isocytosine using CASSCF and ADC(2) broadly agrees on the mechanisms of nonadiabatic decay. The results differ in the quantitative estimation of the excited state lifetime of isocytosine, and the importance of each pathway. The overall decay of isocytosine using ADC(2) is $\sim$ 350 fs, where as CASSCF dynamics predicts an overall lifetime of $\sim$ 1 ps. Due to the lack of experimental studies on the excited state lifetimes of isocytosine, results from NAMD using TDDFT is expected to provide new insights into the decay mechanism of isocytosine. In addition, direct comparison of the effect of decoherence correction to the FSSH algorithm can be studied for isocytosine.

The chapter is organized as follows. In section 5.2, we briefly introduce two popular decoherence corrections to FSSH. The computational details to study thymine and isocytosine are presented in section 5.3. Section 5.4 contains the important results from thymine and isocytosine dynamics using various flavors of decoherence correction, and a future outlook for the nonadiabatic dynamics for nucleobases is discussed in section 5.5.

5.2 Fewest switches surface hopping and decoherence corrections

5.2.1 FSSH

FSSH attempts to reproduce the effects of electronic population transfer through an ensemble of classical nuclei hopping between electronic potential energy surfaces. At any given time, the nuclei are affected by the force from only one of the electronic surfaces (say, the active surface). The method is designed such that the distribution of the active surface in the ensemble mimic the electronic population. Due to the predictive nature of the FSSH simulations, reaction pathways are possible to be discovered in-silico, such as TiO_2 water splitting mechanism,[139] decay mechanisms of $CH_2NH_2^+$,[227] deactivation pathways of nucleobases[187,228] and photobases.[229]

FSSH uses an ensemble of trajectories each consisting of classical nuclei and an auxiliary reduced electronic density matrix. One of the electronic states is identified as the active state and the forces on the nuclei are computed from the energy gradients of that electronic state. The auxiliary electronic density matrix, $\hat{\sigma}^{\mathrm{aux}}$, can be expanded in the outer product space of the eigenstates of the Born-Oppenheimer electronic Hamiltonian, $\mathbf{H}(\mathbf{R})$:[22].

$$\hat{\sigma}^{\mathrm{aux}} = \sum_{nm} \sigma^{\mathrm{aux}}(t)_{nm} |\phi_n; \mathbf{R}(t)\rangle\langle\phi_m; \mathbf{R}(t)| \tag{5.1}$$

where $|\phi_n\rangle$ is the nth eigenstate of $\mathbf{H}(\mathbf{R})$ with electronic energy of E_n, $\mathbf{R}(t)$ is the nuclear coordinate vector and $\sigma(t)$ are the expansion coefficients, which are the dynamical variable for the propagation of the auxiliary electronic density matrix.

When the electronic Schrödinger equation is expanded in the adiabatic basis, the auxiliary density matrix follows the equation of motion:

$$\dot{\sigma}^{\mathrm{aux}}(t) = -i[\hat{\bar{H}}(\mathbf{R}), \sigma^{\mathrm{aux}}(t)] \tag{5.2}$$

where

$$\hat{\bar{H}} = \hat{\mathbf{H}} - i\hat{\mathbf{W}} \tag{5.3}$$

acts as the effective Hamiltonian, $\hat{\mathbf{W}}(\mathbf{R})$ is the nonadiabatic coupling term computed as $W_{ij}(\mathbf{R}(t)) = \dot{\mathbf{R}} \cdot \langle \phi_i; \mathbf{R}(t) | \frac{\partial}{\partial \mathbf{R}} | \phi_j; \mathbf{R}(t) \rangle$. The term $\langle \phi_i; \mathbf{R}(t) | \frac{\partial}{\partial \mathbf{R}} | \phi_j; \mathbf{R}(t) \rangle$ is the so-called nonadiabatic coupling vector, $\tau_{ij}(\mathbf{R})$.

The nuclear coordinates follow the classical equations of motion:

$$\dot{\mathbf{P}} = -\nabla_{\mathbf{R}} \langle \phi_{\text{active}} | \hat{\mathbf{H}}(\mathbf{R}) | \phi_{\text{active}} \rangle \tag{5.4}$$

where $\mathbf{P} = \mathbf{M}\dot{\mathbf{R}}$, $\mathbf{M}$ being a diagonal matrix containing the nuclear mass corresponding to each degree of freedom. In each time step Δt of the simulation, each trajectory gets a chance to change its identity of active state through a stochastic 'hop'. The probability of a hop from a state k to a state m is given by g_{km} and is defined as:

$$g_{km} = \int_t^{t+\Delta t} dt' \frac{\text{Re}\{\sigma_{km}^{\text{aux}}(t')\bar{\mathbf{H}}_{mk} - \bar{\mathbf{H}}_{km}\sigma_{mk}^{\text{aux}}(t')\}}{\sigma_{kk}^{\text{aux}}}. \tag{5.5}$$

A random number η is generated from the uniform distribution U(0,1) and compared to the probability of hopping from the active state to every other state considered in the system. If $g_{\text{active},m} < \eta$, then a hop is initiated from the active state to state m, which becomes the new active state. Upon hopping, to conserve total energy, the nuclear classical momentum is rescaled, however, only along the direction of the nonadiabatic coupling vector between the two states. In case of a hop from a state of lower electronic energy to a state of higher electronic energy, it is possible to have insufficient kinetic energy along the direction of the nonadiabatic coupling vector between the two states involved, resulting in a so-called 'frustrated hop'. The implications of a frustrated hop are unclear, and several suggestions exists on what to be done in such event.[230–232,25] In our simulations we have chosen to ignore the frustrated hops and proceed without hopping.

5.2.2 Energy based decoherence correction as suggested by Granucci and Persico

One of the earliest solutions to the problem of overcoherent auxiliary electronic density matrices was suggested by Truhlar and coworkers through their decay of mixing methods.[24] The method was simplified by Granucci and Persico,[26] making it more suitable to be incorporated within an existing FSSH implementation. The method uses an adjustable parameter in the units of energy in calculating the rate of decoherence. The decoherence corrected FSSH, as suggested by Granucci and Persico (GP), was shown to correctly describe the decay of diazobenzene, is gaining popularity in the literature. The method has been used in diverse applications with reasonable success in explaining nonadiabatic phenomena.[233–235]

In the energy based decoherence correction to the FSSH, a rate of decoherence τ_{km} is computed at each step:

$$\tau_{km} = \frac{1}{|E_k - E_m|}\left(1 + \frac{C_{gp}}{E_{\text{kin}}}\right) \tag{5.6}$$

where E_{kin} is the total nuclear kinetic energy, and E_k is the electronic energy of the kth adiabatic state. The parameter C_{gp} is set to 0.1 Hartree according to the suggested by Jasper and coworkers.[236]

Using this rate of decoherence, after each time step, the density matrix is modified after propagating it using eq. 5.2. The 'decoherence correction' to the density matrix is introduced as

$$\sigma_{ij}^{\text{aux}}(t') = \sigma_{ij}^{\text{aux}}(t)e^{-\Delta t\left[\frac{1}{\tau_{i,\text{active}}} + \frac{1}{\tau_{j,\text{active}}}\right]}. \tag{5.7}$$

5.2.3 Augmented fewest switches surface hopping

As an alternative to parameter-based decoherence corrections, a parameter-free correction for decoherence in FSSH is the augmented FSSH (A-FSSH) developed by Subotnik and coworkers.[27,28]

Instead of an energy based cut-off, the method propagates the moments of quantum nuclear position and momentum on each surface, and motivates for a parameter-free rate of decoherence. The idea is to check for diverging position and momentum on different adiabatic surfaces and construct a stable rate of decoherence. The rate of decoherence is estimated assuming Gaussian nuclear wavepackets in position and momentum representation and invoking the minimal uncertainty principle between them. Using the rate of decoherence, a probability of collapse of the electronic density matrix is estimated and the auxiliary density matrix of each trajectory of the ensemble is stochastically collapsed based on this probability.

The exact algorithm for A-FSSH has evolved over the years, and the same name, A-FSSH, has been used to describe several algorithms. While the original method had only a rate of collapse for the auxiliary density matrices,[27] the subsequent algorithms with the same name added a rate of reset for the moments,[237] as the authors argued that upon long simulations, the Gaussian approximated moments lose meaning, and must be discarded. A simplified algorithm, using the diagonal approximation for the moments, has also been suggested by Jain *et al.*[33] The motivation for the diagonal approximation was computational cost, which in our simulations is dominated by the ab-initio calculations of the electronic properties.

In A-FSSH, the position and momentum distributions are assumed to be Gaussians. Additional dynamical quantities, $\delta \mathbf{R}$ and $\delta \mathbf{P}$ are propagated, denoting the second moments of quantum position and momentum operators for the nuclei respectively. The equations of motion for these dynamical variables up to first order are:

$$\dot{\delta \mathbf{R}} = -i[\hat{\mathbf{H}}(\mathbf{R}), \delta \mathbf{R}] + \delta \mathbf{P} \mathbf{M}^{-1} - [\hat{\mathbf{W}}, \delta \mathbf{R}] \tag{5.8}$$

and

$$\dot{\delta \mathbf{P}} = -i[\hat{\mathbf{H}}(\mathbf{R}), \delta \mathbf{P}] + \frac{1}{2}\{\delta \mathbf{F}, \sigma^{\mathrm{aux}}\} - [\hat{\mathbf{W}}, \delta \mathbf{P}] \tag{5.9}$$

where $\delta \mathbf{F} = \mathbf{F} - \mathbf{F}_{\mathrm{active,active}}$, $\mathbf{F}_{ij} = \langle \phi_i; \mathbf{R}(t) | \frac{\hat{\mathbf{H}}(\mathbf{R})}{\partial \mathbf{R}} | \phi_j; \mathbf{R}(t) \rangle$ and $\{\cdot, \cdot\}$ denotes an anticommutator.

In A-FSSH, the decoherence correction is introduced through collapses of the auxiliary density matrix σ^{aux}. These collapses are determined by sampling a random number between zero and one, and comparing it to a probability of collapse. The probability of collapse of state i is given by

$$p_i^{\mathrm{collapse}} = \Delta t \times \left(\frac{1}{2} \left(\delta \mathbf{F}_{ii} \cdot (\delta \mathbf{R}_{ii} - \delta \mathbf{R}_{\mathrm{active,active}}) \right) - 2 | \mathbf{F}_{i,\mathrm{active}} \cdot (\delta \mathbf{R}_{ii} - \delta \mathbf{R}_{\mathrm{active,active}}) | \right). \quad (5.10)$$

The probability of collapse is proportional to the difference in the second moments of the position operator. The authors argue that, if in a trajectory, the moments on any surface become too large, it indicates that the nuclear population on that surface is not represented by that trajectory in the ensemble, and hence its quantum amplitudes should be collapsed.

Subotnik and coworkers further argued that the moments lose significance over long simulation time, and suggested a rate of resetting the moments to zero. The probability of resetting the moments at each step is:

$$p_i^{\mathrm{reset}} = \Delta t \times \left(-\frac{1}{2} \left(\delta \mathbf{F}_{ii} \cdot (\delta \mathbf{R}_{ii} - \delta \mathbf{R}_{\mathrm{active,active}}) \right) \right). \quad (5.11)$$

At each step, a new random number is drawn from the U(0,1) distribution and compared to p_i^{collapse} and p_i^{reset} $\forall i$. If the random number is greater than any of the two probabilities, then the moments are reset to zero. In case of the random number being larger than p_i^{collapse}, the $\sigma_{ij}^{\mathrm{aux}}$ and $\sigma_{ji}^{\mathrm{aux}}$ are set to zero for all states, and the population of state i is added to $\sigma_{\mathrm{active,active}}^{\mathrm{aux}}$. In case of a hop, the moments are also reset to zero. The various conditions and consequences of the dynamical variables are listed in equation 5.12.

$$\text{Set } \delta \mathbf{R} = \delta \mathbf{P} = \mathbf{0} \begin{cases} \text{if} \eta > p_i^{\mathrm{collapse}}, & \text{Set } \sigma_{\mathrm{active,active}}^{\mathrm{aux}} = 0 \\ \text{if} \eta > p_i^{\mathrm{reset}}, \\ \text{if Surface hop} \end{cases} \quad (5.12)$$

61

Implementation and performance of FSSH into the program `frog`[238] has been reported in Refs. 20 and 221. We implemented the methods GP and A-FSSH using the existing implementation of FSSH in `frog`. Implementation of eq. (5.7) did not require additional propagation of any further dynamical variables. For the implementation of A-FSSH, we used a fourth-order Runge-Kutta scheme to integrate eqs. (5.8) and (5.9) with a smaller timestep than the classical propagation, $\Delta t' = \Delta t / f$. The smallest value for the f was 10, and it was set to the closest integer of $\frac{E_{max} - E_0}{0.01 Hartree}$ for each time step, which was usually larger, to achieve higher accuracy.

5.3   Computational details

For the NAMD, all ground and excited state energies and gradients were obtained from DFT and TDDFT calculations using the hybrid functional PBE0.[63] Fine integration grid m4[59] with weight derivatives were used for the numerical integration of the density. The resolution-of-identity (RI-J) approximation[60] was used throughout and Grimme's D3-BJ[190,191] correction was used to account for the dispersion interaction. The self-consistent field calculations were converged to a threshold of 10^{-8} Hartrees. The Franck–Condon geometry of the molecule was obtained by optimizing the geometry using the def2-SVP basis functions[192] with a threshold of 10^{-4} au in gradients. Excitation energies were obtained at the Franck–Condon geometry within the full TDDFT formalism, and the dynamics was simulated within the Tamm-Damcoff approximation (TDA)[180] of TDDFT using the def2-SVP basis set.[192] Initial distribution of position and momentum was obtained from an ab initio molecular dynamics (AIMD) simulation using DFT at 500 K for 1.5 ps. The coordinates were propagated using a time step of 20 a.u. (= 0.4838 fs) and the leap frog velocity-Verlet algorithm.

The initial positions and momenta of the nuclei for the NAMD simulations were sampled from the last 1 ps of the ground state (AIMD) trajectory. 50 trajectories for each method (FSSH, GP and A-FSSH) were initiated by populating the S_2 state and setting the active state to the bright state of each molecule. The molecular dynamics was performed using a time step of 40 a.u. (= 0.9676 fs) up to 1 ps. The trajectories were forced to hop to the ground state when the lowest excitation

energy was lower than 0.2 eV to avoid instabilities. Bootstrapping sampling with 10,000 samples was used to measure the uncertainty in the ensemble averages.[194] We use a 95% confidence interval to estimate the lower and upper bound of the ensemble averages. With a total simulation time of 150 ps, we can extract statistically significant results at a cost of 0.6 kWh per method per timestep.

We measured the lifetimes of $S_2 \rightarrow S_1$ (τ_2) and $S_1 \rightarrow S_0$ (τ_0) decay by characterizing them as single exponential decays:

$$p_2(t) \approx e^{-t/\tau_2} \tag{5.13}$$

and

$$(1 - p_0(t)) \approx e^{-t/\tau_0}. \tag{5.14}$$

In case of an exponential decay, S_2 lifetime can be estimated using the half-life time of the population $0.5 = p_2(t_{S_2,1/2})$ and τ_2 is related to $t_{S_2,1/2}$ by

$$\tau_2 = t_{S_2,1/2}/\ln(2) \tag{5.15}$$

However, for the case of FSSH, the S_2 electronic population does not necessarily decay exponentially below 0.5. In such cases, we estimate τ_2 as:

$$\tau_2 = t_{S_2,1/4}/\ln(4) \tag{5.16}$$

where $p_2(t_{S_2,1/4}) = 0.75$. The lifetime of internal conversion is easier to compute as $\tau_0 = -t_f/\ln(1 - p_{0f})$ where $p_{0f} = p_0(t_f)$ is the final population of the ground state at the end of the simulation at time t_f.

For the analysis of the potential energy surfaces, single point calculations for excitation energies

of thymine and isocytosine are performed using approximate coupled cluster singles and doubles (CC2)[239] along with other density functionals: TPSS,[54] TPSSh[240] and PBE .[241] All calculations were carried out using a developer version from Turbomole-7.4.[65]

5.4   Results

5.4.1   Thymine

The results obtained from FSSH without decoherence correction are presented in chapter 4. Using the decoherence corrections, we find an improved consistency between the electronic and swarm populations in the decay of S_2 to S_1. While there was no qualitative difference in S_2 to S_1 lifetime with decoherence corrections, slight dilation occurred from 154 fs to 173 fs (A-FSSH) and 200 fs (GP) respectively. The mechanism of decay from S_2 to S_1 is through a ring puckering distortion conical intersection (see Figure 5.1) which is of similar geometry to that optimized using CASSCF as reported in Ref. 242. The distortion is similar to a boat structure of six-membered rings. The lifetimes calculated using the electronic and the swarm populations are listed in Table 5.1.
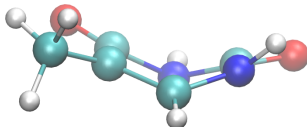
Figure 5.1:   Structure of thymine at an S_2-S_1 conical experienced in the course of its dynamics.

Using the data presented in Ref. 221 we find substantial disagreement in the calculated lifetimes using the swarm (14 fs) and electronic (3696 fs) populations for S_1 to S_0 decay, with the lifetimes calculated from the swarm populations being consistent with experiment. Hops from the S_1 to S_0 state within TDDFT occurred in configurations where the calculated gap was around 1.5 eV. Following the hops to the S_0 state, the trajectories encountered a significant number of frustrated hops. With the addition of decoherence corrections, no decay from the S_1 to the S_0 is observed

Table 5.1: Lifetimes of $S_2 \rightarrow S_1$ and $S_1 \rightarrow S_0$ decays for thymine using the three methods. The window of 95% confidence interval is mentioned in parenthesis.

	FSSH		A-FSSH	GP
$S_2 \rightarrow S_1$ decay times in fs				
Electronic population	69	(66 - 91)	158 (155 - 173)	184 (165 - 208)
Swarm population	154	(148 - 166)	173 (161 - 195)	200 (181 - 216)
$S_1 \rightarrow S_0$ decay times in ps				
Electronic population	3696	(5089 - 2776)	X	X
Swarm population	14	(21 - 10)	X	X

Table 5.2: TDDFT and CC2 excitation energies at the ADC(2) conical intersection geometry.

Method	TD-PBE	TD-PBE0	TD-TPSS	TD-TPSSh	CC2
Basis set	SVPD	SVPD	SVPD	SVPD	SVP
Excitation (eV)	1.01446	1.57510	1.13547	1.35332	1.16067

within 2 ps of simulations. The estimated lifetime from the little electronic population transfer to the ground state in either decoherence corrections is in the order of 10 μs, which is not experimentally supported. In A-FSSH, the source of such small transfer of population to the ground state is the occasional collapse of the density matrix, which removes all electronic populations from the ground state. Addition of the decoherence correction also resulted in overall reduction of frustrated hops (see Figure 5.2). In contrast to ADC(2) based dynamics as reported in Ref. 165, the decoherence corrected and uncorrected FSSH dynamics based on TDDFT surfaces had no decay through a S_1/S_0 conical intersection. The ring distortion conical intersection which plays an important role in the dynamics of thymine on ADC(2) surfaces is, in fact, not reproduced when using TDDFT with different functionals or CC2 excitation (see Table 5.2). Of the four identified S_1–S_0 conical intersections from CASSCF calculations in Ref. 159, only one is reproduced using TDDFT. Linear interpolation of the the S_1 surface from the S_1 minima structure to that conical intersection shows a barrier of 1.30 eV (see Figure 5.3) explaining why that conical intersection is never accessed in the dynamics.
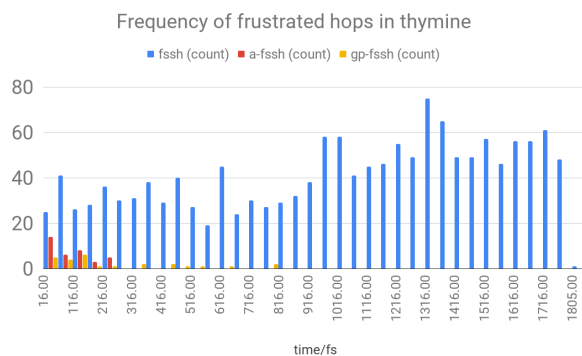
Figure 5.2: Frequency of frustrated hops for thymine using FSSH, A-FSSH and GP for the nonadiabatic dynamics.
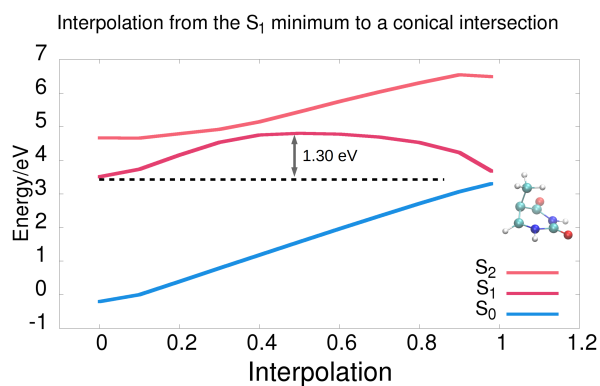
Figure 5.3: TD-PBE0 potential energy profiles for S_0, S_1 and S_2 surfaces using def2-SVPD basis interpolated from the S_1 minima to a conical intersection involving the out-of-plane bend of the methyl group is shown in the figure. The structure of thymine at the conical intersection is shown in the inset.

(a)

(b)
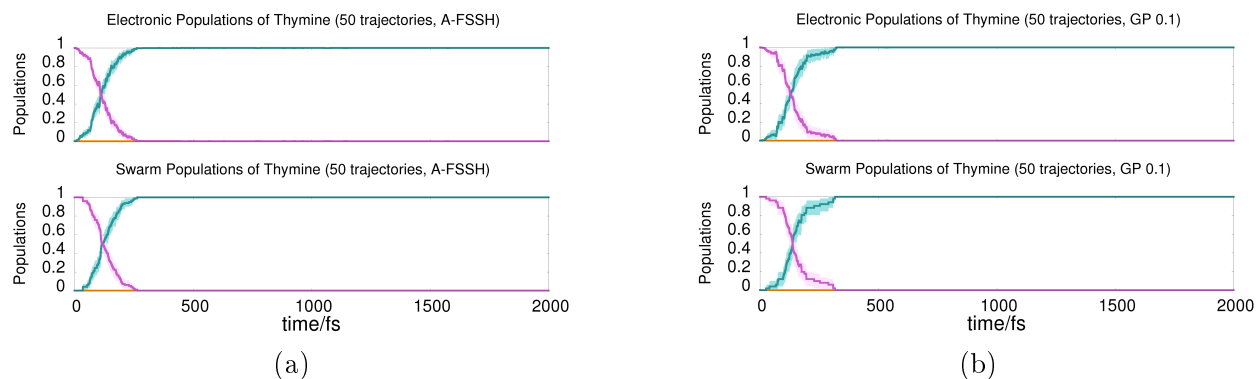
Figure 5.4: Electronic and swarm populations of S_2 (magenta), S_1 (cyan), S_0 (orange) of thymine using a) A-FSSH and b) GP. The same color shadings represent a bootstrap confidence interval of 95%.

66

Table 5.3: The lowest two singlet excitations of isocytosine at the Franck–Condon geometry from TD-PBE0 with TDA and full linear response using three basis sets.

| Excitation | S_1 | S_2 | S_1 | S_2 | S_1 | S_2 | S_1 | S_2 |
Basis	SVP	SVP	SVPD	SVPD	TZVP	TZVP	TZVPD	TZVPD
TDA								
Excitation energy (eV)	5.11	5.22	5.04	5.08	5.09	5.12	5.00	5.07
Oscillator strength	0.001	0.235	0.211	0.004	0.218	0.006	0.214	0.001
Full response								
Excitation energy (eV)	4.99	5.09	4.82	5.07	4.87	5.10	4.79	5.06
Oscillator strength	0.179	0.000	0.171	0.000	0.171	0.000	0.165	0.000

Table 5.4: Lowest two excitation energies in eV of isocytosine.

Method	Basis	$\pi \rightarrow \pi*$	$n_O \rightarrow \pi^*$
ADC(2)	aug-cc-pVDZ[225]	4.60	4.85
CC2	aug-cc-pVDZ[224]	4.57	4.88
SA-CASSCF(14,10)	6-31G*[226]	5.30	5.17
ADC(2)	def2-SVP[226]	4.79	4.94

5.4.2   Isocytosine

The lowest two excitation energies of isocytosine as calculated using TDDFT at the Franck–Condon geometry differs with and without TDA approximation. They agree in characterizing the excited states, the lower S_1 being a bright $\pi \rightarrow \pi^*$ transition and S_2 being a dark $n_o \rightarrow \pi^*$. However, within TDA, with increasing size of the basis set, the two excited states appear to become degenerate. Such is not observed when using the full response equations to calculate the excitation energies and the S_2–S_1 gap converges to ~ 0.25 eV (see Table 5.3). Excitation energies and character using other electronic structure methods reported in the literature vary substantially, indicating the difficulty of characterizing the excited states of isocytosine (see Table 5.4). The scope of this study, however, is to compare the performance of TDDFT with different decoherence corrections to the FSSH algorithm, and detailed analysis of the excited state characters of isocytosine is left for further investigation.

The consequence of the S_2–S_1 degeneracy within TDA is well captured in the surface hopping dynamics of isocytosine using the def2-SVP basis for the electronic structure calculation. The swarm populations transfer completely from the initial S_2 to S_1 state in less than 200 fs irrespective of the choice of the nuclear dynamics method (see Figure 5.5). However, in case of FSSH, the

Table 5.5: Lifetimes of $S_2 \rightarrow S_1$ and $S_1 \rightarrow S_0$ decays for isocytosine using the three methods. The window of 95% confidence interval is mentioned in parenthesis.

	FSSH		A-FSSH	GP
$S_2 \rightarrow S_1$ decay times in fs				
Electronic population	5	(3 - 11)	22 (19 - 39)	47 (34 - 72)
Swarm population	13	(11 - 16)	36 (30 - 45)	61 (48 - 82)
$S_1 \rightarrow S_0$ decay times in ps				
Electronic population	4.5	(3.2 - 7.0)	1.0 (0.7 - 1.5)	0.8 (0.6 - 1.1)
Swarm population	0.6	(0.4 - 0.9)	0.9 (0.6 - 1.2)	0.8 (0.6 - 1.2)

electronic populations do not reflect the swarm population, with the electronic populations on S_1 and S_2 reaching an equilibrium around 200 fs. The inconsistency in the electronic and swarm population is however removed when the two decoherence corrections are added (see Figure 5.5). In both sets of simulations using A-FSSH and GP, the nuclear and the electronic populations remain practically identical. The detailed S_2–S_1 lifetimes are tabulated in Table 5.5.

In case of FSSH, over a longer period of time, the electronic populations in S_0 slowly increases with loss of population from both S_2 and S_1 states. The S_1–S_0 hops are mediated through one of two known conical intersection, namely EthylI and EthylII; the naming convention being kept as in Ref. 243 (see Figure 5.6). While the inconsistency between the electronic and the swarm populations are prominent in FSSH, the decoherence corrected methods make the swarm populations consistent with the electronic populations. The S_1–S_0 lifetimes calculated from the swarm populations are 0.6 ps for FSSH, 0.9 ps for A-FSSH and 0.8 ps for GP (see Table 5.5). Although, the FSSH results are inconsistent, the qualitative description of the dynamics involving FSSH and its decoherence-corrected variants remain the same. The lifetimes calculated in this work are closer to the lifetimes calculated using GP for the nonadiabatic dynamics and SA-CASSCF for the electronic properties in Ref. 226. The predominant contribution of the Ethyl I and Ethyl II conical intersection to the ultrafast decay pathway of isocytosine is also similar between the dynamics from TDDFT and SA-CASSCF trajectories and opposed to the C=O stretching pathway being predominant when using ADC(2) surfaces.[226]

For isocytosine, two distinct trends emerge on addition of the decoherence corrections to FSSH.
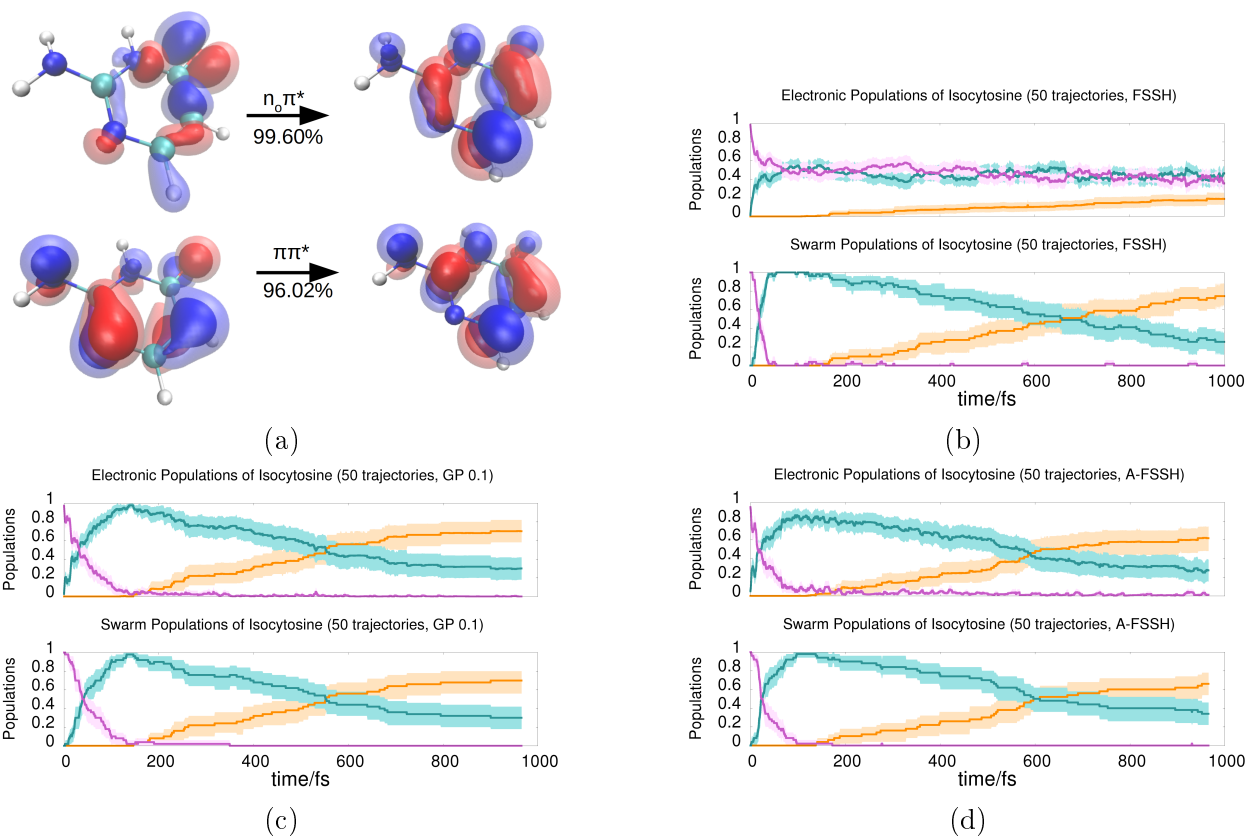
Figure 5.5: a) The dominant natural transition orbitals (NTOs) of the lowest two excitations at the Franck–Condon geometry. The contours of the orbitals are plotted with $\pm$ isovalues of 0.04 and 0.07 au. The singular values of the transitions are indicated under each arrow. Electronic and swarm populations of S_2 (magenta), S_1 (cyan) , S_0 (orange) of isocytosine using b) FSSH, b) GP and c)A-FSSH are shown. The same color shadings represent a bootstrap confidence interval of 95%.

Table 5.6: Decay lifetimes τ_0 and τ_2 of isocytosine in ps.

Method	τ_0	τ_2
ADC(2)/GP[225]	0.185	−
S2-ADC(2)/GP[226]	0.350	0.250
S2-CASSCF/GP[226]	$\approx$1.0	< 0.1
This work		
PBE0/FSSH	0.6	0.01
PBE0/A-FSSH	0.9	0.04
PBE0/GP	0.8	0.06
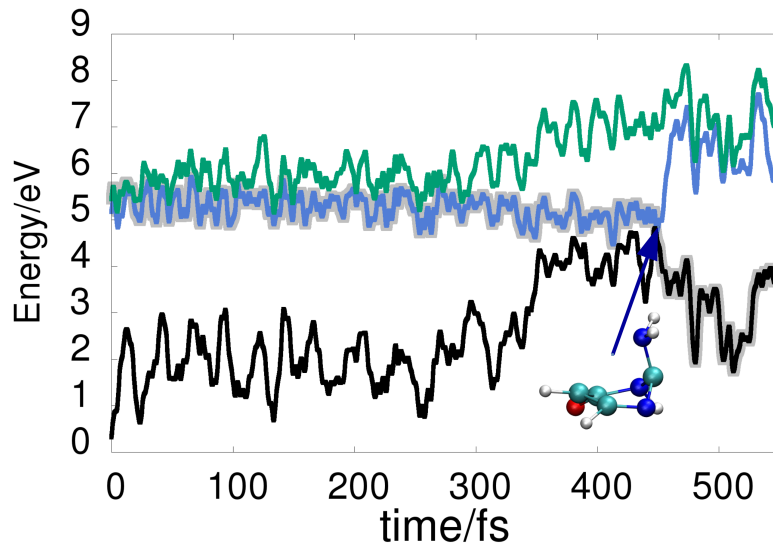
Figure 5.6: Energy of electronic states S_2 (green), S_1 (blue) and S_0 (black) of an example trajectory of isocytosine using FSSH. The active state is highlighted with gray shading. The trajectory decays through an Ethyl II conical intersection, the structure depicted in the inset.

As with thymine, the inconsistency between the electronic populations and the swarm populations is removed. As a result, all modes of ensemble averaging provide qualitatively the same result. Not surprisingly, the lifetimes estimated for isocytosine from decoherence corrected methods are longer than lifetimes estimated from FSSH. In case of A-FSSH, the occasional collapse of the electronic density matrix results in resetting the probability of hopping to zero. In case of GP, the continuous decay of the coherence between the electronic states results in reduced probabilities of hopping compared to FSSH. The only exception to this trend is the case of estimating the $S_1 \rightarrow S_0$ decay lifetime from the electronic population, where ensemble averages do not agree between the electronic and swarm populations. Due to the lack of experimental evidence for excited state lifetimes, the correctness of the decay pathways predicted in our simulations for isocytosine remains to be elucidated.

5.5 Conclusion

FSSH was designed such that the nuclear population in the ensemble follow the electronic populations and simulate the effects on molecular dynamics due to electronic population transfer. The interpretation of the trajectories hence become difficult in case of inconsistent swarm and electronic populations. The source of the inconsistency is often linked with the frustrated hops, where the active state is unable to hop to an electronic state higher in energy due to kinetic energy constraints.[222] A-FSSH and GP can improve upon the problem of inconsistency of electronic and swarm populations in FSSH. This inconsistency arises due to the probability to hop between two states in FSSH being estimated from a two-level system. However, this consistency for A-FSSH and GP comes at a price: it fails to capture the decay of population to the ground state for thymine. We observe that none of the trajectories hopped to the ground state in 2 ps of simulation, which is in contradiction to the results from FSSH. The over-coherent trajectories allowed for hops to the ground state of thymine even when the electronic population of the ground state was negligible.

In FSSH simulations, we observe several frustrated hops from $S_1 \rightarrow S_2$ in which the nuclear kinetic energy along the nonadiabatic vector was not sufficient to compensate for the excitation energy despite the total nuclear kinetic energy being adequate for the hop. The distinction between the two kinds of frustrated hops has been recently been pointed out by González and coworkers.[232] It is suggested that reflecting the momenta yields better results. Effects of reflecting the momenta upon encountering a frustrated hop for isocytosine and thymine dynamics remain a future research topic.

From our simulations, it appears that the effect of decoherence corrections is less pronounced than the discrepancies arising from the potential energy surfaces. With a classical nuclear model, the lack of accessible S_1–S_0 conical intersections for thymine, from both CASSCF and TDDFT based potential energy surfaces, makes it hard to justify the ultrafast decay of thymine, and other effects such as vibronic coupling for non-radiative decay of thymine should be considered for future examination. The only conical intersection found in this work has a barrier of 1.3 eV, making it inaccessible in low nuclear kinetic energy. In case of isocytosine, the EthylI and EthylII S_1–S_0 conical intersections become the primary channels of internal conversion, and adding the decoherence

corrections improves the consistency among the electronic and swarm populations.

Although the two decoherence corrections to FSSH is derived from different perspectives, the similarity in the isocytosine dynamics for both the decoherence corrections is striking. The simple post-dynamics correction to the density matrix as prescribed in GP achieves the same results as the parameter free A-FSSH. The computational expense of A-FSSH is higher than GP, but is not noticed in our simulation due to the computation of the energy, energy gradients and couplings being the bottleneck. The similarity in the results from GP and A-FSSH simulations indicates that although GP has an adjustable parameter, it can be used instead of A-FSSH in situations where calculating the electronic properties is no longer the rate-limiting step of the simulation.

The implementation of different decoherence corrections to FSSH will be available through Turbomole software package.[65]

Chapter 6

Conclusion and outlook

The thesis comprises a route by which molecular photochemistry involving multiple electronic states may be studied *in-silico*. The application of the TD-DFT/FSSH approach to study nonadiabatic phenomenon is presented in this thesis. The accuracy and limitations of this methodology is also discussed in this work.

DFT and TDDFT was used to explain the electronic structure of the first square planar actinide complex to be synthesized. A π-donating ligand field theory was proposed to explain the uncommon low-lying d_{z^2} orbital in the square planar coordination, and was supported by simulated UV/Vis spectrum matching with the experimentally observed one. This study adds more evidence towards using DFT and TDDFT as an accurate methods for modeling electronic adiabatic states. The availability of efficient implementation to compute the gradients and nonadiabatic coupling vectors between the adiabatic states was utilized to study several photochemical processes. Based on the TDDFT/FSSH simulation data for 5-methoxyquinoline, an alternate mechanism for its photobasicity of was proposed. The validity of the Förster cycle to explain photoacidity/basicity was reevaluated and the participation of water molecules in the excited state dynamics is observed. The photodynamics of thymine and isocytosine involving multiple electronic states was investigated using the same methodology. The mechanism for the ultrafast decay of thymine, the nucleobase with

the longest excited state lifetime, is not well understood, and the various competing hypotheses about its internal conversion mechanism, along with new data from the TDDFT/FSSH simulations, was discussed in this thesis. The decay of thymine from the S_2 to S_1 was observed through a ring puckering conical intersection. However, no S_1–S_2 conical intersections were encountered in the dynamics of thymine. Isocytosine, on the decayed through previously identified conical intersections to the ground state. The effects of decoherence corrections to the FSSH algorithm were studied for thymine and isocytosine, and improvement in the internal consistency between the swarm and the electronic populations was observed. The decoherence corrections, however, predicts no ultrafast decay to the ground state for thymine, which is seemingly unphysical.

Of the various shortcomings of the method, the lack of the correct topology of the PES near a degenerate ground state obtained from TDDFT calculations is perhaps the most critical problem.[188] Further development in addressing near-generate ground state within DFT/TDDFT is required. This thesis demonstrates that the limitations arising from the over coherent trajectories in FSSH are less crucial than the correct and robust description of the potential energy surface.

Bibliography

[1] WWAP (United Nations World Water Assessment Programme): The United Nations World Water Development Report 2018: Nature-Based Solutions for Water., UNESCO, Paris, 2018.

[2] WWAP (United Nations World Water Assessment Programme): The United Nations World Water Development Report 2014: Water and Energy, UNESCO, Paris, 2014.

[3] B. Hönisch, A. Ridgwell, D. N. Schmidt, E. Thomas, S. J. Gibbs, A. Sluijs, R. Zeebe, L. Kump, R. C. Martindale, S. E. Greene, W. Kiessling, J. Ries, J. C. Zachos, D. L. Royer, S. Barker, T. M. Marchitto Jr., R. Moyer, C. Pelejero, P. Ziveri, G. L. Foster, and B. Williams: The Geological Record of Ocean Acidification, *Science* **335**, 1058–1063, 2012.

[4] T. J. B. Wilson, S. R. Cooley, T. C. Tai, W. W. L. Cheung, and P. H. Tyedmers: Potential Socioeconomic Impacts from Ocean Acidification and Climate Change Effects on Atlantic Canadian Fisheries, *PLoS ONE* **15**, e0226544, 2020.

[5] United Nations , Department of Economic and Social Affairs , Population Division (2019). *World Population Prospects 2019: Methodology of the United Nations Population Estimates and Projections* (ST/ESA/SER.A/425).

[6] L. A. Weinstein, J. Loomis, B. Bhatia, D. M. Bierman, E. N. Wang, and G. Chen: Concentrating Solar Power, *Chem. Rev.* **115**, 12797–12838, 2015.

[7] G. H. Carey, A. L. Abdelhady, Z. Ning, S. M. Thon, O. M. Bakr, and E. H. Sargent: Colloidal Quantum Dot Solar Cells, *Chem. Rev.* **115**, 12732–12763, 2015.

[8] Z. Wang, C. Li, and K. Domen: Recent Developments in Heterogeneous Photocatalysts for Solar-Driven Overall Water Splitting, *Chem. Soc. Rev.* **48**, 2109–2125, 2019.

[9] G. R. Garbarini, R. F. Eaton, T. K. Kwei, and A. V. Tobolsb: Diffusion and reverse osmosis through polymer membranes, *J. Chem. Ed.* **48**, 226, 1971.

[10] M. Bui, C. S. Adjiman, A. Bardow, E. J. Anthony, A. Boston, S. Brown, P. S. Fennell, S. Fuss, A. Galindo, L. A. Hackett, J. P. Hallett, H. J. Herzog, G. Jackson, J. Kemper, S. Kervor, G. C. Maitland, M. Matuszewski, C. Metcalfe, Ian S. Petit, G. Puxty, J. Reimer, D. M. Reiner, E. S. Rubin, S. S. A., N. Shah, B. Smit, J. P. M. Trusler, P. Webley, J. Wilcox, and N. M. Dowell: Carbon Capture and Storage (CCS): The Way Forward, *Energy Environ. Sci.* **11**, 1062–1176, 2018.

[11] J. Lilliestam, M. Labordena, A. Patt, and S. Pfenninger: Empirically Observed Learning Rates for Concentrating Solar Power and their Responses to Regime Change, *Nature Energy* **2**, 2017.

[12] A. J. Carrillo, J. González-Aguilar, M. Romero, and J. M. Coronado: Solar Energy on Demand: A Review on High Temperature Thermochemical Heat Storage Systems and Materials, *Chem. Rev.* **119**, 4777–4816, 2019.

[13] D. Spasiano, R. Marotta, S. Malato, P. Fernandez-Ibañez, and I. Di Somma: Solar Photocatalysis: Materials, Reactors, some Commercial, and Pre-Industrialized Applications. A Comprehensive Approach, *Appl. Catal. B-Env.* **170-171**, 90–123, 2015.

[14] N. S. Lewis and D. G. Nocera: Powering the Planet: Chemical Challenges in Solar Energy Utilization, *Proc. Natl. Acad. Sci. U.S.A.* **103**(43), 15729–15735, 2006.

[15] M. Born and R. Oppenheimer: Zur Quantentheorie der Molekeln, *Ann. Phys.* **389**(20), 457–484, 1927.

[16] J. C. Tully: Perspective: Nonadiabatic Dynamics Theory, *J. Chem. Phys.* **137**, 22A301, 2012.

[17] F. Furche and R. Ahlrichs: Adiabatic time-dependent density functional methods for excited state properties, *J. Chem. Phys.* **117**, 7433–7447, 2002.

[18] R. Send and F. Furche: First-order nonadiabatic couplings from time-dependent hybrid density functional response theory: Consistent formalism, implementation, and performance., *J. Chem. Phys.* **132**, 044107, 2010.

[19] E. Tapavicza, I. Tavernelli, and U. Rothlisberger: Trajectory Surface Hopping within Linear Response Time-Dependent Density-Functional Theory, *Phys. Rev. Lett.* **98**(2), 2007.

[20] E. Tapavicza, G. D. Bellchambers, J. C. Vincent, and F. Furche: Ab initio non-adiabatic molecular dynamics, *Phys. Chem. Chem. Phys.* **15**, 18336–18348, 2013.

[21] Q. Ou, G. D. Bellchambers, F. Furche, and J. E. Subotnik: First-order derivative couplings between excited states from adiabatic TDDFT response theory, *J. Chem. Phys.* **142**, 064114, 2015.

[22] J. C. Tully: Molecular dynamics with electronic transitions, *J. Chem. Phys.* **93**, 1061, 1990.

[23] M. J. Bedard-Hearn, R. E. Larsen, and B. J. Schwartz: Mean-Field Dynamics with Stochastic Decoherence (MF-SD): A New Algorithm for Nonadiabatic Mixed Quantum/Classical Molecular-Dynamics Simulations with Nuclear-Induced Decoherence, *J. Chem. Phys.* **123**(23), 234106, 2005.

[24] R. E. Larsen, M. J. Bedard-Hearn, and B. J. Schwartz: Exploring the Role of Decoherence in Condensed-Phase Nonadiabatic Dynamics: A Comparison of Different Mixed Quantum/Classical Simulation Algorithms for the Excited Hydrated Electron, *J. Phys. Chem. B* **110**(40), 20055–20066, 2006.

[25] G. Granucci and M. Persico: Critical Appraisal of the Fewest Switches Algorithm for Surface Hopping, *J. Chem. Phys.* **126**(13), 134114, 2007.

[26] G. Granucci, M. Persico, and A. Zoccante: Including Quantum Decoherence in Surface Hopping, *J. Chem. Phys.* **133**(13), 134111, 2010.

[27] J. E. Subotnik and N. Shenvi: A New approach to Decoherence and Momentum Rescaling in the Surface Hopping Algorithm, *J. Chem. Phys.* **134**(2), 024105, 2011.

[28] J. E. Subotnik: Fewest-Switches Surface Hopping and Decoherence in Multiple Dimensions, *J. Phys. Chem. A* **115**(44), 12083–12096, 2011.

[29] B. R. Landry and J. E. Subotnik: Communication: Standard Surface Hopping Predicts Incorrect Scaling for Marcus' Rolden-Rule Rate: The Decoherence Problem Cannot be Ignored, *J. Chem. Phys.* **135**(19), 191101, 2011.

[30] H. M. Jaeger, S. Fischer, and O. V. Prezhdo: Decoherence-Induced Surface Hopping, *J. Chem. Phys.* **137**(22), 22A545, 2012.

[31] A. Jain, E. Alguire, and J. E. Subotnik: An Efficient, Augmented Surface Hopping Algorithm That Includes Decoherence for Use in Large-Scale Simulations, *J. Chem. Theory Comput.* **12**(11), 5256–5268, 2016.

[32] S. K. Min, F. Agostini, I. Tavernelli, and E. K. U. Gross: Ab Initio Nonadiabatic Dynamics with Coupled Trajectories: A Rigorous Approach to Quantum (De)Coherence, *J. Phys. Chem. Lett.* **8**(13), 3048–3055, 2017.

[33] A. Jain and J. E. Subotnik: Vibrational Energy Relaxation: A Benchmark for Mixed Quantum-Classical Methods, *J. Phys. Chem. A* **122**(1), 16–27, 2017.

[34] T. Förster: Die pH-Abhängigkeit der Fluoreszenz von Naphthalinderivaten, *Elektrochem.* **54**, 1950.

[35] S. M. Parker, S. Roy, and F. Furche: Unphysical divergences in response theory, *J. Chem. Phys.* **145**, 134105, 2016.

[36] D. C. Bradley, M. A. Saad, and W. Wardlaw: The Preparation of Thorium Alkoxides, *J. Chem. Soc.* p. 1091, 1954.

[37] D. C. Bradley, M. A. Saad, and W. Wardlaw: Tertiary Alkoxides of Thorium, *J. Chem. Soc.* p. 3488, 1954.

[38] D. C. Bradley, A. K. Chatterjee, and W. Wardlaw: 439. Structural Chemistry of the Alkoxides. Part VI. Primary Alkoxides of Quadrivalent Cerium and Thorium, *J. Chem. Soc.* p. 2260, 1956.

[39] D. C. Bradley, A. K. Chatterjee, and W. Wardlaw: 671. Structural Chemistry of the Alkoxides. Part VII. Secondary Alkoxides of Quadrivalent Cerium and Thorium, *J. Chem. Soc.* p. 3469, 1956.

[40] P. C. Blake, M. F. Lappert, R. G. Taylor, J. L. Atwood, and H. Zhang: Some Aspects of the Coordination and Organometallic Chemistry of Thorium and Uranium (M^{III}, M^{IV}, U^{V}) in +3 and +4 Oxidation States, *Inorg. Chim. Acta* **139**, 13–20, 1987.

[41] P. B. Hitchcock, M. F. Lappert, A. Singh, R. G. Taylor, and D. Brown: Hydrocarbon-Soluble, Crystalline, Four-Co-ordinate Chloro(aryl oxide)s, Dialkylamido(aryl oxide)s and di[bis(trimethylsilyl)cyclopentadienyl]s of Th^{IV} and U^{IV}; X-ray Crystal Structure of Diethylamidotris(2,6-di-t-butylphenoxo)uranium(IV), *J. Chem. Soc., Chem. Commun.* p. 561, 1983.

[42] J. M. Berg, D. L. Clark, J. C. Huffman, D. E. Morris, A. P. Sattelberger, W. E. Streib, W. G. Van der Sluys, and J. G. Watkin: Early Actinide Alkoxide Chemistry. Synthesis, Characterization, and Molecular Structures of Thorium(IV) and Uranium(IV) Aryloxide Complexes, *J. Am. Chem. Soc.* **114**, 10811–10821, 1992.

[43] J. S. Parry, Cloke, S. J. Coles, and M. B. Hursthouse: Synthesis and Characterization of the First Sandwich Complex of Trivalent Thorium: A Structural Comparison with the Uranium Analogue, *J. Am. Chem. Soc.* **121**, 6867–6871, 1999.

[44] P. C. Blake, N. M. Edelstein, P. B. Hitchcock, W. K. Kot, M. F. Lappert, G. V. Shalimoff, and S. Tian: Synthesis, Properties and Structures of the Tris(cyclopentadienyl)thorium(III) Complexes [Th$\{\eta_5$-C$_5$H$_3$(SiMe$_2$R)$_2$-1,3$\}_3$] (R=Me or tBu), *J. Organomet. Chem.* **636**, 124–129, 2001.

[45] J. R. Walensky, R. L. Martin, J. W. Ziller, and W. J. Evans: Importance of Energy Level Matching for Bonding in Th^{3+}-Am^{3+} Actinide Metallocene Amidinates, (C$_5$Me$_5$)$_2$[^{i}PrNC(Me)N^{i}Pr]An, *Inorg. Chem.* **49**, 10007–10012, 2010.

[46] N. A. Siladke, C. L. Webster, J. R. Walensky, M. K. Takase, J. W. Ziller, D. J. Grant, L. Gagliardi, and W. J. Evans: Actinide Metallocene Hydride Chemistry: C-H Activation in Tetramethylcyclopentadienyl Ligands to Form [μ-η_5-C$_5$Me$_3$H(CH$_2$)-κC]$^{2-}$ Tuck-over Ligands in a Tetrathorium Octahydride Complex, *Organometallics* **32**, 6522–6531, 2013.

[47] R. R. Langeslay, M. E. Fieser, J. W. Ziller, F. Furche, and W. J. Evans: Expanding Thorium Hydride Chemistry Through Th^{2+}, Including the Synthesis of a Mixed-Valent Th^{4+}/Th^{3+} Hydride Complex, *J. Am. Chem. Soc.* **138**, 4036–4045, 2016.

[48] R. R. Langeslay, G. P. Chen, C. J. Windorff, A. K. Chan, J. W. Ziller, F. Furche, and W. J. Evans: Synthesis, Structure, and Reactivity of the Sterically Crowded Th^{3+} Complex (C$_5$Me$_5$)$_3$Th Including Formation of the Thorium Carbonyl, [(C$_5$Me$_5$)$_3$Th(CO)][BPh$_4$], *J. Am. Chem. Soc.* **139**, 3387–3398, 2017.

[49] A. Formanuik, A.-M. Ariciu, F. Ortu, R. Beekmeyer, A. Kerridge, F. Tuna, E. J. L. McInnes, and D. P. Mills: Actinide Covalency Measured by Pulsed Electron Paramagnetic Resonance Spectroscopy, *Nat. Chem.* **9**, 578–583, 2017.

[50] A. B. Altman, A. C. Brown, G. Rao, T. D. Lohrey, R. D. Britt, L. Maron, S. G. Minasian, D. K. Shuh, and J. Arnold: Chemical Structure and Bonding in a Thorium(III)-Aluminum Heterobimetallic Complex, *Chem. Sci.* **9**, 4317–4324, 2018.

[51] I. Korobkov, A. Arunachalampillai, and S. Gambarotta: Cyclometalation and Solvent Deoxygenation during Reduction of a Homoleptic Th(OAr)$_4$ Complex: Serendipitous Formation of a Terminally Bonded Th–OH Function, *Organometallics* **23**, 6248–6252, 2004.

[52] H. Yin, A. J. Lewis, U. J. Williams, P. J. Carroll, and E. J. Schelter: Fluorinated Diarylamide Complexes of Uranium(III,IV) Incorporating Ancillary Fluorine-to-Uranium Dative Interactions, *Chem. Sci.* **4**, 798–805, 2013.

[53] S. M. Mansell, N. Kaltsoyannis, and P. L. Arnold: Small Molecule Activation by Uranium Tris(aryloxides): Experimental and Computational Studies of Binding of N$_2$, Coupling of CO, and Deoxygenation Insertion of CO$_2$ under Ambient Conditions, *J. Am. Chem. Soc.* **133**, 9036–9051, 2011.

[54] J. Tao, J. P. Perdew, V. N. Staroverov, and G. E. Scuseria: Climbing the Density Functional Ladder: Nonempirical Meta-Generalized Gradient Approximation Designed for Molecules and Solids, *Phys. Rev. Lett.* **91**, 2003.

[55] S. Grimme: Semiempirical GGA-type density functional constructed with a long-range dispersion correction, *J. Comput. Chem.* **27**, 1787–1799, 2006.

[56] W. Küchle, M. Dolg, H. Stoll, and H. Preuss: Energy-Adjusted Pseudopotentials for the Actinides. Parameter Sets and Test Calculations for Thorium and Thorium Monoxide, *J. Chem. Phys.* **100**, 7535–7542, 1994.

[57] X. Cao and M. Dolg: Segmented contraction scheme for small-core actinide pseudopotential basis sets, *J. Mol. Struct. (THEOCHEM)* **673**, 203–209, 2004.

[58] A. Schäfer, H. Horn, and R. Ahlrichs: Fully optimized contracted Gaussian basis sets for atoms Li to Kr, *J. Chem. Phys.* **97**, 2571–2577, 1992.

[59] O. Treutler and R. Ahlrichs: Efficient molecular numerical integration schemes, *J. Chem. Phys.* **102**, 346–354, 1995.

[60] B. I. Dunlap, J. W. D. Connolly, and J. R. Sabin: On Some Approximations in Applications of Xα Theory, *J. Chem. Phys.* **71**, 3396–3402, 1979.

[61] A. Schäfer, A. Klamt, D. Sattel, J. C. W. Lohrenz, and F. Eckert: COSMO Implementation in TURBOMOLE: Extension of an efficient quantum chemical code towards liquid systems, *Phys. Chem. Chem. Phys.* **2**, 2187–2193, 2000.

[62] D. R. Lide, editor: CRC Handbook of Chemistry and Physics, CRC Press, 88 edition, 2008.

[63] C. Adamo and V. Barone: Toward Reliable Density Functional Methods without Adjustable Parameters: The PBE0 Model, *J. Chem. Phys.* **110**, 6158–6170, 1999.

[64] CRC Handbook: CRC Handbook of Chemistry and Physics, 88th Edition, CRC Press, 88 edition, 2007.

[65] F. Furche, R. Ahlrichs, C. Hättig, W. Klopper, M. Sierka, and F. Weigend: Turbomole, *Wiley Interdiscip. Rev.: Comput. Mol. Sci.* **4**, 91–100, 2013.

[66] M. K. Thomsen, A. Nyvang, J. P. S. Walsh, P. C. Bunting, J. R. Long, F. Neese, M. Atanasov, A. Genoni, and J. Overgaard: Insights into Single-Molecule-Magnet Behavior from the Experimental Electron Density of Linear Two-Coordinate Iron Complexes, *Inorg. Chem.* **58**, 3211–3218, 2019.

[67] J. Chatt, G. A. Gamlen, and L. E. Orgel: 86. The Visible and Ultraviolet Spectra of Some Platinous Ammines, *J. Chem. Soc.* p. 486, 1958.

[68] S. Larsson, L.-F. Olsson, and A. Rosén: Electronic Structure of the $PdCl_4{}^{2-}$ and $PtCl_4{}^{2-}$ ions, *Int. J. Quantum Chem.* **25**, 201–209, 1984.

[69] R. Schrock: Catalytic Reduction of Dinitrogen to Ammonia by Molybdenum: Theory versus Experiment, *Angew. Chem.* **47**, 5512–5522, 2008.

[70] R. A. D. Soriaga, J. M. Nguyen, T. A. Albright, and D. M. Hoffman: Diamagnetic Group 6 Tetrakis(di-tert-butylketimido)metal(IV) Complexes, *J. Am. Chem. Soc.* **132**, 18014–18016, 2010.

[71] R. A. Lewis, G. Wu, and T. W. Hayton: Synthesis and Characterization of an Iron(IV) Ketimide Complex, *J. Am. Chem. Soc.* **132**, 12814–12816, 2010.

[72] J. Cirera, P. Alemany, and S. Alvarez: Mapping the Stereochemistry and Symmetry of Tetra-coordinate Transition-Metal Complexes, *Chem. Eur. J.* **10**, 190–207, 2004.

[73] A. F. Holleman and E. Wiberg: Inorganic Chemistry, Academic Press, Berlin, 1st edition, 2001.

[74] R. H. Crabtree: The Organometallic Chemistry of the Transition Metals, John Wiley & Sons, Hoboken, NJ, 5th edition, 2009.

[75] J. F. Hartwig: Organotransition Metal Chemistry, University of Science Books, Mill Valley, CA, 1st edition, 2010.

[76] D. L. Kepert: Aspects of the Stereochemistry of Eight-Coordination, pp. 179–249, John Wiley & Sons, Ltd, 2007.

[77] S. J. Lippard: Eight-Coordination Chemistry, pp. 109–193, John Wiley & Sons, Ltd, 2007.

[78] D. J. Liptrot and P. P. Power: London Dispersion Forces in Sterically Crowded Inorganic and Organometallic Molecules, *Nat. Rev. Chem.* **1**, 2017.

[79] E. Osawa, Y. Onuki, and K. Mislow: The Central Bond Length in Hexaphenylethane and Hexakis(2,6-di-tert-butyl-4-biphenylyl)ethane, *J. Am. Chem. Soc.* **103**, 7475–7479, 1981.

[80] W. D. Hounshell, D. A. Dougherty, J. P. Hummel, and K. Mislow: Structure of Hexaphenylethane and Congeners as Determined by Empirical Force Field Calculations, *J. Am. Chem. Soc.* **99**, 1916–1924, 1977.

[81] S. Grimme and P. R. Schreiner: Steric Crowding Can Stabilize a Labile Molecule: Solving the Hexaphenylethane Riddle, *Angew. Chem.* **50**, 12639–12642, 2011.

[82] B. Kahr, D. Van Engen, and K. Mislow: Length of the Ethane Bond in Hexaphenylethane and Its Derivatives, *J. Am. Chem. Soc.* **108**, 8305–8307, 1986.

[83] D. B. Spry and M. D. Fayer: Charge Redistribution and Photoacidity: Neutral versus Cationic Photoacids, *J. Chem. Phys.* **128**, 084508, 2008.

[84] N. Mataga, Y. Kaifu, and M. Koizumi: On the Base Strength of Some Nitrogen Heterocycles in the Excited State, *Bull. Chem. Soc. Jpn.* **29**, 373–379, 1956.

[85] E. Pines, D. Huppert, M. Gutman, N. Nachliel, and M. Fishman: The pOH Jump: Determination of Deprotonation Rates of Water by 6-Methoxyquinoline and Acridin, *J. Phys. Chem.* **90**, 6366–6370, 1986.

[86] W. Zhou, S. M. Kuebler, K. L. Braun, T. Yu, J. K. Cammack, C. K. Ober, J. W. Perry, and S. R. Marder: An Efficient Two-Photon-Generated Photoacid Applied to Positive-Tone 3D Microfabrication, *Science* **296**, 1106–1109, 2002.

[87] J. V. Crivello: The Discovery and Development of Onium Salt Cationic Photoinitiators, *J. Polym. Sci. A* **37**, 4241–4254, 1999.

[88] N. Amdursky: Photoacids as a New Fluorescence Tool for Tracking Structural Transitions of Proteins: Following the Concentration-Induced Transition of Bovine Serum Albumin, *Phys. Chem. Chem. Phys.* **17**, 32023–32032, 2015.

[89] W. White, C. D. Sanborn, R. S. Reiter, D. M. Fabian, and S. Ardo: Observation of Photovoltaic Action from Photoacid-Modified Nafion Due to Light-Driven Ion Transport, *J. Am. Chem. Soc.* **139**, 11726–11733, 2017.

[90] A. Weller: Fast Reactions of Excited Molecules, *Prog. React. Kinet.* **1**, 187–214, 1961.

[91] N. Lasser and J. Feitelson: Excited State pK_a Values from Fluorescence Measurements, *J. Phys. Chem.* **77**, 1011–1016, 1973.

[92] B. Finkler, C. Spies, M. Vester, F. Walte, K. Omlor, I. Riemann, M. Zimmer, F. Stracke, M. Gerhards, and G. Jung: Highly Photostable "Super"-Photoacids for Ultrasensitive Fluorescence Spectroscopy, *Photochem. Photobiol. Sci.* **13**, 548–562, 2014.

[93] L. M. Tolbert and K. M. Solntsev: Excited-State Proton Transfer: From Constrained Systems to "Super" Photoacids to Superfast Proton Transfer, *Acc. Chem. Res.* **35**, 19–27, 2002.

[94] J. V. Crivello and J. H. W. Lam: Photoinitiated Cationic Polymerization with Triarylsulfonium Salts, *J. Polym. Sci. Polym. Chem. Ed.* **17**, 977–999, 1979.

[95] A. V. Akimov, A. J. Neukirch, and O. V. Prezhdo: Theoretical Insights into Photoinduced Charge Transfer and Catalysis at Oxide Interfaces, *Chem. Rev.* **113**, 4496–4565, 2013.

[96] H. Lischka, D. Nachtigalloviá, A. J. A. Aquino, P. G. Szalay, F. Plasser, F. B. C. Machado, and M. Barbatti: Multireference Approaches for Excited States of Molecules, *Chem. Rev.* **118**, 7293–7361, 2018.

[97] W. Domcke and A. L. Sobolewski: Unraveling the Molecular Mechanisms of Photoacidity, *Science* **302**, 1693–1694, 2003.

[98] A. L. Sobolewski, W. Domcke, C. Dedonder-Lardeux, and C. Jouvet: Excited-state Hydrogen Detachment and Hydrogen Transfer Driven by Repulsive $^1\pi\sigma^*$ States: A New Paradigm for Nonradiative Decay in Aromatic Biomolecules, *Phys. Chem. Chem. Phys.* **4**, 1093–1100, 2002.

[99] E. W. Driscoll, J. R. Hunt, and J. M. Dawlaty: Photobasicity in Quinolines: Origin and Tunability via the Substituents' Hammett Parameters, *J. Phys. Chem. Lett.* **7**, 2093–2099, 2016.

[100] E. W. Driscoll, J. R. Hunt, and J. M. Dawlaty: Proton Capture Dynamics in Quinoline Photobases: Substituent Effect and Involvement of Triplet States, *J. Phys. Chem. A* **121**, 7099–7107, 2017.

[101] J. R. Hunt and J. M. Dawlaty: Photodriven Deprotonation of Alcohols by a Quinoline Photobase, *J. Phys. Chem. A.* **122**, 7931–7940, 2018.

[102] A. Trofimov, I. Krivdina, J. Weller, and J. Schirmer: Algebraic-Diagrammatic Construction Propagator Approach to Molecular Response Properties, *Chem. Phys.* **329**, 1 – 10, 2006, electron Correlation and Multimode Dynamics in Molecules.

[103] C. Hättig: Structure Optimizations for Excited States with Correlated Second-Order Methods: CC2 and ADC(2), in H. Jensen, editor, Response Theory and Molecular Properties (A Tribute to Jan Linderberg and Poul Jørgensen), volume 50 of *Advances in Quantum Chemistry*, pp. 37 – 60, Academic Press, 2005.

[104] S. Grimme, J. Antony, S. Ehrlich, and H. Krieg: A Consistent and Accurate Ab Initio Parametrization of Density Functional Dispersion Correction (DFT-D) for the 94 Elements H-Pu, *J. Chem. Phys.* **132**, 154104, 2010.

[105] F. Weigend, F. Furche, and R. Ahlrichs: Gaussian Basis Sets of Quadruple Zeta Valence Quality for Atoms H-Kr, *J. Chem. Phys.* **119**, 12753–12762, 2003.

[106] R. W. Hockney and J. W. Eastwood: Computer Simulation using Particles, McGraw-Hill International Book Co., 1981.

[107] A. Klamt and G. Schüürmann: COSMO: a new approach to dielectric screening in solvents with explicit expressions for the screening energy and its gradient, *J. Chem. Soc., Perkin Trans. 2* pp. 799–805, 1993.

[108] TURBOMOLE V7.4 2019, a development of University of Karlsruhe and Forschungszentrum Karlsruhe GmbH, 1989-2007, TURBOMOLE GmbH, since 2007; available from http://www.turbomole.com.

[109] A. Einstein: On the Quantum Theory of Radiation, *Phys. Z.* **18**, 121, 1917.

[110] D. J. Tozer, R. D. Amos, N. C. Handy, B. O. Roos, and L. Serrano-Andrés: Does Density Functional Theory Contribute to the Understanding of Excited States of Unsaturated Organic Compounds?, *Mol. Phys.* **97**, 859–868, 1999.

[111] A. Dreuw, J. L. Weisman, and M. Head-Gordon: Long-Range Charge-Transfer Excited States in Time-Dependent Density Functional Theory Require Non-Local Exchange, *J. Chem. Phys.* **119**, 2943–2946, 2003.

[112] A. Dreuw and M. Head-Gordon: Failure of Time-Dependent Density Functional Theory for Long-range Charge-Transfer Excited States: the Zincbacteriochlorin–Bacteriochlorin and Bacteriochlorophyll–Spheroidene Complexes, *J. Am. Chem. Soc.* **126**, 4007–4016, 2004.

[113] C. M. Isborn, B. D. Mar, B. F. E. Curchod, I. Tavernelli, and T. J. Martínez: The Charge Transfer Problem in Density Functional Theory Calculations of Aqueously Solvated Molecules, *J. Phys. Chem. B* **117**, 12189–12201, 2013.

[114] H. Li, R. Nieman, A. J. A. Aquino, H. Lischka, and S. Tretiak: Comparison of LC-TDDFT and ADC(2) Methods in Computations of Bright and Charge Transfer States in Stacked Oligothiophenes, *J. Chem. Theory Comput.* **10**, 3280–3289, 2014.

[115] A. Bernas and D. Grand: The So-Called Ionization Potential of Water and Associated Liquids, *J. Phys. Chem.* **98**, 3440–3443, 1994.

[116] X. Cai, M. Sakamoto, M. Fujitsuka, and T. Majima: One-Electron Oxidation of Alcohols by the 1,3,5-Trimethoxybenzene Radical Cation in the Excited State during Two-Color Two-Laser Flash Photolysis, *J. Phys. Chem. A* **111**, 1788–1791, 2007.

[117] E. J. Rabe, K. L. Corp, A. L. Sobolewski, W. Domcke, and C. W. Schlenker: Proton-Coupled Electron Transfer from Water to a Model Heptazine-based Molecular Photocatalyst, *J. Phys. Chem. Lett.* **9**, 6257–6261, 2018.

[118] W. Domcke and D. R. Yarkony: Role of conical intersections in molecular spectroscopy and photoinduced chemical dynamics, *Annu. Rev. Phys. Chem.* **63**, 325–352, 2012.

[119] A. Zangwill and P. Soven: Density-functional approach to local-field effects in finite systems: Photoabsorption in the rare gases, *Phys. Rev. A* **21**, 1561–1572, 1980.

[120] E. Runge and E. K. U. Gross: Density-Functional Theory for Time-Dependent Systems, *Phys. Rev. Lett.* **52**, 997–1000, 1984.

[121] M. Petersilka, U. J. Gossmann, and E. K. U. Gross: Excitation Energies from Time-Dependent Density-Functional Theory, *Phys. Rev. Lett.* **76**, 1212–1215, 1996.

[122] E. K. U. Gross, J. F. Dobson, and M. Petersilka: Density functional theory of time-dependent phenomena, in Density Functional Theory II, pp. 81–172, Springer-Verlag, Berlin/Heidelberg, 1996.

[123] R. Baer: Non-adiabatic couplings by time-dependent density functional theory, *Chem. Phys. Lett.* **364**, 75–79, 2002.

[124] R. Baer, Y. Kurzweil, and L. S. Cederbaum: Time-dependent density functional theory for nonadiabatic processes, *Isr. J. Chem.* **45**, 161–170, 2005.

[125] F. Agostini, B. F. E. Curchod, R. Vuilleumier, I. Tavernelli, and E. K. U. Gross: TDDFT and Quantum-Classical Dynamics: A Universal Tool Describing the Dynamics of Matter, pp. 1–47, Springer International Publishing, Cham, 2018.

[126] C. F. Craig, W. R. Duncan, and O. V. Prezhdo: Trajectory surface hopping in the time-dependent Kohn-Sham approach for electron-nuclear dynamics, *Phys. Rev. Lett.* **95**, 163001, 2005.

[127] E. Tapavicza, I. Tavernelli, U. Rothlisberger, C. Filippi, and M. E. Casida: Mixed time-dependent density-functional theory/classical trajectory surface hopping study of oxirane photochemistry, *J. Chem. Phys.* **129**, 124108, 2008.

[128] T. Thompson and E. Tapavicza: First-Principles Prediction of Wavelength-Dependent Product Quantum Yields, *J. Chem. Phys.* **9**, 4758–4764, 2018.

[129] E. Tapavicza, A. M. Meyer, and F. Furche: Unravelling the details of vitamin D photosynthesis by non-adiabatic molecular dynamics simulations, *Phys. Chem. Chem. Phys.* **13**, 20986–20998, 2011.

[130] J. Kim, H. Tao, T. J. Martínez, and P. Bucksbaum: Ab initio multiple spawning on laser-dressed states: a study of 1,3-cyclohexadiene photoisomerization via light-induced conical intersections, *J. Phys. B: At., Mol. Opt. Phys.* **48**, 164003, 2015.

[131] O. Schalk, T. Geng, T. Thompson, N. Baluyot, R. D. Thomas, E. Tapavicza, and T. Hansson: Cyclohexadiene revisited: A time-resolved photoelectron spectroscopy and ab initio study, *J. Phys. Chem. A* **120**, 2320–2329, 2016.

[132] M. Barbatti, J. Pittner, M. Pederzoli, U. Werner, R. Mitrić, V. Bonačić-Koutecký, and H. Lischka: Non-adiabatic dynamics of pyrrole: Dependence of deactivation mechanisms on the excitation energy, *Chem. Phys.* **375**, 26–34, 2010.

[133] M. Sapunar, A. Ponzi, S. Chaiwongwattana, M. Mališ, A. Prlj, P. Decleva, and N. Došlić: Timescales of N-H bond dissociation in pyrrole: a nonadiabatic dynamics study, *Phys. Chem. Chem. Phys.* **17**, 19012–19020, 2015.

[134] M. Wohlgemuth, V. Bonačić-Koutecký, and R. Mitrić: Time-dependent density functional theory excited state nonadiabatic dynamics combined with quantum mechanical/molecular mechanical approach: Photodynamics of indole in water, *J. Chem. Phys.* **135**, 054105, 2011.

[135] L. Du and Z. Lan: An on-the-fly surface-hopping program JADE for nonadiabatic molecular dynamics of polyatomic systems: Implementation and applications, *J. Chem. Theory Comput.* **11**, 1360–1374, 2015.

[136] R. Long, J. Liu, and O. V. Prezhdo: Unravelling the Effects of Grain Boundary and Chemical Doping on Electron-Hole Recombination in $CH_3NH_3PbI_3$ Perovskite by Time-Domain Atomistic Simulation, *J. Am. Chem. Soc.* **138**, 3884–3890, 2016.

[137] W. R. Duncan, W. M. Stier, and O. V. Prezhdo: Ab initio nonadiabatic molecular dynamics of the ultrafast electron injection across the alizarin-TiO_2 interface, *J. Am. Chem. Soc.* **127**, 7941–7951, 2005.

[138] W. R. Duncan, C. F. Craig, and O. V. Prezhdo: Time-domain ab initio study of charge relaxation and recombination in dye-sensitized TiO_2, *J. Am. Chem. Soc.* **129**, 8528–8543, 2007.

[139] M. Muuronen, S. M. Parker, E. Berardo, A. Le, M. A. Zwijnenburg, and F. Furche: Mechanism of photocatalytic water oxidation on small TiO_2 nanoparticles, *Chem. Sci.* **8**, 2179–2183, 2017.

[140] J. C. Vincent, M. Muuronen, K. C. Pearce, L. N. Mohanam, E. Tapavicza, and F. Furche: That little extra kick: Non-adiabatic effects in acetaldehyde photodissociation, *J. Phys. Chem. Lett.* **7**, 4185–4190, 2016.

[141] Y. Han, B. Rasulev, and D. S. Kilin: Photofragmentation of Tetranitromethane: Spin-Unrestricted Time-Dependent Excited-State Molecular Dynamics, *J. Phys. Chem. Lett.* **8**, 3185–3192, 2017.

[142] E. Tapavicza, I. Tavernelli, and U. Rothlisberger: Trajectory Surface Hopping within Linear Response Time-Dependent Density-Functional Theory, *Phys. Rev. Lett.* **98**, 023001, 2007.

[143] M. Wohlgemuth, V. Bonačić-Koutecký, and R. Mitrić: Nonadiabatic coupling vectors for excited states within time-dependent density functional theory in the Tamm–Dancoff approximation and beyond, *J. Chem. Phys.* **133**, 194104, 2010.

[144] I. Tavernelli, B. F. E. Curchod, and U. Rothlisberger: Nonadiabatic molecular dynamics with solvent effects: A LR-TDDFT QM/MM study of ruthenium (II) tris (bipyridine) in water, *Chem. Phys.* **391**, 101–109, 2011.

[145] B. Curchod, T. Penfold, U. Rothlisberger, and I. Tavernelli: Nonadiabatic ab initio molecular dynamics using linear-response time-dependent density functional theory, *Cent. Eur. J. Phys.* **11**, 1059, 2013.

[146] T. Nelson, S. Fernandez-Alberti, V. Chernyak, A. E. Roitberg, and S. Tretiak: Nonadiabatic Excited-State Molecular Dynamics Modeling of Photoinduced Dynamics in Conjugated Molecules, *J. Phys. Chem. B* **115**, 5402–5414, 2011.

[147] Z. Li, B. Suo, and W. Liu: First order nonadiabatic coupling matrix elements between excited states: Implementation and application at the TD-DFT and pp-TDA levels, *J. Chem. Phys.* **141**, 244105, 2014.

[148] X. Zhang and J. M. Herbert: Analytic derivative couplings in time-dependent density functional theory: Quadratic response theory versus pseudo-wavefunction approach, *J. Chem. Phys.* **142**, 064109, 2015.

[149] S. M. Parker, D. Rappoport, and F. Furche: Quadratic Response Properties from TDDFT: Trials and Tribulations, *J. Chem. Theory Comput.* **14**(2), 807–819, 2017.

[150] H. Kang, K. T. Lee, B. Jung, Y. J. Ko, and S. K. Kim: Intrinsic Lifetimes of the Excited State of DNA and RNA Bases, *J. Am. Chem. Soc.* **124**, 12958–12959, 2002.

[151] C. Canuel, M. Mons, F. Piuzzi, B. Tardivel, I. Dimicoli, and M. Elhanine: Excited states dynamics of DNA and RNA bases: Characterization of a stepwise deactivation pathway in the gas phase, *J. Chem. Phys.* **122**, 074316, 2005.

[152] S. Ullrich, T. Schultz, M. Z. Zgierski, and A. Stolow: Electronic relaxation dynamics in DNA and RNA bases studied by time-resolved photoelectron spectroscopy, *Phys. Chem. Chem. Phys.* **6**, 2796, 2004.

[153] E. Samoylova, H. Lippert, S. Ullrich, I. V. Hertel, W. Radloff, and T. Schultz: Dynamics of Photoinduced Processes in Adenine and Thymine Base Pairs, *J. Am. Chem. Soc.* **127**, 1782–1786, 2005.

[154] E. Samoylova, T. Schultz, I. V. Hertel, and W. Radloff: Analysis of ultrafast relaxation in photoexcited DNA base pairs of adenine and thymine, *Chem. Phys.* **347**, 376–382, 2008.

[155] J. González-Vázquez, L. González, E. Samoylova, and T. Schultz: Thymine Relaxation After UV Irradiation: The Role of Tautomerization and $\pi\sigma^*$ States, *Phys. Chem. Chem. Phys.* **11**(20), 3927, 2009.

[156] J. J. Szymczak, M. Barbatti, J. T. Soo Hoo, J. A. Adkins, T. L. Windus, D. Nachtigallová, and H. Lischka: Photodynamics Simulations of Thymine: Relaxation into the First Excited Singlet State, *J. Phys. Chem. A* **113**, 12686–12693, 2009.

[157] B. K. McFarland, J. P. Farrell, S. Miyabe, F. Tarantelli, A. Aguilar, N. Berrah, C. Bostedt, J. D. Bozek, P. H. Bucksbaum, J. C. Castagna, R. N. Coffee, J. P. Cryan, L. Fang, R. Feifel, K. J. Gaffney, J. M. Glownia, T. J. Martinez, M. Mucke, B. Murphy, A. Natan, T. Osipov, V. S. Petrović, S. Schorb, T. Schultz, L. S. Spector, M. Swiggers, I. Tenney, S. Wang, J. L. White, W. White, and M. Gühr: Ultrafast X-ray Auger probing of photoexcited molecular dynamics, *Nat. Commun.* **5**, 4235, 2014.

[158] C. E. Crespo-Hernández, B. Cohen, P. M. Hare, and B. Kohler: Ultrafast Excited-State Dynamics in Nucleic Acids, *Chem. Rev.* **104**(4), 1977–2020, 2004.

[159] S. Perun, A. L. Sobolewski, and W. Domcke: Conical Intersections in Thymine, *J. Phys. Chem. A* **110**, 13238–13244, 2006.

[160] G. Zechmann and M. Barbatti: Photophysics and Deactivation Pathways of Thymine, *J. Phys. Chem. A* **112**, 8273–8279, 2008.

[161] Z. Lan, E. Fabiano, and W. Thiel: Photoinduced Nonadiabatic Dynamics of Pyrimidine Nucleobases: On-the-Fly Surface-Hopping Study with Semiempirical Methods, *J. Phys. Chem. B* **113**, 3548–3555, 2009.

[162] M. Barbatti, A. J. A. Aquino, J. J. Szymczak, D. Nachtigallová, P. Hobza, and H. Lischka: Relaxation mechanisms of UV-photoexcited DNA and RNA nucleobases, *Proc. Natl Acad. Sci.* **107**, 21453–21458, 2010.

[163] D. Asturiol, B. Lasorne, G. A. Worth, M. A. Robb, and L. Blancafort: Exploring the sloped-to-peaked S_2/S_1 seam of intersection of thymine with electronic structure and direct quantum dynamics calculations, *Phys. Chem. Chem. Phys.* **12**, 4949, 2010.

[164] D. Picconi, V. Barone, A. Lami, F. Santoro, and R. Improta: The Interplay between $\pi\pi^*/n\pi^*$ Excited States in Gas-Phase Thymine: A Quantum Dynamical Study, *ChemPhysChem* **12**, 1957–1968, 2011.

[165] L. Stojanović, S. Bai, J. Nagesh, A. Izmaylov, R. Crespo-Otero, H. Lischka, and M. Barbatti: New Insights into the State Trapping of UV-Excited Thymine, *Molecules* **21**, 1603, 2016.

[166] R. Improta, F. Santoro, and L. Blancafort: Quantum Mechanical Studies on the Photophysics and the Photochemistry of Nucleic Acids and Nucleobases, *Chem. Rev.* **116**, 3540–3593, 2016.

[167] J. C. Tully and R. K. Preston: Trajectory Surface Hopping Approach to Nonadiabatic Molecular Collisions: The Reaction of H+ with D_2, *J. Chem. Phys.* **55**, 562–572, 1971.

[168] N. C. Blais and D. G. Truhlar: Trajectory-Surface-Hopping Study of Na($3p^2P$) +$H_2 \rightarrow$ Na($3s^2S$)+H_2(v', j', θ), *J. Chem. Phys.* **79**(3), 1334–1342, 1983.

[169] M. E. Casida: Recent advances in density functional methods, volume 1 of *Recent advances in computational chemistry*, chapter Time-Dependent Density Functional Response Theory for Molecules, pp. 155–192, World Scientific, Singapore, 1995.

[170] F. Furche: On the density matrix based approach to time-dependent density functional response theory, *J. Chem. Phys.* **114**, 5982–5992, 2001.

[171] E. Gross and W. Kohn: Time-Dependent Density-Functional Theory, in P.-O. Löwdin, editor, *Density Functional Theory of Many-Fermion Systems*, volume 21 of *Advances in Quantum Chemistry*, pp. 255 – 291, Academic Press, 1990.

[172] S. Fatehi, E. Alguire, Y. Shao, and J. E. Subotnik: Analytic derivative couplings between configuration-interaction-singles states with built-in electron-translation factors for translational invariance., *J. Chem. Phys.* **135**, 234105, 2011.

[173] X. Zhang and J. M. Herbert: Analytic derivative couplings for spin-flip configuration interaction singles and spin-flip time-dependent density functional theory, *J. Chem. Phys.* **141**, 064104, 2014.

[174] F. Furche, R. Ahlrichs, C. Wachsmann, E. Weber, A. Sobanski, F. Vögtle, and S. Grimme: Circular Dichroism of Helicenes Investigated by Time-Dependent Density Functional Theory, *J. Am. Chem. Soc.* **122**, 1717–1724, 2000.

[175] H. Weiss, R. Ahlrichs, and M. Häser: A direct algorithm for self-consistent-field linear response theory and application to C_{60}: Excitation energies, oscillator strengths, and frequency-dependent polarizabilities, *J. Chem. Phys.* **99**, 1262–1270, 1993.

[176] R. E. Stratmann, G. E. Scuseria, and M. J. Frisch: An efficient implementation of time-dependent density-functional theory for the calculation of excitation energies of large molecules, *J. Chem. Phys.* **109**, 8218–8224, 1998.

[177] S. J. A. van Gisbergen, J. G. Snijders, and E. J. Baerends: Implementation of time-dependent density functional response equations, *Comput. Phys. Commun.* **118**, 119–138, 1999.

[178] A. Görling, H. H. Heinze, S. P. Ruzankin, M. Staufer, and N. Rösch: Density- and density-matrix-based coupled Kohn–Sham methods for dynamic polarizabilities and excitation energies of molecules, *J. Chem. Phys.* **110**, 2785–2799, 1999.

[179] F. Furche, B. T. Krull, B. D. Nguyen, and J. Kwon: Accelerating molecular property calculations with nonorthonormal Krylov space methods, *J. Chem. Phys.* **144**, 174105, 2016.

[180] S. Hirata and M. Head-Gordon: Time-dependent density functional theory within the Tamm–Dancoff approximation, *Chem. Phys. Lett.* **314**, 291–299, 1999.

[181] S. Yarasi, S. Ng, and G. R. Loppnow: Initial Excited-State Structural Dynamics of Uracil from Resonance Raman Spectroscopy Are Different from Those of Thymine (5-Methyluracil), *J. Phys. Chem. B* **113**, 14336–14342, 2009.

[182] P. M. Hare, C. E. Crespo-Hernandez, and B. Kohler: Internal conversion to the electronic ground state occurs via two distinct pathways for pyrimidine bases in aqueous solution, *Proc. Natl Acad. Sci.* **104**, 435–440, 2007.

[183] D. Asturiol, B. Lasorne, M. A. Robb, and L. Blancafort: Photophysics of the π,π^* and n,π^* States of Thymine: MS-CASPT2 Minimum-Energy Paths and CASSCF on-the-Fly Dynamics, *J. Phys. Chem. A* **113**, 10211–10218, 2009.

[184] S. Yamazaki and T. Taketsugu: Nonradiative Deactivation Mechanisms of Uracil, Thymine, and 5-Fluorouracil: A Comparative ab Initio Study, *J. Phys. Chem. A* **116**, 491–503, 2011.

[185] W. Weber and W. Thiel: Orthogonalization corrections for semiempirical methods, *Theor. Chem. Acc.* **103**, 495–506, 2000.

[186] B. G. Levine, C. Ko, J. Quenneville, and T. J. Martínez: Conical intersections and double excitations in time-dependent density functional theory, *Mol. Phys.* **104**, 1039–1051, 2006.

[187] F. Plasser, R. Crespo-Otero, M. Pederzoli, J. Pittner, H. Lischka, and M. Barbatti: Surface Hopping Dynamics with Correlated Single-Reference Methods: 9H-Adenine as a Case Study, *J. Chem. Theory Comput.* **10**, 1395–1405, 2014.

[188] S. Gozem, F. Melaccio, A. Valentini, M. Filatov, M. Huix-Rotllant, N. Ferré, L. M. Frutos, C. Angeli, A. I. Krylov, A. A. Granovsky, R. Lindh, and M. Olivucci: Shape of Multireference, Equation-of-Motion Coupled-Cluster, and Density Functional Theory Potential Energy Surfaces at a Conical Intersection, *J. Chem. Theory Comput.* **10**, 3074–3084, 2014.

[189] J. Tao, J. P. Perdew, V. N. Staroverov, and G. E. Scuseria: Climbing the Density Functional Ladder: Nonempirical Meta–Generalized Gradient Approximation Designed for Molecules and Solids, *Phys. Rev. Lett.* **91**, 146401, 2003.

[190] S. Grimme, J. Antony, S. Ehrlich, and H. Krieg: A consistent and accurate ab initio parametrization of density functional dispersion correction (DFT-D) for the 94 elements H-Pu, *J. Chem. Phys.* **132**, 154104, 2010.

[191] S. Grimme, S. Ehrlich, and L. Goerigk: Effect of the damping function in dispersion corrected density functional theory, *J. Comput. Chem.* **32**, 1456–1465, 2011.

[192] F. Weigend and R. Ahlrichs: Balanced basis sets of split valence, triple zeta valence and quadruple zeta valence quality for H to Rn: Design and assessment of accuracy., *Phys. Chem. Chem. Phys.* **7**, 3297–3305, 2005.

[193] D. Rappoport and F. Furche: Property-optimized Gaussian basis sets for molecular response calculations, *J. Chem. Phys.* **133**, 134105, 2010.

[194] B. Efron: Bootstrap Methods: Another Look at the Jackknife, *Ann. Stat.* **7**, 1–26, 1979.

[195] S. Nangia, A. W. Jasper, T. F. Miller, and D. G. Truhlar: Army ants algorithm for rare event sampling of delocalized nonadiabatic transitions by trajectory surface hopping and the estimation of sampling errors by the bootstrap method, *J. Chem. Phys.* **120**, 3586–3597, 2004.

[196] R. Abouaf, J. Pommier, and H. Dunet: Electronic and vibrational excitation in gas phase thymine and 5-bromouracil by electron impact, *Chem. Phys. Lett.* **381**, 486–494, 2003.

[197] M. Michaud, M. Bazin, and L. o. Sanche: Measurement of inelastic cross sections for low-energy electron scattering from DNA bases, *Int. J. Radiat. Biol.* **88**, 15–21, 2011.

[198] I. V. Chernyshova, E. J. Kontros, P. P. Markush, and O. B. Shpenik: Excitation of lowest electronic states of thymine by slow electrons, *Opt. Spectrosc.* **115**, 645–650, 2013.

[199] D. Cremer and J. A. Pople: General definition of ring puckering coordinates, *J. Am. Chem. Soc.* **97**, 1354–1358, 1975.

[200] J. E. Subotnik, A. Jain, B. Landry, A. Petit, W. Ouyang, and N. Bellonzi: Understanding the Surface Hopping View of Electronic Transitions and Decoherence, *Annu. Rev. Phys. Chem.* **67**, 387–417, 2016.

[201] B. R. Landry, M. J. Falk, and J. E. Subotnik: Communication: The correct interpretation of surface hopping trajectories: How to calculate electronic properties, *J. Chem. Phys.* **139**, 211101, 2013.

[202] L. Wang, D. Trivedi, and O. V. Prezhdo: Global Flux Surface Hopping Approach for Mixed Quantum-Classical Dynamics, *J. Chem. Theory Comput.* **10**, 3598–3605, 2014.

[203] S. M. Parker and F. Furche: Response Theory and Molecular Properties, in M. J. Wójcik, H. Nakatsuji, B. Kirtman, and Y. Ozaki, editors, Frontiers of Quantum Chemistry, pp. 69–86, Springer Singapore, Singapore, 2018.

[204] TURBOMOLE website, `https://www.turbomole.org` (retrieved January 10, 2020).

[205] S. M. Parker, S. Roy, and F. Furche: Multistate hybrid time-dependent density functional theory with surface hopping accurately captures ultrafast thymine photodeactivation, UC Irvine Dash, Dataset, 2019.

[206] G. Pereira Rodrigues, E. Ventura, S. A. do Monte, and M. Barbatti: Photochemical Deactivation Process of HCFC-133a ($C_2H_2F_3Cl$): A Nonadiabatic Dynamics Study, *J. Phys. Chem. A* **118**, 12041–12049, 2014.

[207] D. Tuna, N. Došlić, M. Mališ, A. L. Sobolewski, and W. Domcke: Mechanisms of Photostability in Kynurenines: A Joint Electronic-Structure and Dynamics Study, *J. Phys. Chem. B* **119**, 2112–2124, 2015.

[208] D. Fazzi, M. Barbatti, and W. Thiel: Unveiling the Role of Hot Charge-Transfer States in Molecular Aggregates via Nonadiabatic Dynamics, *J. Am. Chem. Soc.* **138**, 4502–4511, 2016.

[209] A. Prlj, N. Došlić, and C. Corminboeuf: How does tetraphenylethylene relax from its excited states?, *Phys. Chem. Chem. Phys.* **18**, 11606–11609, 2016.

[210] B. Marchetti and T. N. V. Karsili: Theoretical insights into the photo-protective mechanisms of natural biological sunscreens: building blocks of eumelanin and pheomelanin, *Phys. Chem. Chem. Phys.* **18**, 3644–3658, 2016.

[211] M. Mališ and N. Došlić: Nonradiative Relaxation Mechanisms of UV Excited Phenylalanine Residues: A Comparative Computational Study, *Molecules* **22**, 493, 2017.

[212] C. Wiebeler, F. Plasser, G. J. Hedley, A. Ruseckas, I. D. W. Samuel, and S. Schumacher: Ultrafast Electronic Energy Transfer in an Orthogonal Molecular Dyad, *J. Phys. Chem. Lett.* **8**, 1086–1092, 2017.

[213] C. Cisneros, T. Thompson, N. Baluyot, A. C. Smith, and E. Tapavicza: The role of tachysterol in vitamin D photosynthesis – a non-adiabatic molecular dynamics study, *Phys. Chem. Chem. Phys.* **19**, 5763–5777, 2017.

[214] M. Ben-Nun, J. Quenneville, and T. J. Martínez: Ab Initio Multiple Spawning: Photo-chemistry from First Principles Quantum Molecular Dynamics, *J. Phys. Chem. A* **104**(22), 5161–5175, 2000.

[215] R. Long, D. Casanova, W.-H. Fang, and O. V. Prezhdo: Donor-Acceptor Interaction Determines the Mechanism of Photoinduced Electron Injection from Graphene Quantum Dots into TiO_2: π-Stacking Supersedes Covalent Bonding, *J. Am. Chem. Soc.* **139**(7), 2619–2629, 2017.

[216] R. Long and O. V. Prezhdo: Ab Initio Nonadiabatic Molecular Dynamics of the Ultrafast Electron Injection from a PbSe Quantum Dot into the TiO_2 Surface, *J. Am. Chem. Soc.* **133**(47), 19240–19249, 2011.

[217] E. Tapavicza, T. Thompson, K. Redd, and D. Kim: Tuning the Photoreactivity of Z-Hexatriene Photoswitches by Substituents - a Non-Adiabatic Molecular Dynamics Study, *Phys. Chem. Chem. Phys.* **20**(38), 24807–24820, 2018.

[218] S. Hammes-Schiffer and J. C. Tully: Proton transfer in solution: Molecular dynamics with quantum transitions, *J. Chem. Phys.* **101**(6), 4657–4667, 1994.

[219] Q. Ou, S. Fatehi, E. Alguire, Y. Shao, and J. E. Subotnik: Derivative Couplings between TDDFT Excited States Obtained by Direct Differentiation in the Tamm-Dancoff Approximation, *J. Chem. Phys.* **141**(2), 024114, 2014.

[220] W. Zhang, M. B. Jungfleisch, W. Jiang, J. Sklenar, F. Y. Fradin, J. E. Pearson, J. B. Ketterson, and A. Hoffmann: Spin pumping and inverse spin Hall effects–Insights for future spin-orbitronics (invited), *J. App. Phys.* **117**(17), 172610, 2015.

[221] S. M. Parker, S. Roy, and F. Furche: Multistate Hybrid Time-Dependent Density Functional Theory with Surface Hopping Accurately Captures Ultrafast Thymine Photodeactivation, *Phys. Chem. Chem. Phys.* **21**, 18999–19010, 2019.

[222] J.-Y. Fang and S. Hammes-Schiffer: Improvement of the Internal Consistency in Trajectory Surface Hopping, *J. Phys. Chem. A* **103**(47), 9399–9407, 1999.

[223] J. E. Subotnik, W. Ouyang, and B. R. Landry: Can We Derive Tully's Surface-Hopping Algorithm from the Semiclassical Quantum Liouville Equation? Almost, but only with Decoherence, *J. Chem. Phys.* **139**(21), 214107, 2013.

[224] R. I. Bakalska and V. B. Delchev: Comparative Study of the Relaxation Mechanisms of the Excited States of Cytosine and Isocytosine, *J. Mol. Model.* **18**(12), 5133–5146, 2012.

[225] R. Szabla, R. W. Góra, and J. Šponer: Ultrafast Excited-State Dynamics of Isocytosine, *Phys. Chem. Chem. Phys.* **18**(30), 20208–20218, 2016.

[226] D. Hu, Y. F. Liu, A. L. Sobolewski, and Z. Lan: Nonadiabatic Dynamics Simulation of Keto Isocytosine: A Comparison of Dynamical Performance of Different Electronic-Structure Methods, *Phys. Chem. Chem. Phys.* **19**(29), 19168–19177, 2017.

[227] M. Barbatti, A. J. A. Aquino, and H. Lischka: Ultrafast Two-Step Process in the Non-Adiabatic Relaxation of the $CH_2NH_2^+$ molecule, *Mol. Phys.* **104**(5-7), 1053–1060, 2006.

[228] L. Martínez-Fernández, I. Corral, G. Granucci, and M. Persico: Competing Ultrafast Inter-system Crossing and Internal Conversion: A Time Resolved Picture for the Deactivation of 6-Thioguanine, *Chem. Sci.* **5**(4), 1336, 2014.

[229] S. Roy, S. Ardo, and F. Furche: 5-Methoxyquinoline Photobasicity Is Mediated by Water Oxidation, *J. Phys. Chem. A* **123**, 6645–6651, 2019.

[230] A. W. Jasper and D. G. Truhlar: Improved treatment of momentum at classically forbidden electronic transitions in trajectory surface hopping calculations, *Chem. Phys. Lett.* **369**(1-2), 60–67, 2003.

[231] A. W. Jasper, S. Nangia, C. Zhu, and D. G. Truhlar: Non-Born-Oppenheimer Molecular Dynamics, *Acc. Chem.* **39**(2), 101–108, 2006.

[232] F. Plasser, S. Mai, M. Fumanal, E. Gindensperger, C. Daniel, and L. González: Strong Influence of Decoherence Corrections and Momentum Rescaling in Surface Hopping Dynamics of Transition Metal Complexes, *J. Chem. Theory Comput.* **15**(9), 5031–5045, 2019.

[233] H. Lischka, M. Barbatti, F. Siddique, A. Das, and A. J. Aquino: The Effect of Hydrogen Bonding on the Nonadiabatic Dynamics of a Thymine-Water Cluster, *Chem. Phys.* **515**, 472–479, 2018.

[234] S. Chen, N. Ullah, Y. Zhao, and R. Zhang: Nonradiative Excited-State Decay via Conical Intersection in Graphene Nanostructures, *ChemPhysChem* **20**(21), 2754–2758, 2019.

[235] B. Smith and A. V. Akimov: Modeling Nonadiabatic Dynamics in Condensed Matter Materials: Some Recent Advances and Applications, *J. Condens. Matter Phys.* **32**(7), 073001, 2019.

[236] A. W. Jasper and D. G. Truhlar: Non-Born-Oppenheimer Molecular Dynamics of Na... Photodissociation, *J. Chem. Phys.* **127**(19), 194306, 2007.

[237] B. R. Landry and J. E. Subotnik: How to Recover Marcus Theory with Fewest Switches Surface Hopping: Add just a Touch of Decoherence, *J. Chem. Phys.* **137**(22), 22A513, 2012.

[238] S. D. Elliott, R. Ahlrichs, O. Hampe, and M. M. Kappes: Auto-Ionised Products from the Reaction of Sodium Clusters with Dioxygen: Theory and Experiment, *Phys. Chem. Chem. Phys.* **2**(15), 3415–3424, 2000.

[239] C. Hättig and F. Weigend: CC2 excitation energy calculations on large molecules using the resolution of the identity approximation, *J. Chem. Phys.* **113**(13), 5154, 2000.

[240] V. N. Staroverov, G. E. Scuseria, J. Tao, and J. P. Perdew: Comparative assessment of a new nonempirical density functional: Molecules and hydrogen-bonded complexes, *J. Chem. Phys.* **119**(23), 12129–12137, 2003.

[241] J. P. Perdew, K. Burke, and M. Ernzerhof: Generalized Gradient Approximation Made Simple, *Phys. Rev. Lett.* **77**(18), 3865–3868, 1996.

[242] H. R. Hudock, B. G. Levine, A. L. Thompson, H. Satzger, D. Townsend, N. Gador, S. Ullrich, A. Stolow, and T. J. Martínez: Ab Initio Molecular Dynamics and Time-Resolved Photoelectron Spectroscopy of Electronically Excited Uracil and Thymine, *J. Phys. Chem. A* **111**(34), 8500–8508, 2007.

[243] M. Barbatti, J. J. Szymczak, A. J. A. Aquino, D. Nachtigallová, and H. Lischka: The Decay Mechanism of Photoexcited Guanine - A Nonadiabatic Dynamics Study, *J. Chem. Phys.* **134**(1), 014304, 2011.

[244] J. v. Neumann: Wahrscheinlichkeitstheoretischer Aufbau der Quantenmechanik, *Nachrichten von der Gesellschaft der Wissenschaften zu Göttingen, Mathematisch-Physikalische Klasse* **1927**, 245–272, 1927.

[245] L. Verlet: Computer "Experiments" on Classical Fluids. I. Thermodynamical Properties of Lennard-Jones Molecules, *Phys. Rev.* **159**(1), 98–103, 1967.

Appendix A

A practical guide to implementation of FSSH

Of the many ways of approximately solving for the nuclear motion in cases where there are energetically close electronic states, the fewest switches surface hopping (FSSH) is perhaps the most popular method.[22] In this method, the splitting of the nuclear population on different electronic potential energy surfaces is modeled by treating an ensemble of classical trajectories, where each trajectory derives its driving force from the gradient of one of the electronic states, often referred to as the active state. Each trajectory carries with it a corresponding electronic reduced density matrix, which is also propagated in time. The trajectories can 'hop', that is, change the electronic state to propagate the nuclei. The probability of hopping is devised such that the distribution of active states in the ensemble matches the electronic populations.

The classical dynamical variables are position ($\mathbf{R}$) and velocity ($\mathbf{v}$). The classical Hamiltonian is

$$H_{classical} = \frac{1}{2}\mathbf{P}^T\mathbf{M}^{-1}\mathbf{P} + V_{active}(\mathbf{R}). \tag{A.1}$$

The mass matrix is the diagonal matrix $\mathbf{M}$ where the mass associated with each degree of freedom

is on the diagonal. In our case, the degrees of freedom are atomic coordinates, hence the masses are atomic masses The momentum is defined as $\mathbf{P} = \mathbf{M}\dot{\mathbf{R}}$.

In our implementation, velocity of the nuclei is the dynamical variable, denoted as $\mathbf{v}$,

The dynamical variable for the quantum dynamics is σ which is defined as:

$$\hat{\sigma}_{aux} = \sum_{NM} \sigma_{NM} |\Psi_{el}^N(\mathbf{x}; \mathbf{R})\rangle \langle \Psi_{el}^M(\mathbf{x}; \mathbf{R})|. \tag{A.2}$$

The quantum Hamiltonian necessary for the propagation of the electronic density matrix is:

$$\bar{\mathbf{H}}(\mathbf{R}) = \mathbf{V}(\mathbf{R}) + i\mathbf{P}^T\mathbf{M}^{-1}\mathbf{d}(\mathbf{R}) \tag{A.3}$$

where the adiabatic potential energy is defined as:

$$\mathbf{V}_{NM}(\mathbf{q}) = E_N(\mathbf{q})\delta_{MN} \tag{A.4}$$

and $\mathbf{d}$ is the derivative coupling.

The equation of motion for the electronic density matrix[244] is

$$\dot{\sigma} = i[\bar{\mathbf{H}}, \sigma]. \tag{A.5}$$

The propagation is carried out in discrete time steps Δt. The algorithm used is leap frog velocity Verlet[245] for the propagation of the nuclear position and velocity. In leap frog velocity Verlet, the

velocities are half-time step staggered from the position. In our implementation, the positions are kept at integer time steps, and velocities at half-time steps apart. As a consequence, all position-dependent quantities such as energies, gradients and derivative couplings are available only at integer time-steps.

The numerical procedure to update the position and velocity in each simulation step is given by:

$$\mathbf{F}(t_n) = -\frac{\partial V_{active}(\mathbf{R})}{\mathbf{R}}\bigg|_{\mathbf{R}=\mathbf{R}(t_n)} \tag{A.6}$$

$$\mathbf{v}(t + \frac{1}{2}\Delta t) = \mathbf{v}(t - \frac{1}{2}\Delta t) + \mathbf{M}^{-1}\mathbf{F}(t_n)\Delta t \tag{A.7}$$

$$\mathbf{q}(t + \Delta t) = \mathbf{q}(t) + \mathbf{v}(t + \frac{1}{2}\Delta t)\Delta t. \tag{A.8}$$

The position and velocities are interlaced in time. The electronic density matrix is implemented to be synchronous with the positions in each simulation time. The electronic density matrix is propagated with an exponential operator:

$$\sigma(t + \Delta t) = e^{-i\bar{\mathbf{H}}\mathbf{\Delta t}}\sigma(t)e^{i\bar{\mathbf{H}}\Delta t} \tag{A.9}$$

$\bar{\mathbf{H}}$ is constructed using the midpoint approximation for the velocities.

$$\bar{\mathbf{H}}_{MN}(t_n) = V_M(t_n)\delta_M + i\frac{1}{2}(\mathbf{v}(t_n - \frac{1}{2}\Delta t) + \mathbf{v}(t_n + \frac{1}{2}\Delta t))\mathbf{d}_{MN}(t_n) \tag{A.10}$$

For the construction of the exponential propagator for the electronic density matrix $\bar{\mathbf{H}}$ is diagonalized,

$$\bar{\mathbf{H}} = \kappa^\dagger \mathbf{W} \kappa. \tag{A.11}$$

Where $\mathbf{W}$ is diagonal, and κ is the transformation matrix.

The exponential propagator is constructed as:

$$e^{-i\bar{\mathbf{H}}\mathbf{\Delta t}} = \kappa^\dagger e^{-i\mathbf{W}\Delta t} \kappa \tag{A.12}$$

At each time step, the probability of hopping from the active state to every other state is calculated. The probability of hopping from state K to state N $(g_{K \to N})$ is defined as:

$$g_{K \to N} = \Delta t \times \quad \left(\sigma_{NK}(t + \Delta t/2)\bar{H}_{KN} - \bar{H}_{NK}\sigma KN(t + \Delta t/2) \right) / \sigma_{kk}(t + \Delta t/2) \tag{A.13}$$

In case of a hop, the rescaling of the velocities is considered at the integer time step. Thus, there is a discontinuous potential,

$$V(\mathbf{R}) = \begin{cases} V_{old}(\mathbf{R}), & \text{if } t < t_n \\ V_{old}(\mathbf{R}_n) + V_{new}(\mathbf{R}) + \Theta(t - t_n)(V_{new}(\mathbf{R}_n) - V_{old}(\mathbf{R}_n)) & t \geq t_n \end{cases} \tag{A.14}$$

Where $\mathbf{R}_n$ is the nuclear coordinate at $t = t_n$

Hence the force used to integrate the nuclear dynamical variables

$$\mathbf{F}(t) = \begin{cases} \mathbf{F}_{old}(t), & \text{if } t < t_n \\ \mathbf{F}_{new}(t) + \delta(t - t_n)(\Delta E)\tau & t \geq t_n \end{cases} \tag{A.15}$$

The numerical integration for the velocity becomes

$$\mathbf{v}(t + \frac{1}{2}\Delta t) = \mathbf{v}(t - \frac{1}{2}\Delta t) + \mathbf{M}^{-1}\mathbf{F}_{old}(t_n)\frac{\Delta t}{2} + \mathbf{M}^{-1}\mathbf{F}_{new}(t_n)\frac{\Delta t}{2} + \Delta E\tau \tag{A.16}$$

where τ is an unknown vector along which the momentum is to be scaled by a factor λ. Tully recommends using the nonadiabatic coupling vector $\mathbf{d}$ between the active state and the state to hop to.

The momenta are rescaled in the direction of τ by solving

$$\tilde{\mathbf{P}} = \mathbf{P} + \lambda\tau. \tag{A.17}$$

Conservation of energy leads to the following equation for λ

$$\lambda^2\left(\frac{\tau^T\mathbf{M}^{-1}\tau}{2}\right) + \lambda(\mathbf{v}^T\tau) + \Delta E = 0. \tag{A.18}$$

There are two solutions to the equation, and the λ with the smaller magnitude is chosen.

Hence, in case of a hop, the overall update for the velocity becomes

$$\mathbf{v}(t_n) = \mathbf{v}(t_n - \frac{1}{2}\Delta t) + \mathbf{M}^{-1}\mathbf{F}_{old}\frac{\Delta t}{2}, \tag{A.19}$$

$$\tilde{\mathbf{v}}(t_n) = \mathbf{v}(t_n) + \lambda \mathbf{M}^{-1}\tau, \tag{A.20}$$

where $\tilde{\mathbf{v}}$ is the intermediate velocity at an integer time-step after rescaling, and

$$\mathbf{v}(t_n + \frac{1}{2}\Delta t) = \tilde{\mathbf{v}}(t_n) + \mathbf{M}^{-1}\mathbf{F}_{new}\frac{\Delta t}{2}. \tag{A.21}$$